This is to certify that the

dissertation entitled

Raman Spectroscopy of modified porphyrin
Macrocycle - porphycene and ~~P~~ chlorin -

presented by

Kim, Younkyoo

has been accepted towards fulfillment
of the requirements for

Ph. D degree in Chemistry department

Major professor

Date 2/26/1992

RAMAN SPECTROSCOPY OF MODIFIED PORPHYRIN MACROCYCLES
- PORPHYCENE AND CHLORIN -

BY

YOUNKYOO KIM

A DISSERTATION

Submitted to
Michigan State University
in partial fulfillment of the requirements
for the degree of

DOCTOR OF PHILOSOPHY

Department of Chemistry

1992

Abstract

RAMAN SPECTROSCOPY OF MODIFIED PORPHYRIN MACROCYCLES - PORPHYCENE AND CHLORIN -

BY

YOUNKYOO KIM

The electronic and vibronic properties of metalloporphycenes (MPPC) which are isomers of the extensively studied metalloporphyrins, and the effect of lower symmetry in metallooctaethylchlorins (MOEC) were studied by using UV-visible, IR, Raman spectroscopy and normal coordinate calculations.

Close investigation of absorption band positions, spectral shifts caused by metal substitution, ring bromination and oscillator strengths reveal that the $\pi \rightarrow \pi^*$ states of MPPC are adequately defined by one-electron wave functions unlike those of metalloporphyrins. Thus the π-electron configuration interaction, which dominates the spectroscopy of the metalloporphyrins, is weak in the MPPC. Raman spectra of CuPPC with either Soret or visible excitation do not show anomalously polarized bands, which are commonly observed in metalloporphyrins. This means that Herzberg - Teller mechanisms for vibronic coupling are

extremely weak in the MPPC. Several vibrational bands show dependence on the central metal in the MPPC that is analogous to the metal dependent frequencies of the structure sensitive bands in the metalloporphyrins. Like hemes, both UV-visible and resonance Raman spectra of FePPC derivatives demonstrate sensitivity to iron spin and oxidation states. This suggests an overlap of the iron d_{xz}, d_{yz} and the porphycene π orbitals.

Normal coordinate calculations based on the IR and resonance Raman spectra of selectively meso-deuterated CuOEC (CuOEC-h_4, CuOEC-$\alpha\beta$-d_2, CuOEC-$\gamma\delta$-d_2, CuOEC-d_4) are reported. In general, the calculations show that various force fields satisfactorily reproduce the experimental data of CuOEC. However, none of these force fields reproduce the frequencies and meso-deuteration shift patterns of all of the modes. This suggests that 1,4 and higher interaction constants could be important to the valence force field. All of the force fields indicate that the eigenvectors of certain skeletal mode are localized on sectors of the macrocycle. A detailed vibrational spectroscopic characterization of ZnOEC was also completed. The meso-deuteration shift patterns of CuOEC and ZnOEC show that mode localization phenomena are not dependent on the identity of the central metal but are inherent properties of metallochlorins that results from their reduced symmetry.

To my mother and in memory of my father

ACKNOWLEDGMENTS

I am deeply grateful to Dr. Gerald T. Babcock for his guidance and financial support. I wish to also thank Dr. George E. Leroi for serving as second leader. Tony, Juan and Dr. T. Carter deserve a special thanks for their technical assistance with Raman spectroscopy. Special thanks is extended to W. Wu and Einhard for their sincerity, enthusiasm and perseverance in the preparation of porphycenes and chlorins. Thanks also go to Mike, Hak-Hyun and Alex for their discussions and help with the set of the normal coordinate analysis programs. I also express my thankfulness to all our group member for their friendship. I also appreciate the encouragement and assistance of Mr. Dae W. Yun, all of my friends and all Korean students in the chemistry department. Without their assistance, this work would have been much more difficult.

Finally, I would like to thank to my wife (Yunmi), my daughter (Yeaji), and my family, including my parents-in-law, for their patience, love, help, and constant encouragement.

TABLE OF CONTENTS

Page

List of Tables

List of Figures

Page

CHAPTER 1

GENERNAL INTRODUCTION

1.1) The structure of the macrocycles studied

1.1.1) Metalloporphyrin

The metalloporphyrins, referred to as the pigments of life owing to their biological significance, are characterized by a tetrapyrrole macrocycle with an extensively delocalized π electron system.[1] Metalloporphyrins play important roles in such diverse biochemical functions as oxygen transport, storage and utilization (hemoglobin, myoglobin, cytochrome oxidase), electron transfer (the cytochromes) and catalysis (cytochrome P450, horseradish peroxidase, catalase).[2] Figure 1-1 shows the basic structure of a typical synthetic metallooctaethylporphyrin. The four pyrrole rings are joined at the methine bridge or meso positions, which are labelled $\alpha, \beta, \gamma, \delta$ in Figure 1-1, and various peripheral substituents can be linked to the b-carbon positions, which are usually labelled 1-8. The remaining carbon atoms adjacent to the pyrrole nitrogens are called a-carbons.

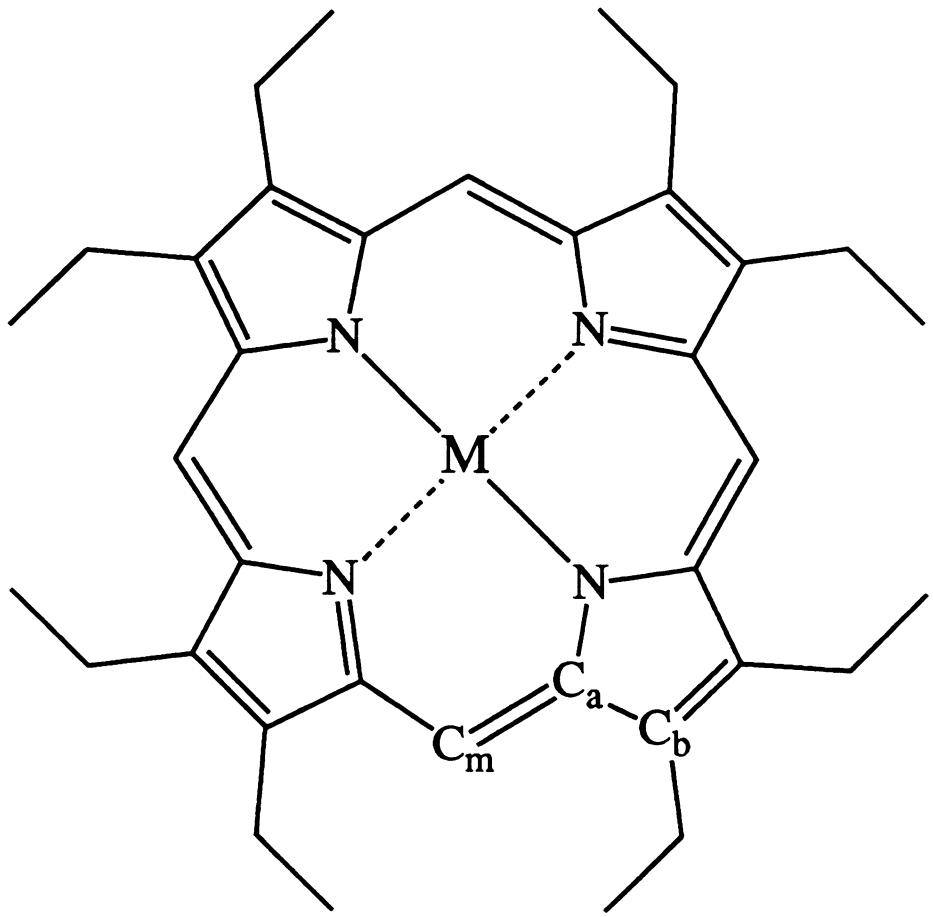

Figure 1-1 Structure of Metallooctaethylporphyrin

1.1.2) Metalloporphycene

Metalloporphycene, a tetrapyrrole macrocycle recently synthesized by Vogel et al.[3], represents a class of molecules that are structural isomers of metalloporphyrins. The limited solubility of porphycene and metalloporphycene led Vogel and co-workers[4-8] to develop the synthesis of 2, 7, 12, 17-tetrapropylporphycene (Figure 1-2). This compound is expected to assume a role in porphycene investigations similar to that of octaethylporphyrin (OEP) in studies of model porphyrin complexes.

1.1.3) Metallochlorin

Metallochlorin is a metalloporphyrin derivative in which a C_bC_b bond of one of the pyrrole rings has been reduced.[9] The structure of metallooctaethylchlorin is shown in Figure 1-3. The reduced C_bC_b bond can have the cis or trans configurations. Metallochlorins are ubiquitous in nature, occurring as the chlorophyll pigments in photosynthetic systems[10], in marine worm pigments[11], and in the green heme proteins, leucocyte myeloperoxidase[12], sulfmyoglobin[13], sulfhemoglobin[14] and bacterial heme-d containing enzymes.[15-16] Reduction of a C_bC_b bond in a metalloporphyrin to form a metallochlorin lowers the molecular symmetry from D_{4h} to C_2 and has a profound effect on the entire macrocycle. A comparative study of FeOEP and FeOEC by X-ray crystallography[17] revealed that the average iron-nitrogen distance is very similar in the two

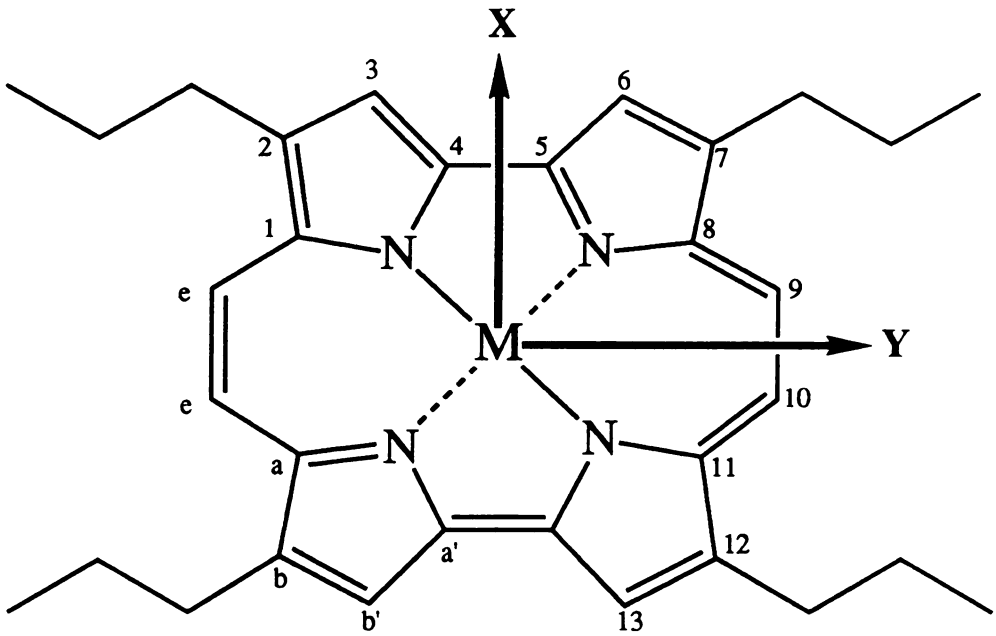

Figure 1-2 Structure of Metallo-2,7,12,17-tetra-propylporphycene

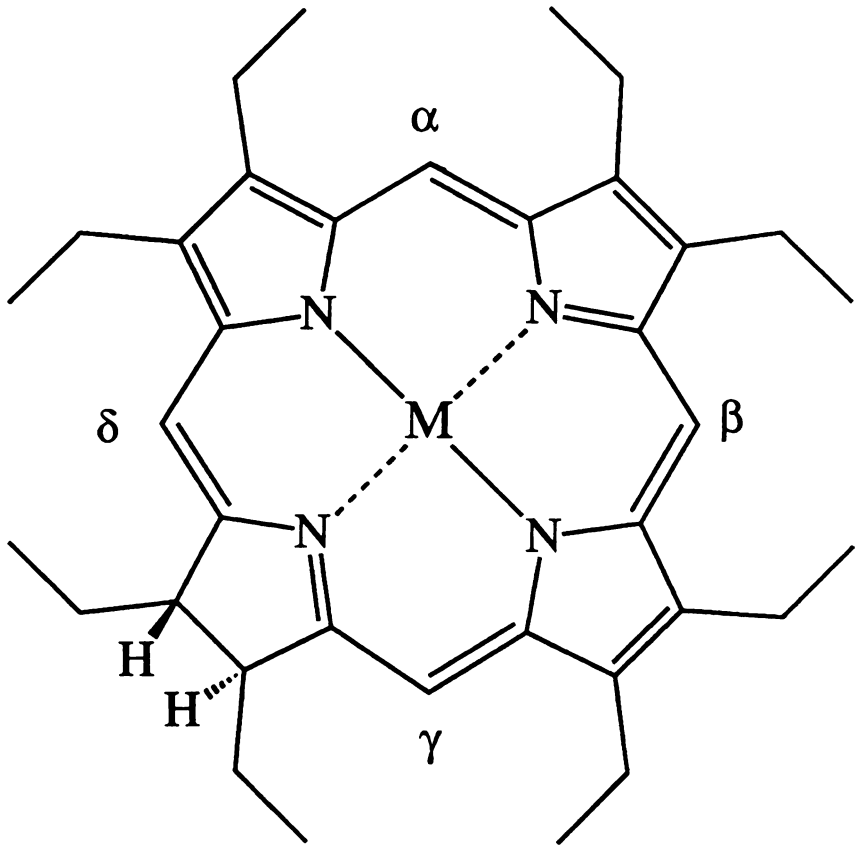

Figure 1-3 Structure of Metallooctaethylchlorin

complexes(1.996Å for FeOEP and 1.986Å for FeOEC). However, the macrocycle of iron octaethylporphyrin is planar but that of iron octaethylchlorin is S_4 ruffled (Figure 1-4). This distortion, which is due to the decreased aromaticity of the chlorin, is produced by the increased flexibility of the macrocycle.

1.2) Electronic absorption spectroscopy

A great deal of structural information can be obtained from the absorption spectra of modified porphyrin macrocycles. The object of several spectroscopic theories has been to explain the optical spectra of porphyrin and modified porphyrin macrocycles. Figure 1-5 shows the electronic absorption spectrum of a typical metalloporphyrin of D_{4h} symmetry, copper octaethylporphyrin, in CH_2Cl_2 solution. Two visible bands are seen between 500 and 600 nm, and the two are separated by ~1250 cm^{-1}. The lower-energy band (called α) is the electronic origin Q(0,0) of the lowest-energy excited singlet state.[18] The higher energy band (called β) associated with the Q(0,0) transition includes one mode of vibrational excitation and is denoted Q(0,1).[18] An exceedingly intense band (called the Soret) appears around 400 nm. It is the origin B(0,0) of the second excited singlet state.[18] Better resolved Soret spectra sometimes show another band ~1250 cm^{-1} to the blue, which is attributed to the optical transition that includes one quantum of vibrational excitation in addition to the B(0,0)

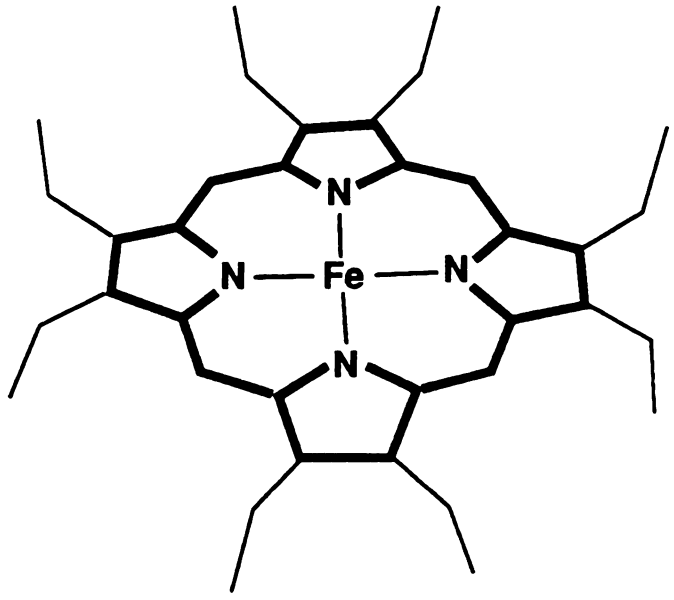

(a)

$Fe^{II}OEP$

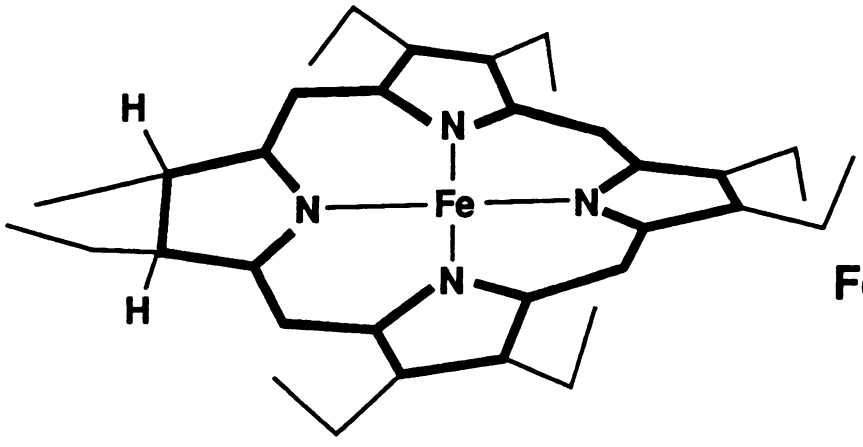

(b)

$Fe^{II}OEC$

Figure 1-4 Molecular structure of a) $Fe^{II}OEP$ b) $Fe^{II}OEC$ as determined by X-ray crystallography (from ref.17)

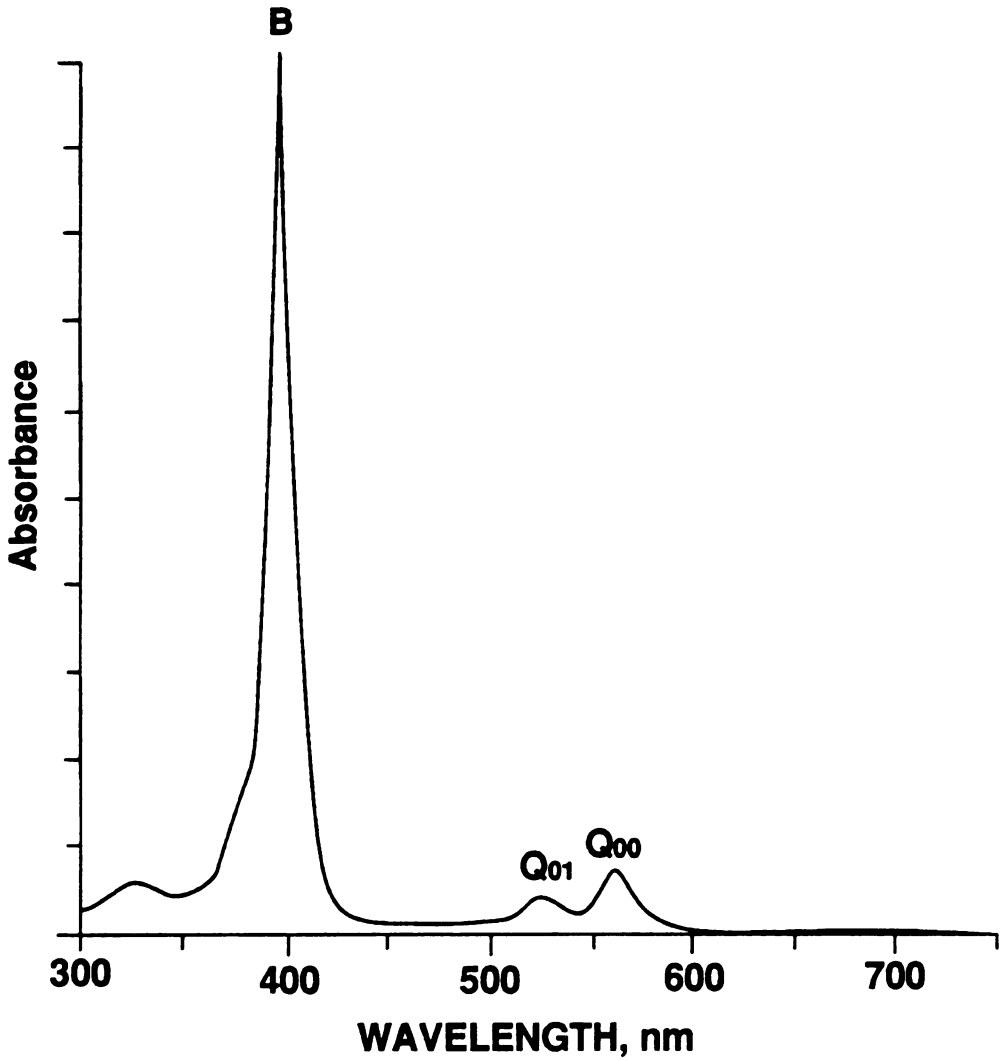

Figure 1-5 Electronic absorption spectrum of CuOEP in CH_2Cl_2 solution

energy and is denoted B(1,0).[18] In D_{4h} symmetry these Q and B electronic transitions are of E_u symmetry and therefore degenerate and x,y polarized in the plane of the ring. In order to understand the porphyrin electronic transitions, Longuet-Higgins et al.[19] employed molecular orbital calculations. Under D_{4h} symmetry, they obtained two top-filled orbitals, a_{2u} and a_{1u} (with a_{1u} of lower energy) and two lowest empty degenerate orbitals of e_g symmetry (Figure 1-6). This identifies two electronic transitions, ($a_{1u} \rightarrow e_g$) and ($a_{2u} \rightarrow e_g$), corresponding to the Q and B bands, respectively. However, this development could not predict the correct intensities for the two transitions. The weakness of this method comes from the neglect of interaction between the two electronic transitions. Based on molecular orbital calculations, Gouterman[20-21] recognized the necessity of configuration interaction in order to describe the porphyrin electronic transitions. The singly excited configurations ($a_{2u}^1 e_g^1$) and ($a_{1u}^1 e_g^1$) have the same symmetry and undergo configuration interaction to produce the excited states that correspond to the B and Q transitions. The transition dipoles for the B state are additive and allowed; hence, the strong Soret absorption. On the other hand, the transition dipoles in the Q state are forbidden, which accounts for the weak visible absorption. The energy and intensity of the B and Q transition in the porphyrins are also affected by other electronic factors such as: the central metal ion, metal oxidation state, spin state and

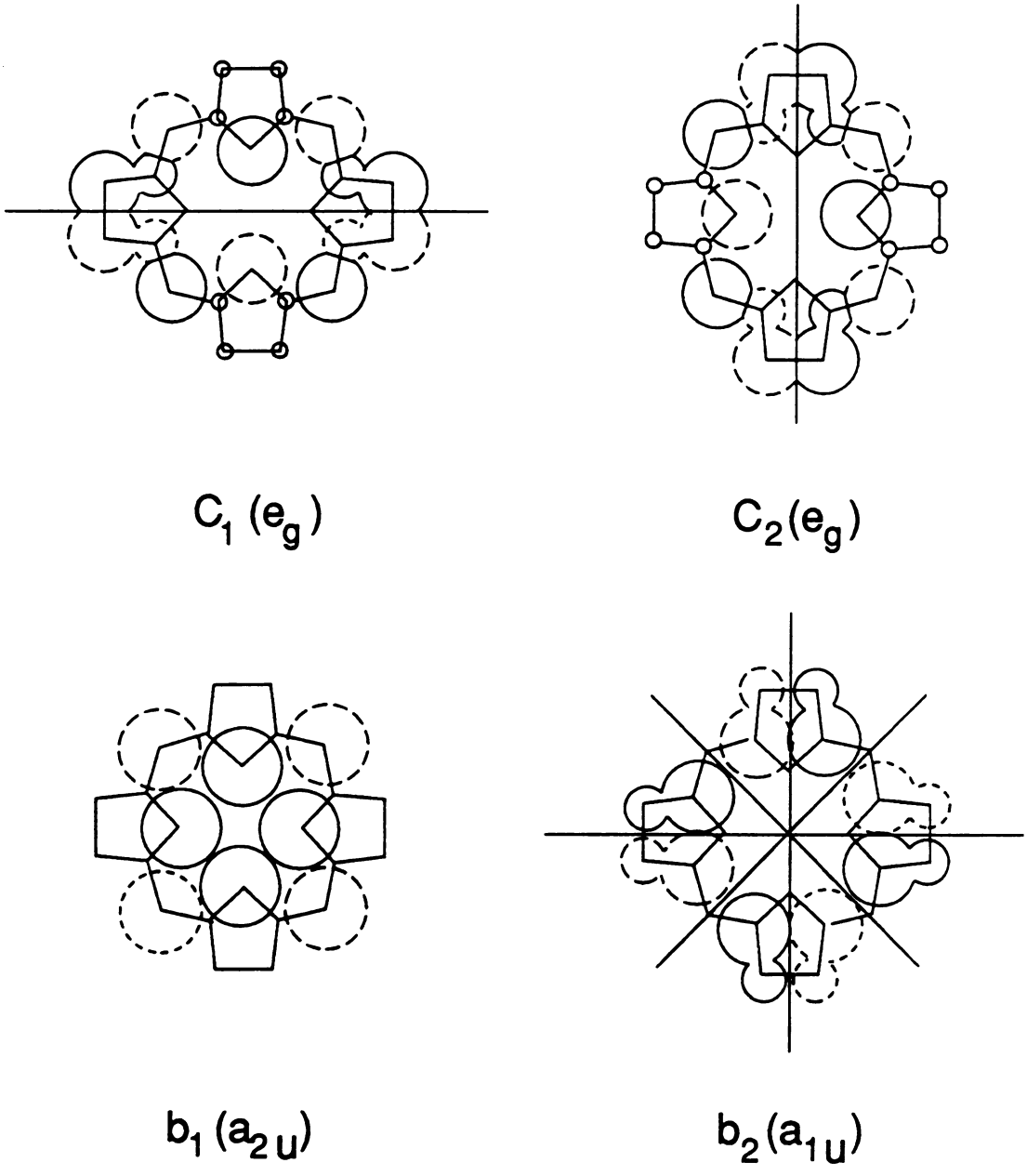

Figure 1-6 Porphyrin M.O.s comprising the Gouterman four oribtal model (from ref.20)

axial-coordination. The metal $d\pi$ orbitals can conjugate with the π electron system of the porphyrin macrocycle (Figure 1-7).

1.3) Infrared and Raman Spectroscopy[22a]

Molecular vibrational spectroscopy deals with interactions of electromagnetic radiation with matter that produce a variation in the vibrational motions of the molecules. The study of these vibrations is important for the understanding of several physical properties of molecular compounds that depend upon the vibrational states of the molecules, and represents a powerful tool for molecular-level investigations. The interaction of electromagnetic radiation with an assembly of molecules can be analyzed by measuring either the absorption of infrared radiation or the scattering of light. Although the two phenomena are controlled by completely different interaction mechanisms, they are determined by the same types of transitions between vibrational states. In principle the infrared spectrum of molecules can be observed either in absorption or in emission, because molecules can emit the same radiation that they can absorb. In practice, however, the absorption spectrum is much more convenient for laboratory measurements. Figure 1-8(a) shows the molecular processes involved in infrared spectroscopy. Here, $|m\rangle$ and $|n\rangle$ represent different quantum states of a vibrational mode in the ground electronic state of the molecule.

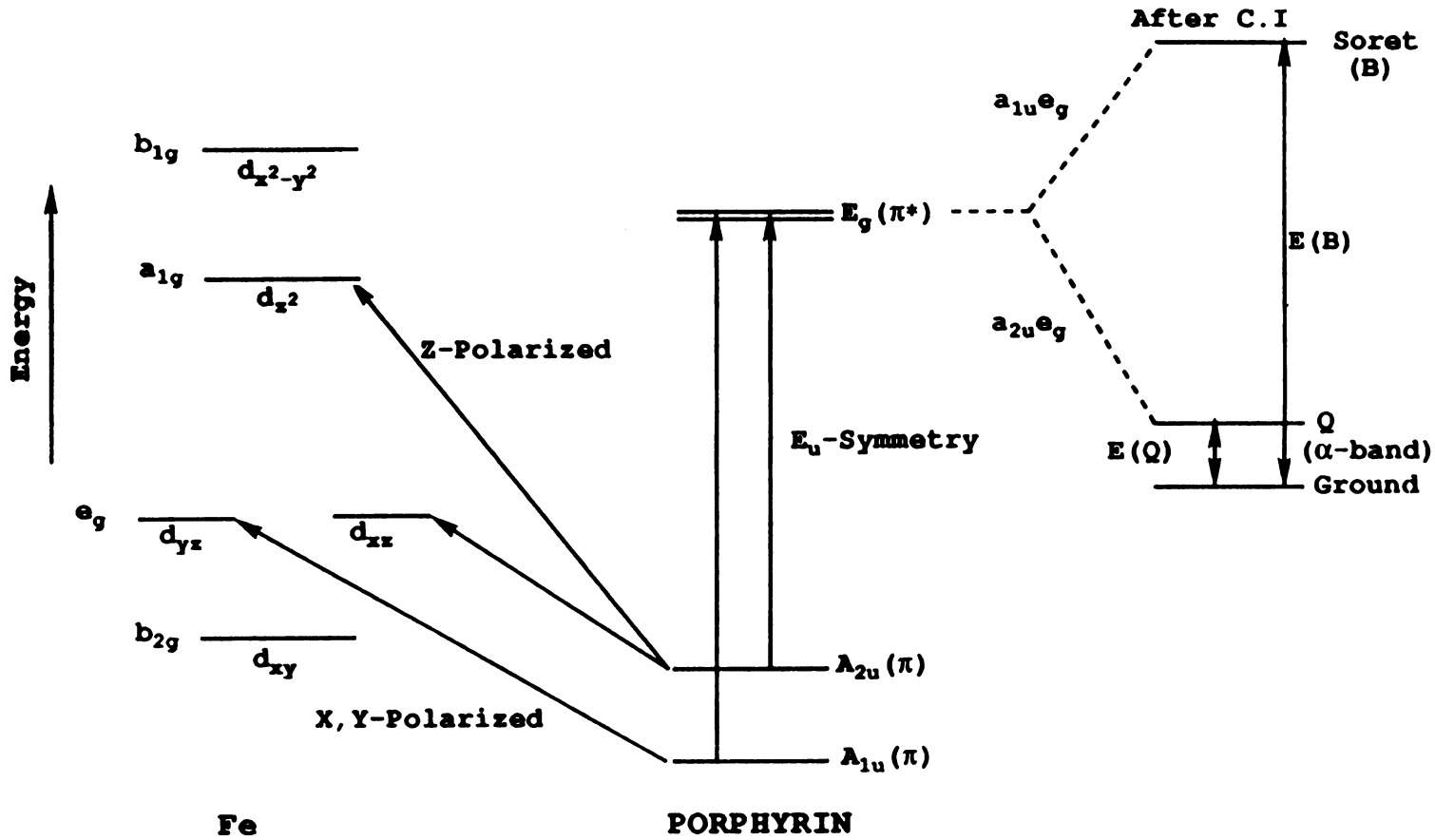

Figure 1-7 Energy diagram for metalloporphyrin absorption spectra. The porphyrin orbitals are indicated at the center of the figure.The mixed-excited states ($a_{1u}{}^1e_g{}^1$) and ($a_{2u}{}^1e_g{}^1$) interact via configuration interaction (C.I.) to give the α-band and Soret, respectively. This is shown on the right hand side of the figure. Interaction of porphyrin orbitals (a_{1u}, a_{2u}) with the metal orbitals of the appropriate symmetry (d_{xz} and d_{yz}) is shown on the left hand side of the figure (from ref. 22b).

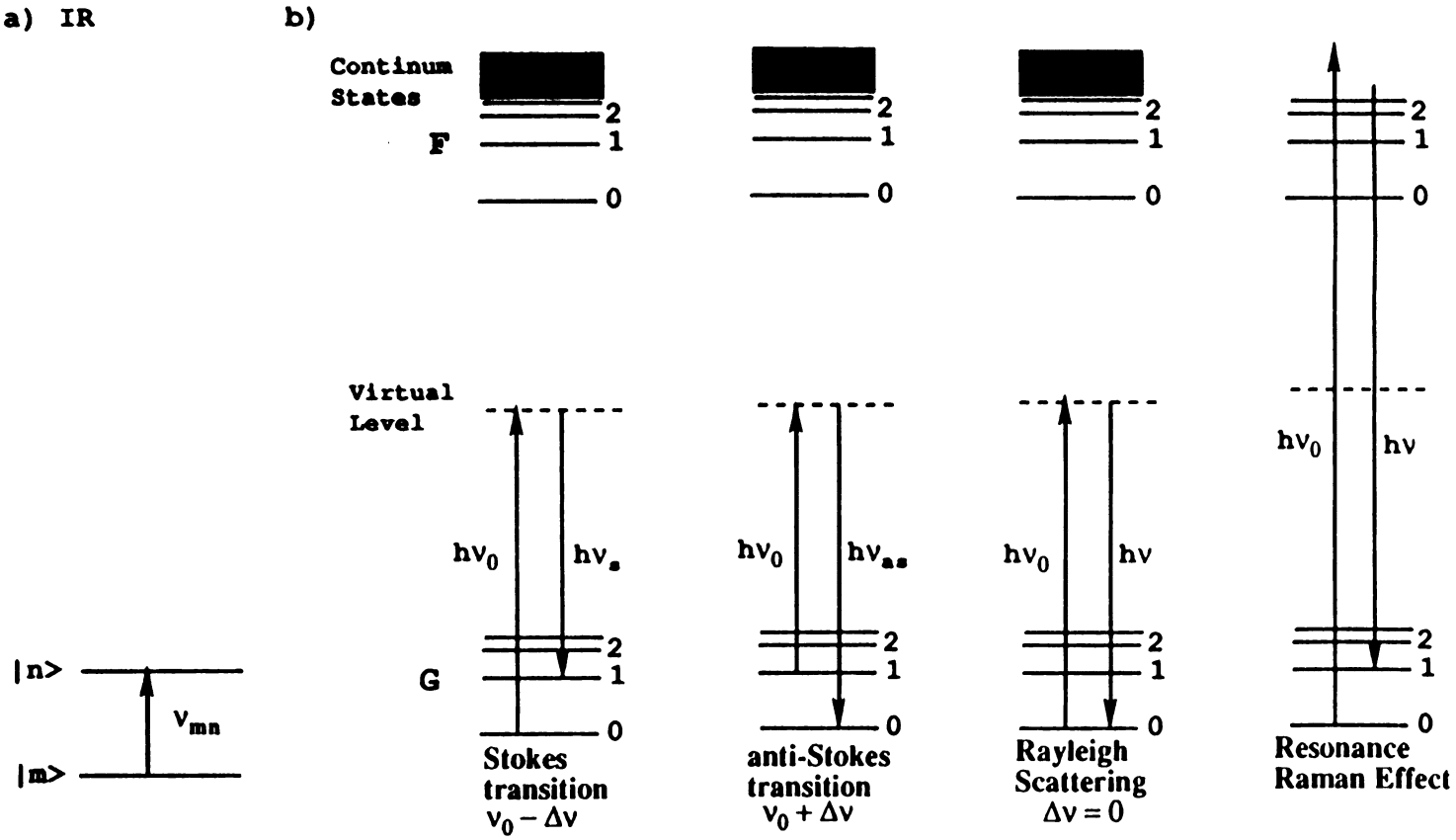

Figure 1-8 Molecular process associated with a) Infrared, and b) Raman spectroscopy.

Transitions between these energy levels occur with absorption or emission.

According to Bohr's rule,

$$\nu_{mn} = (E_n - E_m) / h \qquad \text{(eq. 1-1)}$$

where h is Planck's constant and E_m, E_n are the energy state of $|m\rangle$ and $|n\rangle$. In quantum mechanics a radiative transition can take place only if the integral

$$\int \psi_m \, \mu \, \psi_n \, d\tau \qquad \text{(eq. 1-2)}$$

is not zero, where ψ_m, ψ_n are the wavefunctions associated with the two states (m and n) and μ is the dipole moment operator. It turns out that, when ψ_m and ψ_n are harmonic oscillator wavefunctions, the integral (eq. 1-2) is always zero unless $m - n = \pm 1$. Additionally, the vibrational mode is infrared inactive if there is no change in the molecular dipole moment during the vibration.

The Raman effect is a phenomenon describing the inelastic scattering of electromagnetic radiation by matter. When light scatters off a molecule, the scattered frequency of light will normally be the same as the incident frequency (elastic or Rayleigh scattering). With Raman scattering, incident light of frequency ν_o will result in a gain or loss of energy by the scattered molecules. A simplified diagram describing the Raman scattering process is depicted in Figure 1-8(b). The designations "Stokes" and "anti Stokes"

indicate that the scattered light is of lower or higher frequency, respectively, than the incident light. At room temperature or lower, the Stokes Raman scattering will dominate for most modes, as it originates from the ground vibrational state. The resonance Raman effect is also illustrated as a scattering phenomenon in which the incident photons are of sufficient energy to bridge the gap between the ground state and the electronic excited states. The intensity of the Raman scattering process is given by

$$I_s = (128\pi^5/9c^4) I_o(\nu_s)^4 \Sigma_{\rho\sigma} |(\alpha_{\rho\sigma})_{GF}|^2 \qquad \text{(eq. 1-3)}$$

where I_o is the incident radiation intensity, ν_s represents the frequency of the scattered radiation, and $\alpha_{\rho\sigma}$ is a component of the polarizability tensor (ρ,σ = x,y and z). The polarizability tensor is connected with quantum theory by the Kramers-Heisenberg-Dirac dispersion formula.[23] The polarizability tensor elements in the dispersion formula can be described as:

$$(\alpha_{\rho\sigma})_{GF} = (1/h)\Sigma_E \left\{ \frac{\langle G|\mu_\rho|E\rangle\langle E|\mu_\sigma|F\rangle}{\nu_{EG} - \nu_o + i\Gamma_E} + \frac{\langle G|\mu_\sigma|E\rangle\langle E|\mu_\rho|G\rangle}{\nu_{EF} + \nu_o + i\Gamma_E} \right\} \qquad \text{(eq. 1-4)}$$

where μ_ρ and μ_σ are dipole moment transition operators of polarization direction ρ and σ. $|G\rangle$, $|E\rangle$ and $|F\rangle$ are the wave functions for the ground, excited and final state, and ν_{EG} and ν_{EF} are the frequencies for the transition between the subscripted states. Γ_E is the transition halfwidth, which is a function of the lifetime of the excited state

|E>. The summation runs over all intermediate states, |E>, exclusive of |G> and |F>. The first term in eq. 1-4 is important for the resonance Raman effect. When the incident frequency (ν_o) is very close to the frequency of the electronic transition (ν_{EG}), the intensity will be dominated by the first term as the energy separation $|\nu_{EG} - \nu_o|$ is minimized. This resonance condition results in a substantial enhancement of the intensity of Raman scattering compared to non-resonance (or normal) Raman scattering.

In eq. 1-4 |G>, |F> and |E> represent the wave functions associated with the total (vibrational and electronic) Hamiltonian of the system. By making the Born-Oppenheimer approximation, the vibronic states can be represented as products of pure vibrational states and pure electronic states. As a result, the expression for the polarizability tensor[24] is given by eq. 1-5.

$$(\alpha_{\rho\sigma}) = A + B + \cdots \qquad \text{(eq. 1-5)}$$

$$A = |M_{GE}(R_o)|^2 \Sigma_k \left\{ \frac{\langle n|k\rangle\langle k|m\rangle}{\nu_{EG} - \nu_o - i\Gamma_E} \right\}$$

$$B = M_{GE}(R_o) \left\{ \frac{\partial M_{GE}}{\partial R_k} \right\}_{R_o} \Sigma_k \left\{ \frac{\langle n|R|k\rangle\langle k|m\rangle + \langle n|k\rangle\langle k|R|m\rangle}{\nu_{EG} - \nu_o - i\Gamma_E} \right\}$$

$$M_{GE}(R_o) = \langle G|\mu_\sigma|E\rangle$$

where |n>, |k> and |m> represent the vibrational levels in the initial, excited and final state, respectively. A in the polarizability expression involves no vibronic coupling

between electronic manifolds and is known as the Albrecht A-term. Since the vibrational integrals in the A-term scattering are simple overlap integrals, this mechanism is sometimes referred to as Franck-Condon scattering.

Franck-Condon scattering intensity is determined by three factors: the transition moments M_{GE}, the Franck-Condon overlap intergals, and the frequency dependence of the resonance denominator. The Franck-Condon factors are only non-zero if the orthogonality is removed between a ground state vibrational level and an excited state vibrational level. The removal of orthogonality can be achieved by a difference of vibrational frequency between the ground and excited states or a displacement of the potential energy mininum in the excited state. Because it is usual to assume a common frequency for ground and excited states, vibrational frequency differences between ground and excited states are generally thought to be ineffective in producing non-zero Franck-Condon factors. Accordingly, displacement of the potential energy mininum in the excited state is the predominant cause of A-term intensity and therefore only totally symmetric modes give rise to A-term scattering.[25]

The B term is called the Albrecht B-term or Herzberg-Teller scattering term. Scattering via this mechanism results from vibronic borrowing of intensity between the resonant electronic transition and a nearby electronic transition through $\left\{\frac{\partial M_{GE}}{\partial R_k}\right\}_{R_O}$. Both symmetric and nonsymmetric

modes can be enhanced by B-term mechanisms. But the magnitude of B-term enhancement of symmetric modes is small compared with that of A-term enhancement. In the B-term mechanism, the harmonic oscillator matrix elements $\langle n|R|k\rangle = \delta_{n,k\pm1}$, i.e., modes along which there is no displacement of the potential energy mininum in the excited state will have non-zero integrals. Therefore, non-totally symmetric modes are enhanced by the B-term mechanism.[25]

Resonance Raman studies of porphyrins have revealed an important correlation between the spin and the oxidation states of the central metal. The resonance Raman scattering for porphyrins obtained with Soret excitation is dominated by the Franck-Condon mechanism. The vibrational modes of metalloporphyrins between 1450 and 1700 cm^{-1} represent mainly C-C and C-N stretching modes of the metalloporphyrins. The frequencies of modes in this region that involve the C_aC_m and the C_bC_b bonds have been shown to exhibit a linear correlation with core-size (distance between the central metal and the nitrogen of pyrrole).[26-29] The core-size expansion produces a deformation of the $C_aC_mC_a$ bond angles while the pyrrole rings keep their structural integrity. The increase of the C_aC_m bond length is reflected by a lowering of the corresponding vibrational frequency. Therefore, modes with C_aC_m stretching character are more sensitive to core-size change than are the modes with primarily C_bC_b stretching character. Determination of the core-size sensitivity by using resonance Raman provides a

useful means of assigning vibrational modes in the metalloporphyrin systems. For the C_aN symmetric vibration in the 1355 - 1375 cm^{-1} region, the frequency is sensitive to electron density in the porphyrin π^* orbitals. Therefore, the frequency of the C_aN symmetric vibration is determined to a significant extent by the oxidation state of the metal and the presence of axial ligands.

The resonance Raman scattering for porphyrins obtained with visible excitation are dominated by the Herzerg-Teller mechanism owing to mixing and borrowing of intensity between the resonant electronic transition (Q band) and the Soret band.[25] Therefore, the totally symmetric modes, which give rise to polarized bands, are weak or absent in visible excitation spectra. On the other hand, non-totally symmetric modes, which show depolarized or anomalously polarized bands, are strongly enhanced.[25]

CHAPTER 2

MATERIALS AND METHODS

2.1) Preparation of Porphycenes

All of the porphycenes used in the studies reported were prepared by Weishih Wu (Michigan State Univ.) according to the procedures below.

The free base 2,7,12,17-tetrapropylporphycene (H_2PPC) was made according to the method of Vogel et al.[4] The metal insertion procedures for Ni^{II} and Cu^{II} were described earlier.[30] Selective deuteration at the C_e position (Figure 1-2), NiPPC-9,10,19,20-d_4 (abbreviated NiPPC-d_4(et)), was synthesized according to the published method.[30] Deuteration at the $C_{b'}$ positions, NiPPC-3,6,13,16-d_4 (NiPPC-d_4(py)) was accomplished by refluxing H_2PPC deuterated acetic acid in the presence of nickel acetate and sodium acetate under nitrogen atmosphere for 8 hours.

3,6,13,16-tetrabromo-2,7,12,17-tetrapropylporphycene, which involves bromination at the $C_{b'}$ positions (Figure 1-2), was achieved by the following method. A solution of bromine in chloroform was slowly added to a stirred solution of the free base porphycene. The yield of mono-, di-, tri-, and tetrabromoporphycene depended on the amount

of bromine added. The reaction was easily monitored by TLC developed with hexane/CH_2Cl_2. The Ni(II) and Cu(II) complexes were prepared in the same manner as described above.

In order to synthesize iron(III) tetrapropylporphycene chloride ($ClFe^{III}PPC$), ferric chloride (30 mg) and sodium acetate (5 mg) were added to a solution of the free base porphycene (30 mg) in acetic acid (20 ml) and refluxed for 10 hours. The organic layer was separated, washed with water and evaporated. The residue was run on a silica gel column and eluted with methylene chloride to first remove by-products and then with MeOH(2 %)/CH_2Cl_2 to collect the dark-green iron(III) complex. $(Im)_2Fe^{III}PPCCl$ was produced by titration of the ferric chloride complex with N-methylimidazole (Im). To reduce the $(Im)_2Fe^{III}PPCCl$ chemically, a CH_2Cl_2 solution of $(Im)_2Fe^{III}PPCCl$ was made anaerobic by several freeze-pump-thaw cycles and titrated with hydrazine hydrate.

2.2) Preparation of Chlorins

All of the chlorins used in the studies reported below were prepared by Einhard Schmidt (Michigan State Univ.). Chlorins were prepared by the method of Whitlock et al.[31]; following the reduction reaction, residual porphyrin was removed by alumina column chromatography with benzene as eluent. H_2OEC-d_4 was prepared by treatment of H_2OEC with D_2SO_4/D_2O (9:1, v/v). Reduction of the D_2SO_4/D_2O ratio to 6:1 (v/v) afforded H_2OEC-γ,δ-d_2. Re-exchange at the γ and δ

positions of H_2OEC-d_4 with H_2SO_4/H_2O (6:1, v/v) produced $H_2OEC-\alpha,\beta-d_2$. The deuteration process was followed and confirmed by ^{1}HNMR by using a Varian VXR-300s NMR spectrometer. Metal insertion was achieved by dissolving the chlorin in CH_2Cl_2 and adding an appropriate volume of saturated zinc or copper acetate in MeOH. The process was followed by UV-vis spectroscopy with a Shimadzu UV-160 spectrometer.

2.3) Spectroscopic Studies

UV-visible absorbance measurements were recorded on a Perkin Elmer Lamda 5 UV/Vis Spectrometer. Optical spectra were recorded before and after the Raman experiments to confirm the stability of each particular complex to the laser irradiation employed.

Spectrophotometric grade $CHCl_3$ and CH_2Cl_2 were purchased from Aldrich company. Both solvents were purified by the method of Perrin & Perrin[32] in which the solvent of interest is stirred with concentrated H_2SO_4 overnight. The organic layer is washed with H_2O twice, 10 % $NaHCO_3$ once, and again washed with H_2O twice. The solvent is dried over $CaCl_2$, and then distilled from P_2O_5.

Infrared spectra at room temperature were recorded on a Nicolet IR/42 FTIR spectrometer. Samples were prepared by saturating $CHCl_3$ with the various metal chlorins, then running the spectra in a 50μ pathlength NaCl cavity cell obtained from Spectra Tech, Inc.

Resonance Raman spectra were obtained on a computer-controlled Spex 1401 Ramalog with PMT detection, a Spex 1877 Triplemate with EG&G Model 1420 detector and OMA II electronics, and a Spex 1877 B outfitted with a EG&G Model 1421 detector and OMA III computer. The laser systems include a Spectra Physics Model 164 argon ion and model 375 dye laser (to provide wavelengths of 630.0 and 613.0 nm), a Coherent Innova 100 argon (363.8 nm) and an Innova 90 krypton(568.2 and 406.7 nm) ion laser, and a Quanta Ray DCR-2A Nd:YAG and PDL-2 dye laser combination (390.0 and 355.0 nm). Spectra were obtained for CH_2Cl_2 solution of the metallochlorins or porphycenes, which were contained in a cylindrical quartz spinning cell. Long exposure (more than 20 min) of the metallochlorins to high power laser beams (e.g., $\geq$ 15 mW at 406.7 nm) caused sample degradation. Therefore, the Raman spectra of the metallochlorins were collected within 1 minute of initiating low power laser irradiation (e.g., ~ 7 mW at 406.7 nm) with a Spex 1877 Triplemate with a EG&G Model 1420 diode array detector in order to avoid sample degradation. All of Raman spectra were taken under aerobic conditions at room temperature.

Laser powers and concentrations used for specific spectra are noted in the figure captions.

CHAPTER 3

ELECTRONIC AND VIBRONIC PROPERTIES OF METALLOPORPHYCENES

3.1) Introduction

Porphycene is a structural isomer of porphine, the parent compound of porphyrins. Porphycenes qualify as potential agents for tumor marking and photodynamic therapy owing to their high absorption intensity in the wavelength region above 620 nm, in which body tissue is translucent, and to their stability towards photooxidation and singlet oxygen sensitization.[33-35] For these reasons the electronic properties of porphycenes are of interest. Figure 1-2 represents the structure of 2,7,12,17-tetrapropylporphycene.

Several groups have executed systematic studies of the effects of symmetry lowering on the macrocyclic vibrational properties of metallooctaethylchlorins(MOEC)[26,36-38] and metallopheophorbides[39] to understand vibrational spectra of naturally occurring pigments (e.g. chlorophyll) possessing tetrapyrrole-derived structures of symmetry lower than that of metallooctaethylporphyrin. Similarly, the spectroscopic properties of metal complexes of bacteriochlorins and bacteriopheophorbides[40-41] should progressively approach

those of bacteriochlorophyll. In this spirit, metalloporphycene represents an example of a macrocycle of true D_{2h} symmetry which is approximated by heme a[42] and metallobacteriochlorins.[41] Furthermore, the bipyrrole C_a-C_a' bond is a structural feature of the corrin macrocycle; thus, cobalt complexes of porphycene derivatives may model some aspects of vitamin B_{12}. Renner et al.[30] have characterized the NiPPC anion radical and compared the redox properties of this compound to other nickel porphinoid models of coenzyme F_{430} from methanogenic bacteria.

Resonance Raman spectroscopy (RR) has been applied extensively to synthetic MOEP[43], MOEC[26,36-39], metallobacteriochlorins[40-41], and metallocorphinoids.[44] It has been used to study redox-altered states of MOEP and MOEC including π cation[45-49] and anion[50-52] radicals. The studies of these model compounds have contributed to our understanding of resonance Raman results from a number of important biological systems including heme proteins[53], reaction center chlorophyll and bacteriochlorophyll[54-55], coenzyme F_{430}[56-57] and vitamin B_{12}.[58-59] A range of information regarding structure and electronic properties can be offered by the resonance Raman technique. Moreover time-resolved resonance Raman techniques have provided substantial insight in the study of dynamic processes. Interpretation of results from complex biological systems and from sophisticated techniques requires thorough grounding in basic spectroscopic study. For these reasons the UV visible and resonance Raman spectra

of metal-substituted and selectively deuterated porphycene compounds are investigated and compared to the well known spectra of analogous octaethylporphyrin species.

3.2). Results

3.2.1) Electronic Absorption Spectra

Figure 3-1 shows the electronic absorption spectrum of CuPPC and, for comparison, the spectrum of the analogous porphyrin compound, CuOEP (inset). Superficially, the optical spectrum of CuPPC is similar to that of the porphyrin series. However, the oscillator strength ratio, which was determined by measuring the areas under the Soret and visible bands for the absorption spectra plotted in a wavenumbers scale, of CuPPC is much greater (more than 5 times) than that of CuOEP. Additionally, the near-UV band of CuPPC is noticeably split into two components. Compared to that of CuOEP, this band is blue shifted and the visible band is red-shifted in the CuPPC spectrum. Figures 3-2 and 3-3 show absorption spectra of NiPPC and CuPPC. In order to demonstrate the spectral features of these compounds more clearly, the first derivative of each spectrum is superimposed. Table 3-1 collects the band positions determined by inspection of expanded spectra, as well as of first and second derivative spectra of NiPPC and CuPPC. Also included are band positions for the Cu^{II} complex of 3,6,13,16-Br_4PPC (i.e. Br is substituted for H at the $C_{b'}$ positions, Figure 1-2). These are compared to absorption maxima for the following

Figure 3-1 UV-visible absorption spectra of CuPPC and CuOEP (inset) in CH_2Cl_2 solution.

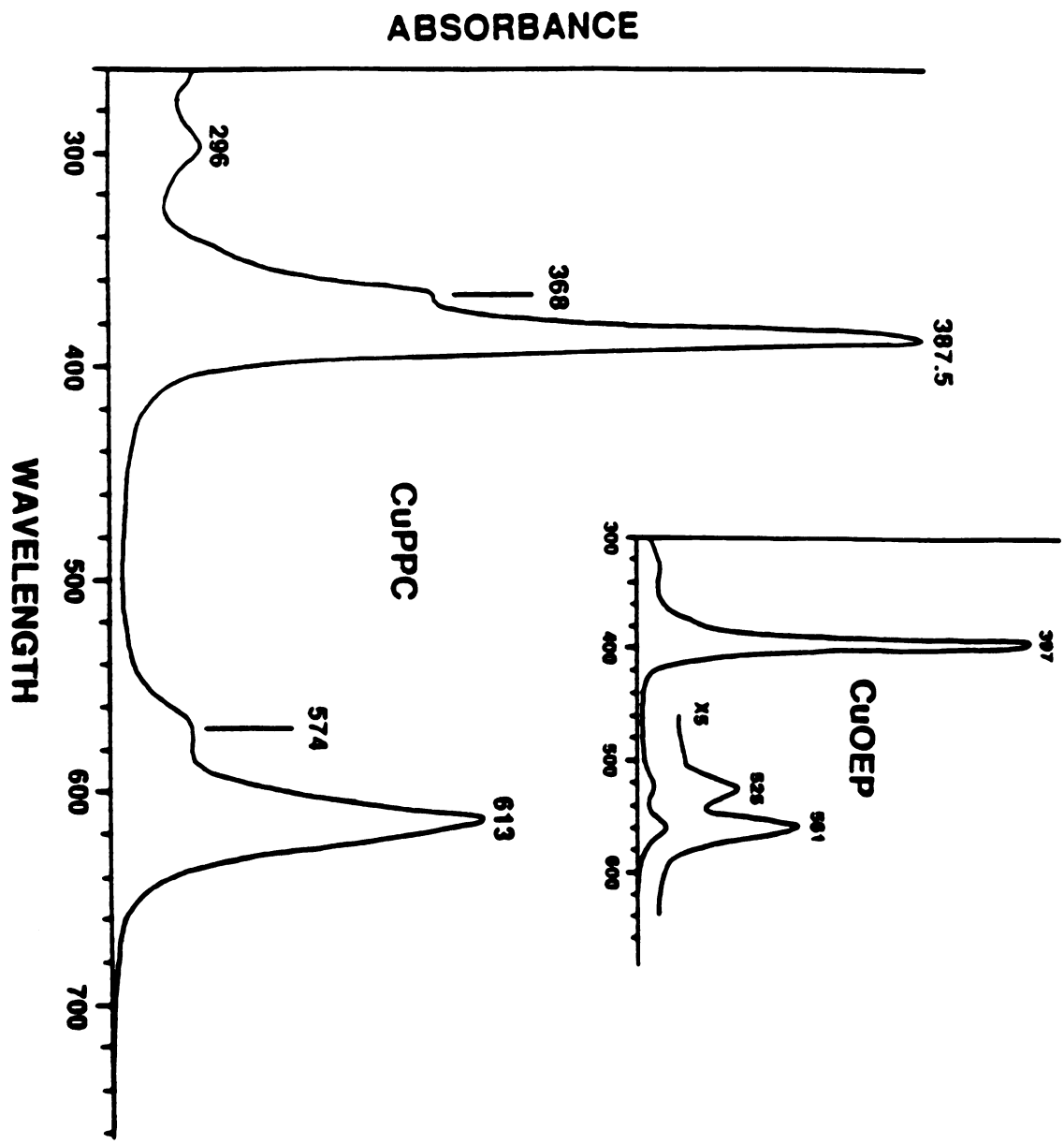
ABSORBANCE
WAVELENGTH
300
400
500
600
700
296
368
387.5
574
613
CuPPC
387
CuOEP
XS
555
561

Figure 3-2 UV-visible absorption (dashed curve) and first derivative (solid curve) absorption spectra of CuPPC in CH_2Cl_2 solution.

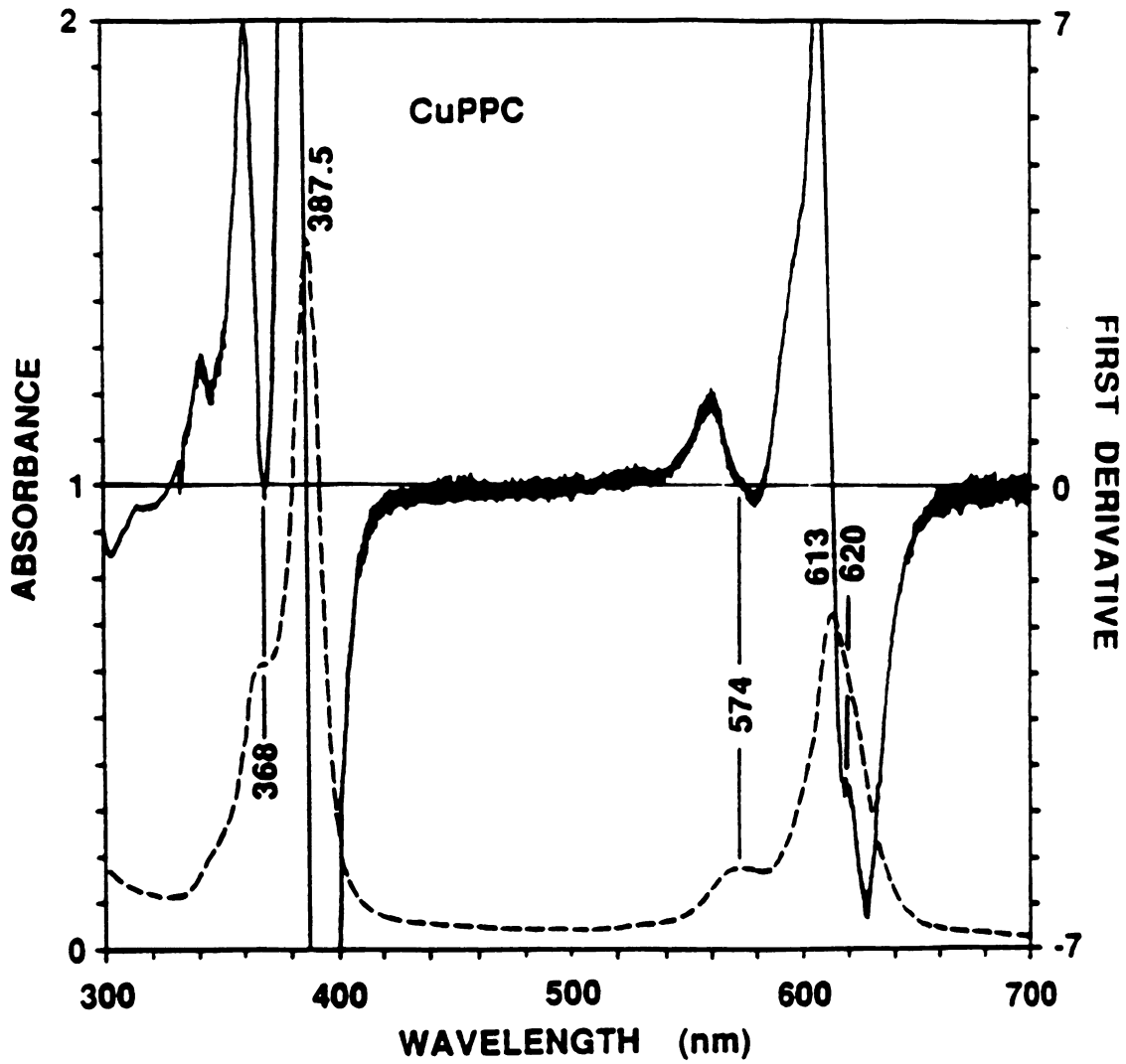
CuPPC
387.5
368
574
613
620
ABSORBANCE
FIRST DERIVATIVE
WAVELENGTH (nm)
2
1
0
7
0
-7
300
400
500
600
700

Figure 3-3 UV-visible absorption (dashed curve) and first derivative absorption (solid curve) spectra of NiPPC in CH_2Cl_2 solution.

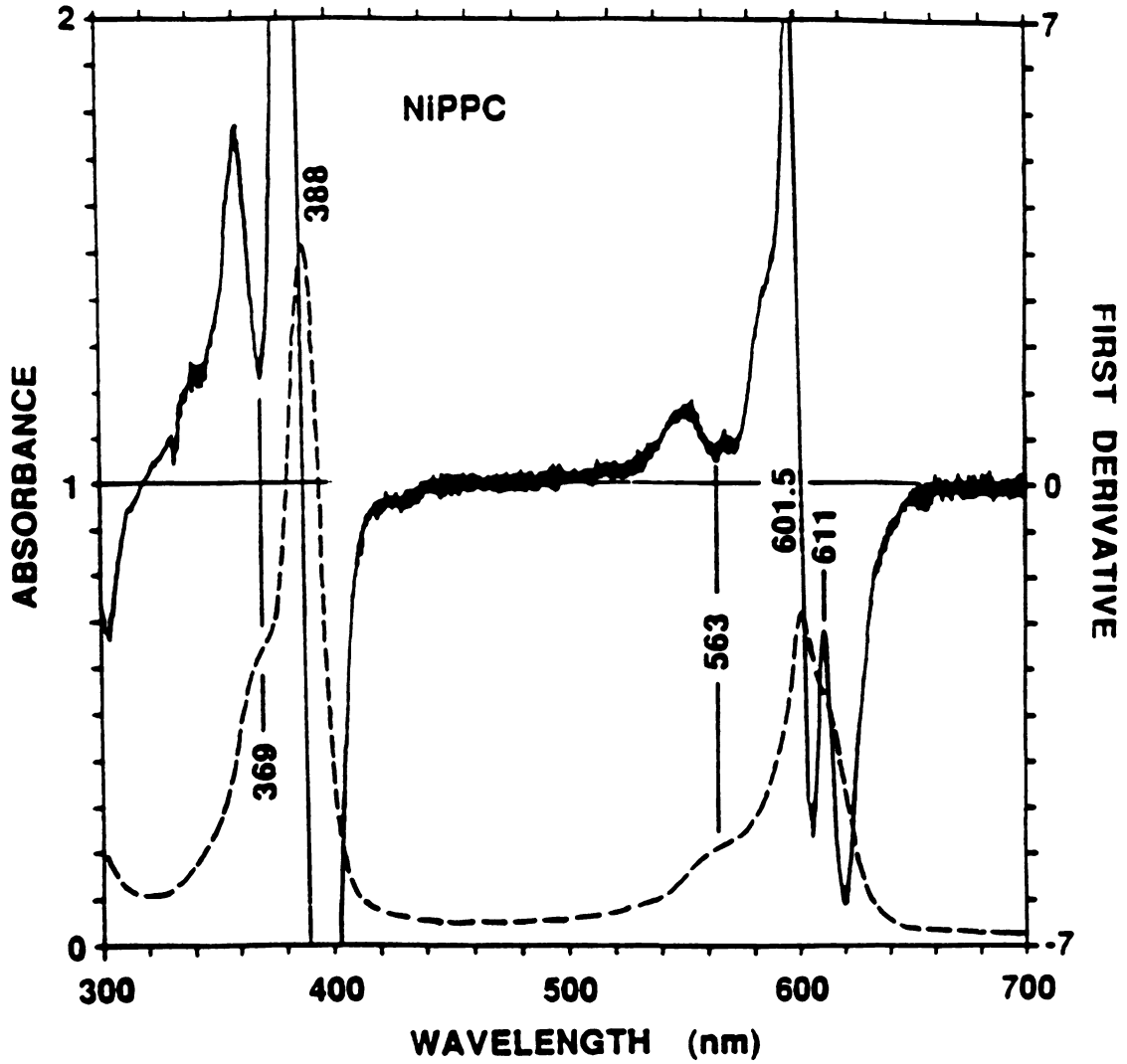
NiPPC
388
369
563
601.5
611
ABSORBANCE
FIRST DERIVATIVE
WAVELENGTH (nm)
2
1
0
7
0
-7
300
400
500
600
700

Table 3-1. UV-Visible Absorptions (nm) of Metalloporphycenes and Metalloporphyins and Assignment of Electronic Transitions of MPPC

NiPPC[a]	CuPPC	Cu-Br_4PPC	one electron ψ	symmetry
601.5	613	631	$b_{1u}b_{2g}$	$B_{3u}(x)$
563 (sh)	574	586	$b_{1u}b_{3g}$	$B_{2u}(y)$
388	387.5	388	$a_u b_{2g}$	$B_{2u}(y)$
369 (sh)	368 (sh)	369 (sh)	$a_u b_{3g}$	$B_{3u}(x)$

NiOEP[b]	CuOEP	NiDPDME[c]	Ni-2,4-Br_2DPDME
551	561	549.5	553
516	525	514	518
391	397	390.5	395

[a]Band positions of CH_2Cl_2 solution were determined by inspection of expanded spectra, as well as from first and second derivative spectra.

[b]Band positions of CH_2Cl_2 solution were determined from multiple runs of each absorption spectrum.

[c]Band positions of $CHCl_3$ solution as reported in ref. 60, 61.

porphyrin complexes: NiOEP, CuOEP, NiDPDME, and Ni-2,4-BrDPDME (DPDME=deuteroporphyrin IX dimethyl ester). Table 3-1 illustrates that a change in the central metal or bromination at the ring periphery significantly shifts both the near-UV (Soret) and visible bands in the porphyrin complexes; however, these substitutions in the porphycene complexes shift only the visible bands and leave the near-UV band positions virtually unchanged. This illustrates a basic difference in the electronic properties of metalloporphycenes and metalloporphyrins and will be discussed later in this chapter.

Figure 3-4 illustrates the UV-visible spectral changes manifested during conversion of the five-coordinate ferric chloride complex to a 6-coordinate ferric bis(N-methyl imidazole), $(Im)_2$, complex. The spectrum of $(Im)_2$FePPCCl (Figure 3-4) is quite similar to that of CuPPC (Figure 3-1), however, the structure in the near-UV band is less well resolved. The ClFe^{III}PPC spectrum is more complex than that of $(Im)_2Fe^{III}$PPCCl. Reduction of the $(Im)_2Fe^{III}$PPC to $(Im)_2Fe^{II}$PPC with hydrazine hydrate generates the UV-visible spectrum inset in Fig.3-4.

3.2.2) Resonance Raman Spectra

Fig.3-5 represents the Raman spectra obtained in resonance at 363.8 nm of CuOEP and CuPPC. Like the optical absorption spectra, there are superficial similarities. Both are dominated by intense features in the 1300-1650 cm^{-1}

Figure 3-4 UV-visible absorption spectra of FePPC derivative in CH_2Cl_2 solution. The ferrous sample was prepared using hydrazine hydrate as a reductant as described in MATERIALS and METHODS. The absorption at 280 nm in the spectrum of the $(Im)_2Fe^{III}PPC$ is from excess N-methylimidazole.

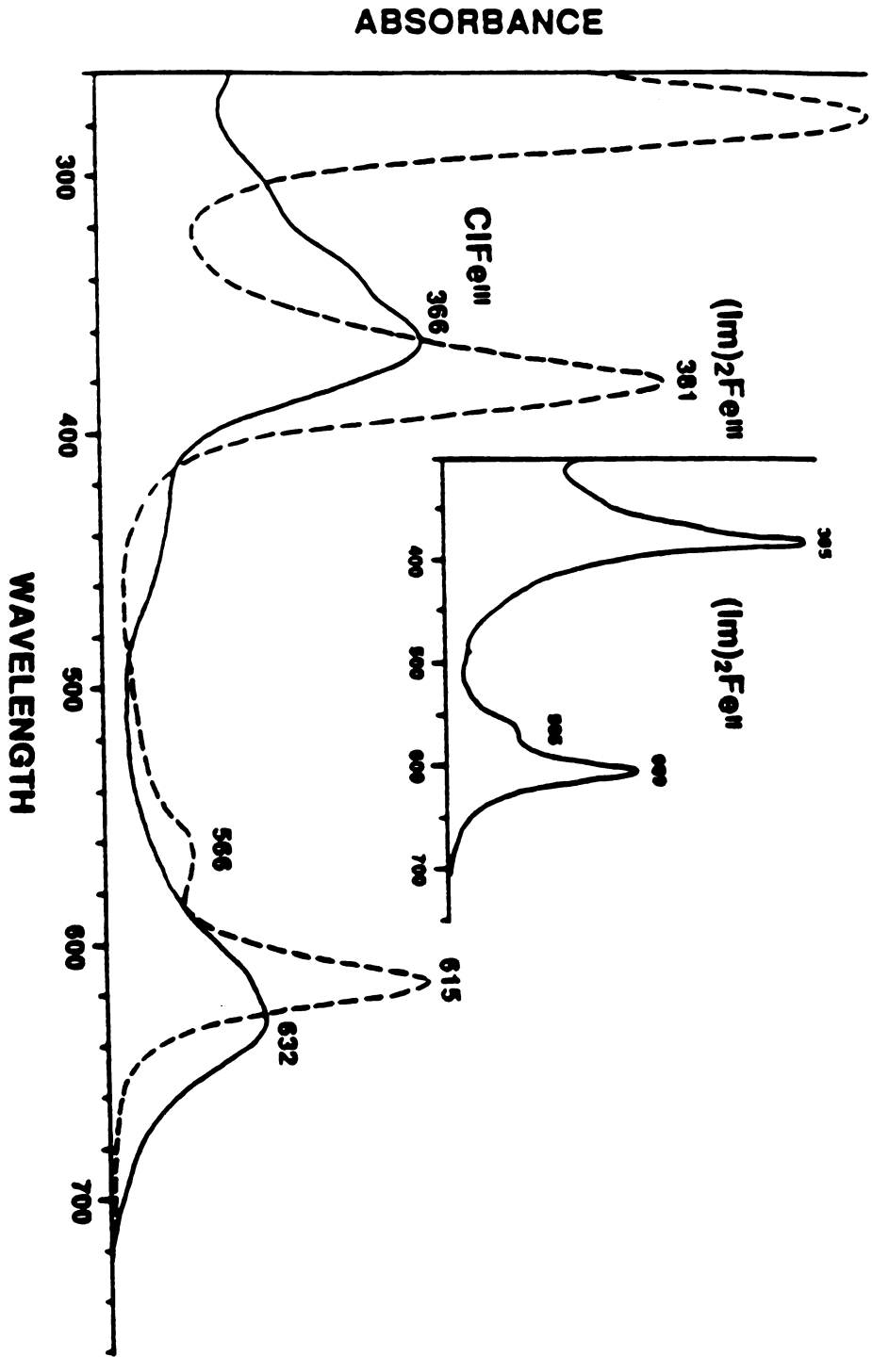
ABSORBANCE
WAVELENGTH
300
400
500
600
700
ClFe^{III}
366
(Im)$_2$Fe^{III}
381
(Im)$_2$Fe^{II}
566
615
632

Figure 3-5 Resonance Raman spectra of CuOEP and CuPPC in CH_2Cl_2 solution at concentration of approximately 0.1 and 0.2 mM, respectively. Laser powers at 363.8 nm were 20 and 10 mW, respectively. Asterisks(*) in Figures 3-5, 6, 7 and 8 represent solvent vibrations.

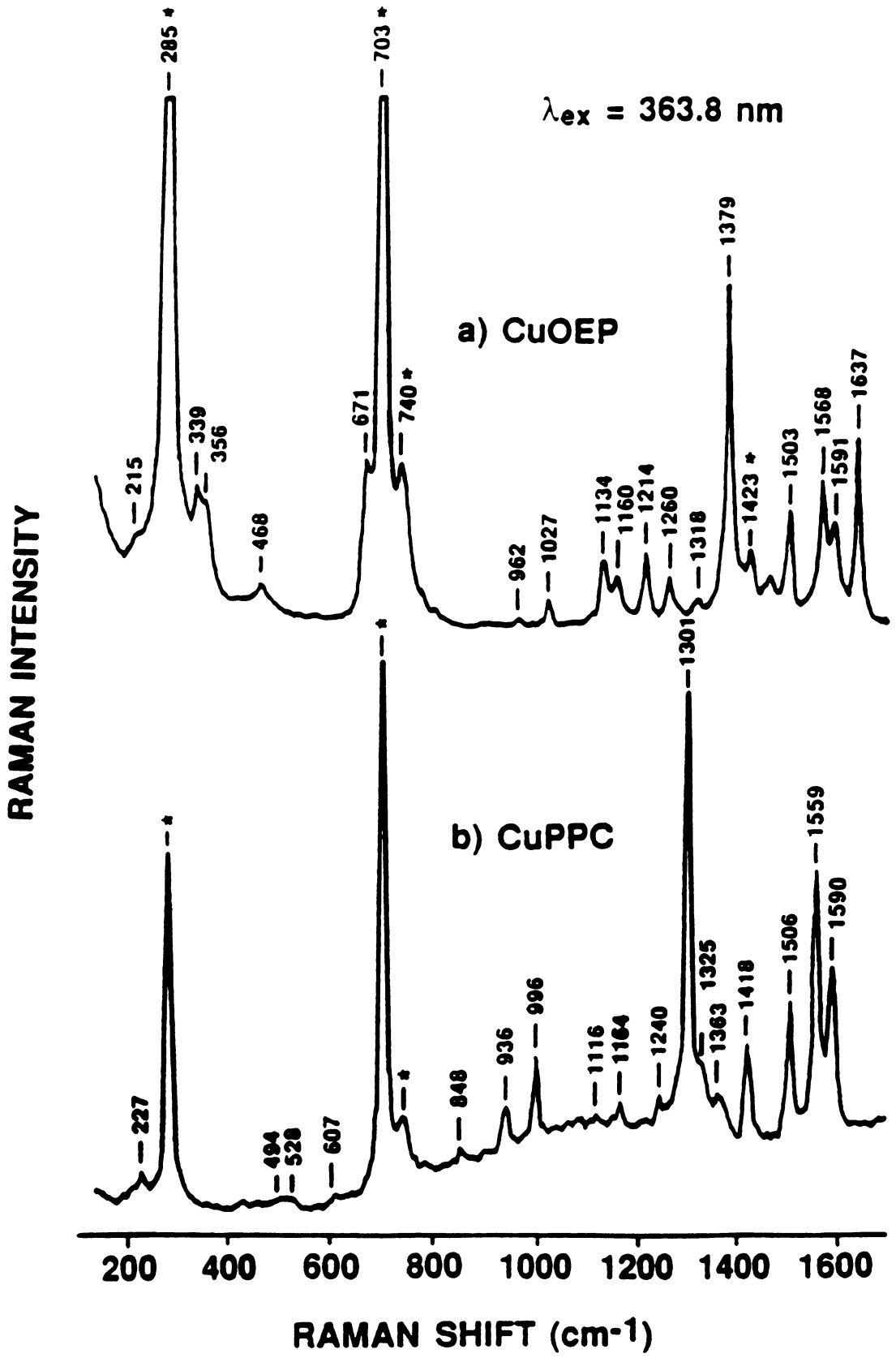
λex = 363.8 nm
a) CuOEP
b) CuPPC
RAMAN INTENSITY
RAMAN SHIFT (cm-1)
285 *
703 *
740 *
215
339
356
468
671
962
1027
1134
1160
1214
1260
1318
1379
1423 *
1503
1568
1591
1637
227
484
528
607
848
936
996
1116
1164
1240
1301
1325
1363
1418
1506
1559
1590
200
400
600
800
1000
1200
1400
1600

region. In the CuOEP complex these normal modes involve C-C and C-N stretching coordinates. Their large intensity is attributed to large displacement along these normal coordinates in the $\pi \rightarrow \pi^*$ excited states of the porphyrin macrocycle. The frequencies of these vibrations are structure sensitive, i.e. they are dependent on the size and redox state of the central metal. The normal coordinate analyses[60-64] of NiOEP and CuOEP indicate that the dominant Raman-active high frequency normal mode of CuOEP (Figure 3-5) include two primarily $\nu C_a C_m$ stretches, ν_{10}(1637 cm^{-1}, b_{1g}) and ν_3(1503 cm^{-1}, a_{1g}), and two primarily $\nu C_b C_b$ stretching motions, ν_2(1591 cm^{-1}, a_{1g}) and ν_{11}(1568 cm^{-1}, b_{1g}). The ν_4(1379 cm^{-1}, a_{1g}) mode of metalloporphyrins is predominantly a $\nu C_a N$, $\delta C_a C_m$ "breathing" motion of the macrocycle.

Figure 3-6 shows polarized RR spectra from CuPPC that were obtained by using laser excitation at 406.7 and 613.0 nm. Similar spectra were measured with λ_{ex} = 568.3 and 630 nm, and depolarization ratios for the most intense bands are collected in Table 3-2 in order to determine the symmetry of the principle vibrations of the CuPPC spectrum.

Figure 3-7 shows the RR spectra of NiPPC, NiPPC-d_4(py), and NiPPC-d_4(et). The latter two complexes have deuterium substituted for hydrogen at the C_b, pyrrole positions and at the C_e ethylene positions, respectively. The frequencies of the Raman bands are collected in Table 3-3 along with those measured for CuPPC and CoPPC.

Figure 3-6 Polarized resonance Raman spectra of CuPPC in CH_2Cl_2 solution at 406.7 nm and 613.0 nm. Concentrations were approximately 0.5 mM and 0.3 mM and laser powers 40 and 100 mW, respectively. In each spectrum, the top trace represents $I_{\parallel}$ and the bottom trace represents $I_{\perp}$.

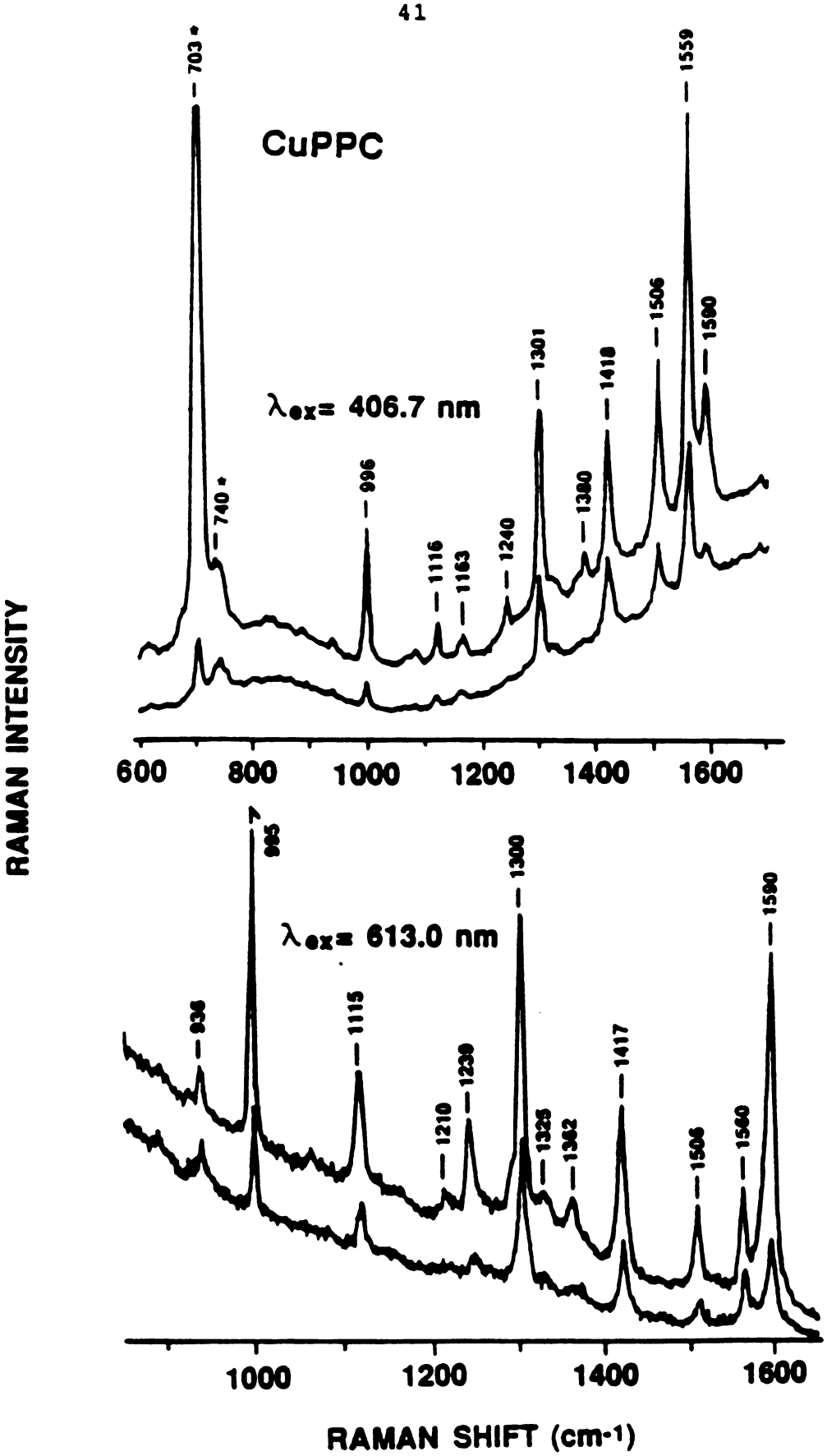
CuPPC
λex= 406.7 nm
703 *
740 *
996
1116
1163
1240
1301
1380
1418
1506
1580
1559
600
800
1000
1200
1400
1600
λex= 613.0 nm
938
995
1115
1210
1230
1300
1325
1382
1417
1506
1540
1590
1000
1200
1400
1600
RAMAN INTENSITY
RAMAN SHIFT (cm-1)

Table 3-2 Resonance Raman Depolarization Ratios, $\rho=I_{\perp}/I_{\parallel}$, for CuPPC.

Raman shift (cm^{-1})	Excitation Wavelengths, λ_{ex} (nm) 406.7	568.2	613.0	630.0
1590	0.3	0.2	0.2	0.3
1559	0.4	0.5	0.5	0.4
1506	0.4	0.3	0.3	0.3
1417	0.5*	0.4	0.5	0.5
1363(w)	0.1	(w)	0.4	(w)
1326	(w)	(w)	0.4	(w)
1301	0.5	0.4	0.5	0.4
1240	0.2	(w)	0.2	0.3
1165	0.6*	(w)	(w)	(w)
1116	0.3	0.3	0.4	0.4
1065	0.5	(w)	(w)	(w)
996	0.2	0.3	0.3	0.3
936	(w)	0.6	1.0(w,?)	1.0(w,?)

*; Indicates that the ρ value may be anomalously high due to contribution from an underlying depolarized solvent band.

w; Weak intensity making measurement of ρ unreliable.

Figure 3-7 Resonance Raman spectra of NiPPC derivatives in CH_2Cl_2 solution at concentration of approximately 0.2 mM. Laser power at 363.8 nm was 30 mW.

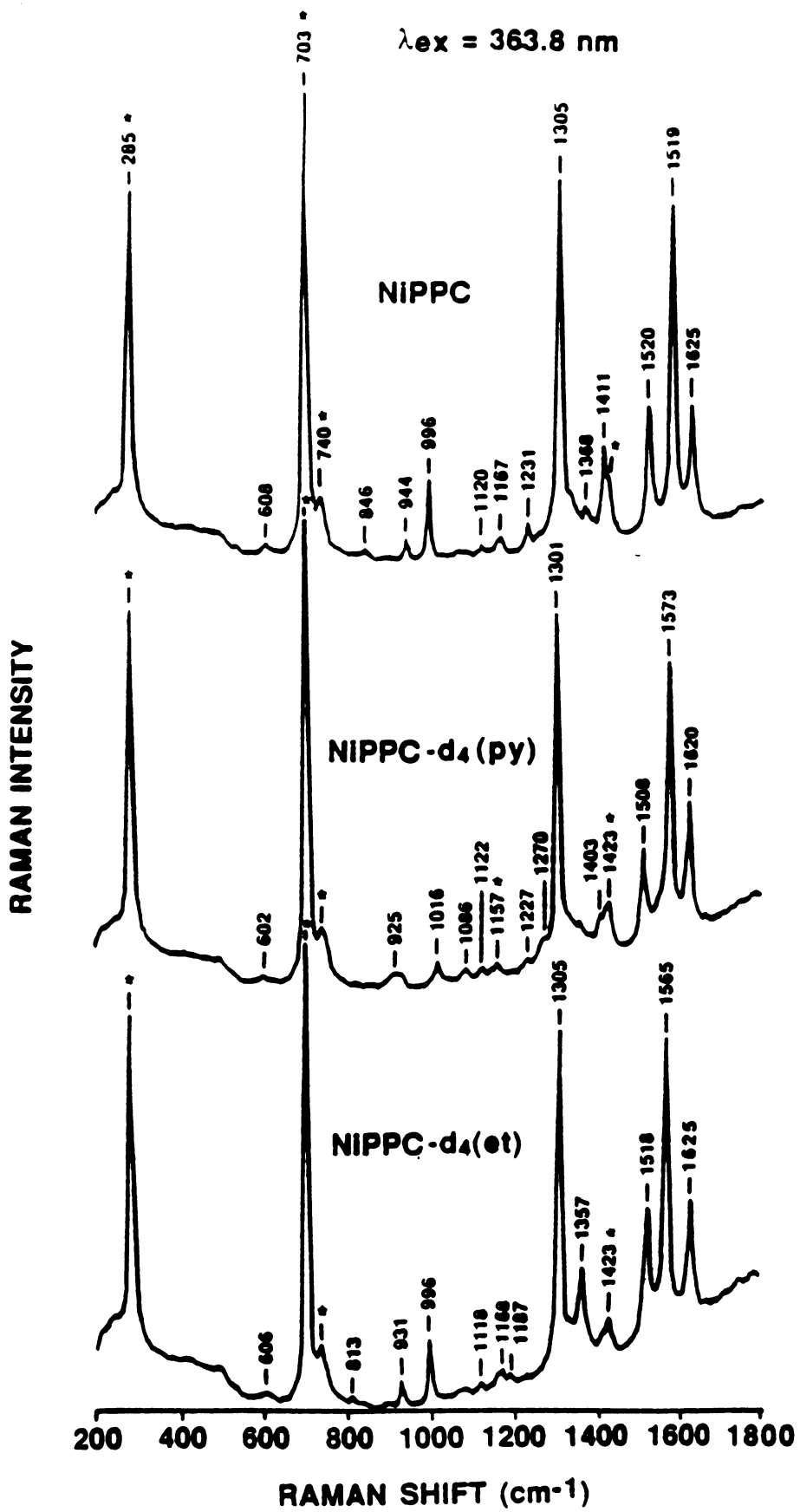
λex = 363.8 nm
NiPPC
NiPPC-d4(py)
NiPPC-d4(et)
RAMAN INTENSITY
RAMAN SHIFT (cm-1)
200
400
600
800
1000
1200
1400
1600
1800

Table 3-3 Raman Vibrational Frequencies (cm^{-1}) of $M^{II}PPC$ Complexes.

[a]The CoPPC spectra (not shown) indicated some residual free-base present in the sample. These contributions may skew the frequencies presented here despite efforts to substract them from the data.

[b]These frequencies most likely represent normal mode of significantly different character than those of the natural abundance sample.

S[c] means small.

L[d] means large.

CuPPC	CoPPC[a]	NiPPC	NiPPC-d_4(py)	NiPPC-d_4(et)	Assignment
1590	1612	1625	1620	1625	νCC(py)
1559	1571	1579	1574	1565	νCC(et,py)
1506	1515	1520	1509	1518	νCC(py)
1417	1407	1410	1403	1357	νC_eC_e, δC_eH
1363	1368	1368	1368(w)	1368(w)	νC_aN
1326		1327	1327	1327	νC_aN
1301	1299	1305	1302	1305	νC_aN
			1270[b]		
1240		1231	1227	1187	δC_eH(S[c] %)
1165	1164	1167	925	1167	δC_bH(L[d] %)
1116		1120	1122	1118	
1065(w)		1064(w)			
			1085[b]		
			1016[b]		
996	995	996		996	νC_b-propyl
936	944	944		931	
848		846	~850(w)	813(w)	
607	607	608	602	606	
528					
494(w)					
227					

Figure 3-8 compares RR spectra of the five-coordinate $ClFe^{III}PPC$ and six-coordinate $(IM)_2Fe^{II}PPC$. The RR spectrum excited at 390 nm of the reduced product appears in Figure 3-8c, while the spectrum at λ_{ex} = 355 nm of the same compound in the presence of excess reductant appears in Figure 3-8d. The spectra are consistent with metal-centered reduction.

3.3) Discussion

3.3.1) Electronic Properties

In order to understand the electronic properties of the porphycene macrocycle and to compare them to the porphyrins, the UV-visible absorption spectra of four coordinate, divalent, transition-metal complexes that exist in a single spin state and that do not exhibit metal-macrocycle π bonding will be discussed.

The UV-visible absorption of the metalloporphyrins have been the subject of extensive study for many years. They arise for the most part from in plane $\pi \rightarrow \pi^*$ transitions of the macrocycle which have been described by the four-orbital model of Gouterman.[20-21] His model came from earlier attempts to explain the π-electron spectra of large conjugated ring molecules.[19,65-68] The model adequately explains the effects of variation of the central metal and peripheral substituents on the electronic structure of the macrocyclic complexes. Comparisons of these effects in metalloporphyrin

Figure 3-8 Resonance Raman spectra of Fe^{III} and Fe^{II} complexes of PPC. Concentrations in CH_2Cl_2 solution were approximately 0.1 mM and laser powers typically 20 mW. Spectrum a was measured with a different diode array detector than spectra b-d.

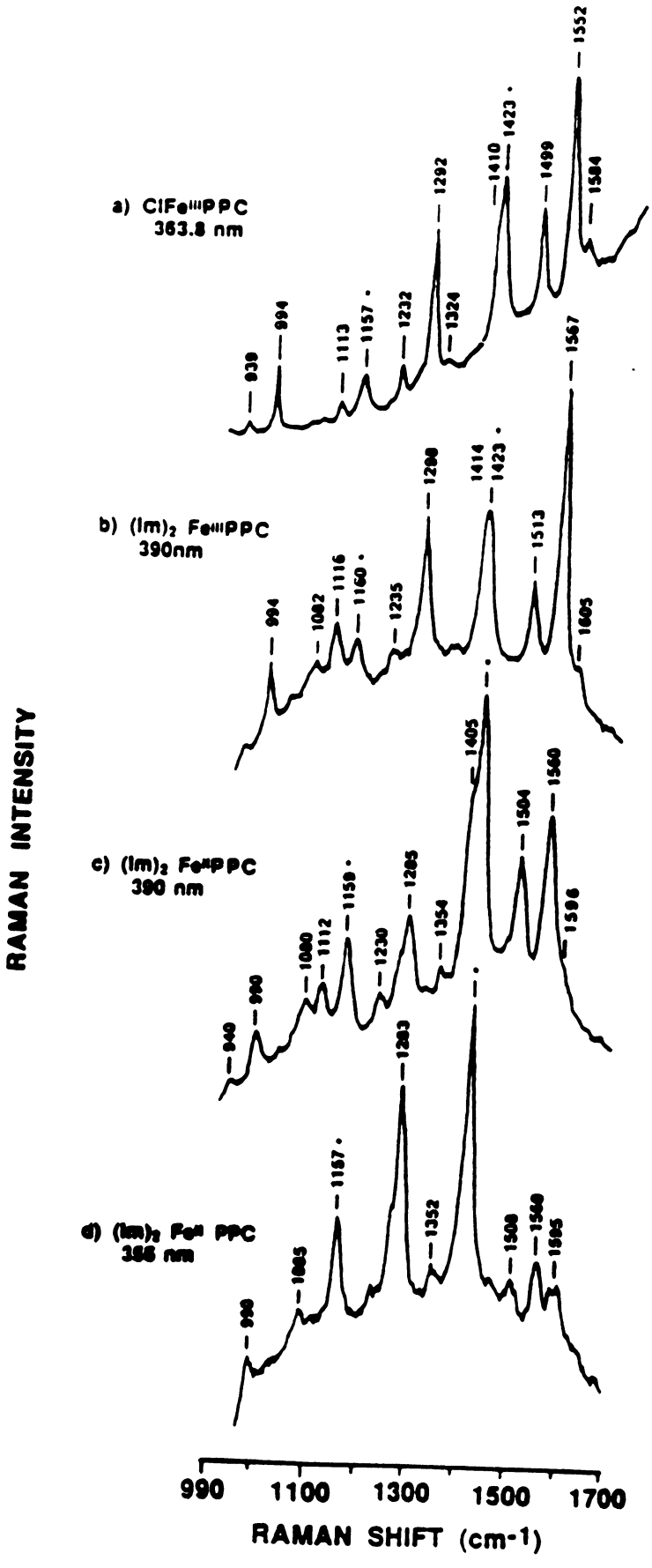
a) ClFe^{III}PPC
363.8 nm
938
994
1113
1157
1232
1292
1324
1410
1423
1499
1552
1584
b) (Im)$_2$ Fe^{III}PPC
390nm
994
1082
1116
1160
1235
1298
1414
1423
1513
1567
1605
c) (Im)$_2$ Fe^{II}PPC
390 nm
940
980
1000
1112
1158
1230
1285
1354
1405
1504
1560
1596
d) (Im)$_2$ Fe^{II} PPC
366 nm
990
1085
1157
1283
1352
1508
1560
1585
RAMAN INTENSITY
990
1100
1300
1500
1700
RAMAN SHIFT (cm-1)

spectra to the corresponding effects in metalloporphycene reveal fundamental differences.

The differences in the electronic properties of metalloporphycene from those of metalloporphyrin are the consequence of the difference in point group symmetry. Figure 3-9 depicts an orbital energy level diagram for both metalloporphyrin (D_{4h}) and metalloporphycene (D_{2h}). For metalloporphyrin four essentially degenerate one electron excited state wave functions are heavily mixed by configuration interaction (CI) resulting in linear combinations usually referred to as the Q (visible) and B (Soret) states.[20-21] These are of $E_u(x,y)$ symmetry. The Q state transition is formally forbidden but gains intensity through vibronic coupling to the B state, which represents an allowed transition. In D_{4h} metalloporphyrins the x and y components of the Q and B states are degenerate, and each total wave function involves all four one-electron wave functions. The configuration interaction comes about primarily because the HOMO energy splitting is small compared to the electron interaction energy. The latter can be estimated by the observed energy difference between the B and Q transition energies and, from the data in Table 3-1, is ~7300 cm^{-1} for CuOEP. Shelnutt[69-70] estimates the energy difference between the a_{1u} and a_{2u} orbitals of CuOEP to be ~1700 cm^{-1}. As a consequence of the electronic configuration, the spectral effects of substitution at the metal center or at the pyrrole periphery change both the Q

Figure 3-9 Schematic orbital energy level diagrams for CuOEP(D_{4h}) and CuPPC(D_{2h})

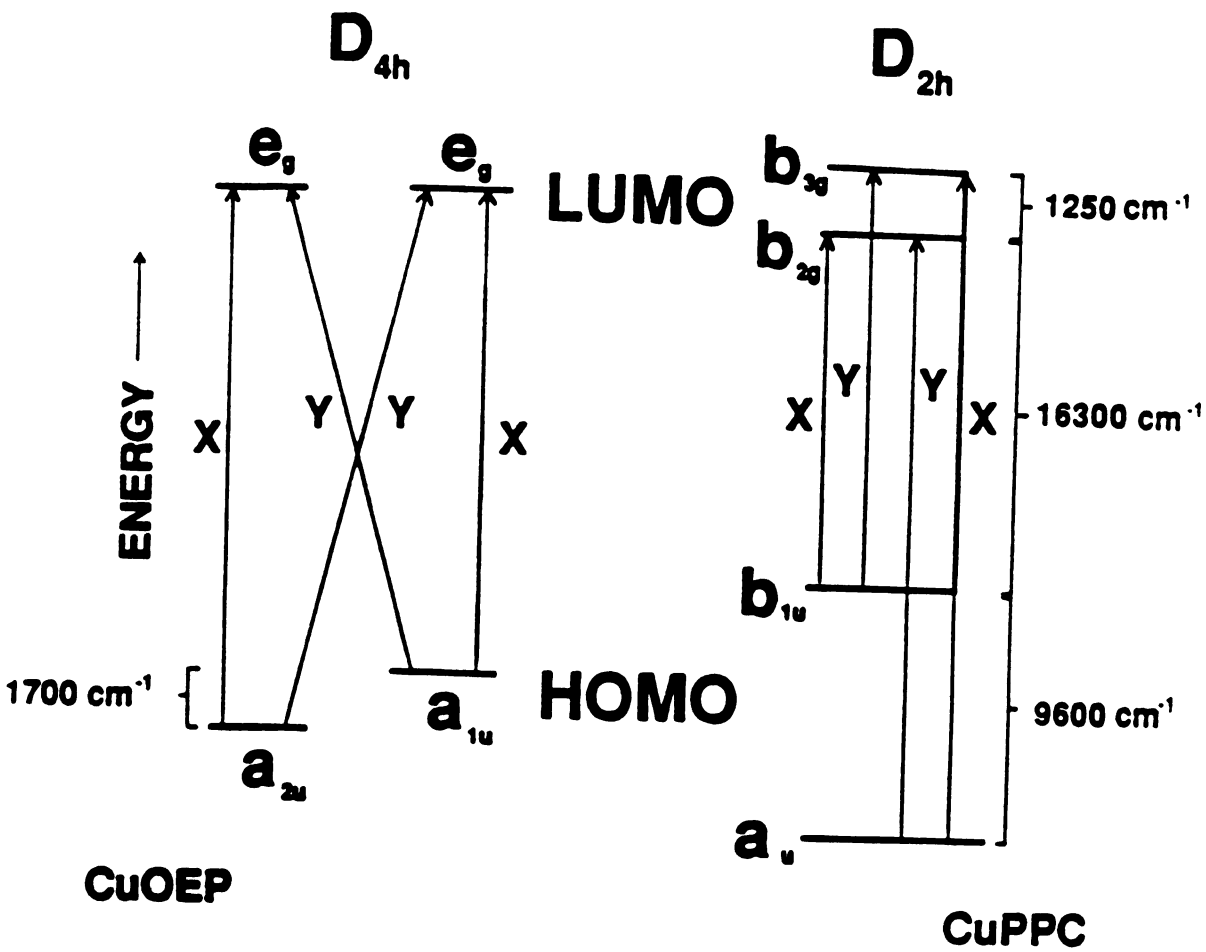
D4h
D2h
eg
eg
LUMO
b3g
b2g
b1u
au
1250 cm-1
16300 cm-1
9600 cm-1
ENERGY
X
Y
Y
X
X
Y
Y
X
1700 cm-1
a1u
HOMO
a2u
CuOEP
CuPPC

and B transition energies. On going from NiOEP to CuOEP there is an expansion of the porphyrin core that results in an increase in the energy of the a_{2u} orbital relative to the a_{1u} and LUMO orbitals[69-70]; thus, a red-shift occurs.

On the other hand, the degeneracy of the LUMOs and the near degeneracy of the HOMOs are lifted for metalloporphycene. For CuPPC it was estimated that a ~1250 cm^{-1} gap occurs between the b_{2g} and b_{3g} orbitals and a splitting of ~9600 cm^{-1} between the a_u and b_{1u} orbitals based on the optical spectrum (Figure 3-1 and Table 3-1) and schematic orbital energy level diagrams (Figure 3-9). This results in four allowed transitions, each involving essentially one-electron excited-state wave functions. Table 3-1 assigns these transitions to the metalloporphycene absorption spectra. According to this model, the effects of substitution are easily understood. Table 3-1 and Figure 3-9 show that the energy gaps between b_{1u} and b_{3g} orbitals for NiPPC and CuPPC are ~17760 cm^{-1} and ~17550 cm^{-1}, respectively, and that the energy gaps between b_{1u} and b_{2g} orbitals for NiPPC and CuPPC are ~16630 cm^{-1} and ~16300 cm^{-1}, respectively. These mean that Ni^{II} substitution for Cu^{II} lowers the relative energy of the b_{1u} orbital by ~300 cm^{-1} and causes a blue-shift of both the $B_{3u}(x)$ and $B_{2u}(y)$ transitions that correspond to the $b_{1u}b_{2g}$ and $b_{1u}b_{3g}$ one-electron excited-state wave functions, respectively. Comparison of CuPPC with Cu-Br_4PPC reveals that tetrabromination at the $C_{b'}$ positions raises the b_{1u} energy

level by ~400 cm^{-1} relative to that of the a_u orbital while causing no change in the energy level of the LUMOs, accounting for the observed red-shifts. Thus, the relative energy level of the b_{1u} orbital (which corresponds to the a_{2u} orbital in D_{4h} the symmetry)[71] increases in the series NiPPC, CuPPC, and Cu-Br_4PPC. This trend most likely originates in the expansion of the macrocycle.

Increased core size on going from NiPPC to CuPPC is analogous to the OEP complexes. Also, tetrabromination increases the macrocycle core size because the bulky C_b, substituents interact sterically.[8] Although metal substitution and bromination of the ring may well change the absolute energies of all orbitals, the relative energies of the a_u or the LUMOs are not influenced by substitution. As a result the near-UV transition energies do not change.[72] Accordingly, in the absence of strong configuration interaction, the MO energy level diagrams can be estimated directly from the absorption spectra. The large splitting (~9600 cm^{-1}) of the HOMO levels cause the absence of configuration interaction (CI) between the near-UV and visible transitions of this symmetry. The gap between the LUMOs is smaller(~1250 cm^{-1}); however, the orthogonality of each of the components of the visible and near-UV transitions also precludes strong CI effects.

Earlier, Platt[19,66] and co-workers pointed out examples of what they termed "long-field" molecules in which CI was minimized. These include pyrene, biphenyl, and

tetrahydroporphine. Although Platt[61] speculated that there is most likely no pure long-field molecule, metalloporphycene may represent the best example of such thus far encountered.

3.3.2) Symmetry and the Resonance Raman Depolarization Ratio

The skeletal structure of metalloporphycene belongs to the D_{2h} point group (Figure 1-2). The x and y symmetry axes are oriented through the bridging positions, not through the pyrrole groups, as in the metalloporphyrin (D_{4h}). For the 37-member structure in which all substituents are considered point masses, 51 Raman-active and 45 IR-active fundamental vibrations should occur. In the resonance Raman spectrum, only in-plane $\pi \rightarrow \pi^*$ electronic transitions of the macrocycle are expected to be observed. Thus the number of in-plane Raman-active fundamentals should be 35 modes (18 a_g and 17 b_{1g}). These modes, a_g and b_{1g}, can be readily distinguished by measurement of the Raman depolarization ratio, ρ. For totally symmetric a_g vibrations, ρ will be between 0 and 3/4. For b_{1g} modes, $\rho \geq 3/4$; that is, the latter modes can assume anomalous polarization if the scattering tensor is a mixture of symmetric and antisymmetric contributions.[25,73] Table 3-2 shows that, although some differences in the relative intensities occur, the ρ values of the major RR bands observed are between 0.2 and 0.5. Thus, only polarized modes may be observed for the

metalloporphycene and the distinctive inverse or anomalous polarization phenomenon present in the RR scattering of the metalloporphyrin[74] is not observed. Based on the depolarization ratios, all of these vibrations are assigned to the totally symmetric representations a_g.

3.3.3) Vibronic Coupling

Although the one-electron $\pi \rightarrow \pi^*$ states of the metalloporphycene do not show strong electronic coupling, i.e., they exhibit weak configuration interaction, vibronic coupling is still conceivable. Under D_{2h} symmetry $B_{2u} \times B_{3u} = b_{1g}$. Thus the b_{1g} modes can couple these electronic transitions via a Herzberg-Teller (HT) mechanism. Electronic transitions of like symmetry can couple via a_g modes; thus, it is possible for totally symmetric modes to exhibit HT activity. Indeed, vibronic activity of a_{1g} modes has been reported for metalloporphyrins.[75-78] The relative oscillator strengths of the visible and near-UV bands apparent from the absorption spectrum in Figure 3-1, however, imply an absence of HT coupling in MPPC compounds. In the case of metalloporphyrins, HT coupling of a formally forbidden transition (the Q band) to an allowed one (the Soret band) results in a smaller ratio of visible to near-UV oscillator strengths.[20-21] But resonance Raman depolarization ratios for metalloporphycene do not exhibit any anomalously polarized modes (Table 3-2). Thus there is no conclusive evidence of HT coupling and the scattering derives primarily from an

Albrecht A-term (Franck-Condon) mechanism. Since no degenerate representations are contained in the D_{2h} point group, Jahn-Teller (JT) coupling is not expected. In view of the above, all of the 18 vibrations listed for CuPPC in Table 3-3 are assigned to the totally symmetric representation, a_g. Owing to the apparent sparseness of vibronic coupling, the spectra of NiPPC and CuPPC are remarkably simple.

This situation in metalloporphycene is in contrast to the case of the metalloporphyrins, where the CI-induced excited states are extensively affected by both JT and HT couplings. As a result, the RR spectra of the MOEP class are exceedingly rich in vibronic information.[25,74-78]

3.3.4) Effects of Selective Deuteration and Metal Substitution on Raman Frequencies

In the region above 1400 cm^{-1} the intense RR bands of Figure 3-7 are clearly isotope sensitive and easily correlated. The 5-11 cm^{-1} shifts upon d_4(py) but not d_4(et) substitution obviously indicate that the 1625 and 1520 cm^{-1} vibrations of NiPPC involve the $C_{b'}$ atom and not the ethylene bridge carbons(C_e). Thus, they are most likely localized on the pyrrole rings and/or across the $C_{a'}C_{a'}$ bond. On the other hand, the features at 1579 and 1410 cm^{-1} shift in both isotopically substituted species. This suggests delocalized motions involving both pyrrole and ethylene bridge carbons. The mode at 1410 cm^{-1} shifts more dramatically upon d_4(et) substitution and is hence assigned

as a large percentage of νC_eC_e and possibly some δC_eH character. The bands in the 1300-1400 cm^{-1} region shift little upon deuteration at the outer ring carbons and are assigned to C-N stretches.

Below 1300 cm^{-1} the Raman features are less intense and the normal modes likely undergo changes in composition upon deuteration. This makes it difficult to correlate features and to ascertain the internal coordinates involved based purely on isotopic shifts. In the d_4(py) derivative, features appear at 1270, 1085, 1016 and 925 cm^{-1} that are not easily associated with vibrations of the natural abundance sample. This is also true for the 1187 cm^{-1} feature in the d_4(et) sample. Some suggestions are presented in Table 3-3 but these must be considered tentative. For example, the 925 cm^{-1} feature in the NiPPC-d_4(py) spectrum is most likely due to a δC_bD motion. In NiOEP, NiTPP, and CuTPP (TPP=tetraphenylporphyrin) the δC_mH and δC_bH motions, respectively, can cause shifts upon deuteration ranging from 30 to 400 cm^{-1}, depending on the potential energy distribution(P.E.D.) of the normal mode.[60-64] Hence, correlating the 925 cm^{-1} feature with the 1167 cm^{-1} band present in both NiPPC and NiPPC-d_4(et) is plausible. The 1410 cm^{-1} vibration of NiPPC can be compared to a mode at 1504 cm^{-1} of both CuPPC and NiTPP that has been assigned by Atamian et al.[63] and Li et al.[64] to a mixture of νC_bC_b and δC_bH motions. The deuterium shifts of 44 and 47 cm^{-1} reported for these porphyrin vibrations[63-64] are similar to the 53 cm^{-1}

which is observed for NiPPC upon deuteration at the ethylene bridge carbons. CuTPP and NiTPP also have a mode around 1375 cm^{-1} displaying approximately a ~40 cm^{-1} deuterium shift. This mode is likely a mixture of the νC_aC_b and C_aN or δC_bH coordinates.[63-64]. By analogy to these assignments, based on the frequency and isotopic shift, the 1410 cm^{-1} feature of NiPPC is assigned to the smaller ~7 cm^{-1} shift on d_4(py) substitution, possibly some $\nu C_{a'}C_{b'}$ or $\nu C_{a'}N$ motion. Finally, the 996 cm^{-1} mode probably involves the pyrrole substituents similar to the 1025 cm^{-1} vibration in NiOEP.[60,62] Incorporation of deuterium at the $C_{b'}$ position most likely causes a change in normal mode composition resulting in a new vibration at 1016 cm^{-1} (and possibly also at 1085 cm^{-1}). This could well result from coupling of the $\delta C_{b'}D$ vibration, which has shifted into the 900 - 1000 cm^{-1} region, with the 996 cm^{-1} mode. The $\delta C_{b'}D$ could then derive some intensity from the 996 cm^{-1} vibration resulting in the features at 925 and 1016 cm^{-1} observed in the spectrum of NiPPC-d_4(py). Similar coupling may also occur for the 944 cm^{-1} vibration, as it cannot be found in the NiPPC-d_4(py) spectrum. This vibration undergoes an isotopic shift upon d_4(et) substitution, whereas the 996 cm^{-1} vibration does not, indicating that they are localized in different areas of the macrocycle.

3.3.5) Structure Sensitive Vibrations

In metalloporphyrins the vibrations in the 1400 - 1700 cm^{-1} range are distinctly dependent on the central metal. This is due to variations in the size of the porphyrin core in response to metal substitution. Spaulding et al.[79] identified the relevant structural parameter to be the center to pyrrole nitrogen distance, d_{CtN}, Huong and Pommier[80] quantified the relationship between vibrational frequency and d_{CtN} , and subsequent work extended the correlation to a large number of vibrations of a variety of metalloporphyrin[27,45,81] complexes. Because the relationship between frequency and core size is dependent on the P.E.D. of the vibration, such analysis has been used to support vibrational assignments in metallochlorins[26,38] and in the π-cation radicals of metalloporphyrins and metallochlorins.[46] Comparison of the crystal structures of Ni^{II} and Mg^{II} porphyrins[82-83] shows that the C_aC_m and C_bC_b bond lengths change by 0.044 and 0.014 Å upon expansion of the porphyrin d_{CtN} from 1.958 to 2.055 Å. The lengthening of these bonds decreases νC_aC_m and νC_bC_b frequencies. Thus, those normal coordinates involving νC_aC_m motion, followed by those involving νC_bC_b motion, show the steepest inverse slopes in the relationship between frequency and core size $\nu = K(A-d_{CtN})$.[80]

Table 3-3 shows that the metal dependence for the vibrational frequencies of PPC is similar to that of the analogous OEP complexes. The vibrations at 1625, 1579, and

1520 cm^{-1} in NiPPC decrease by 35, 20, and 14 cm^{-1}, respectively, in CuPPC. This suggests that these vibrational frequencies are structure sensitive. The structural parameter that determines the vibrational frequencies cannot be identified with certainty until more crystal structures are determined. Correlation of vibrational frequency to metalloporphycene structure will be complicated by the apparent dependence of the core skeletal structure on the peripheral substituents.[8] This is in contrast to the case for metalloporphyrins[84], where the relative invariance of the core size of different porphyrins complexed to the same metal has been exploited extensively in establishing correlations of vibrational frequencies to d_{C_tN}.[79]

Given the above cautions, a preliminary analysis of the available structural and vibrational data suggests that the three highest RR frequencies of the PPC macrocycle are, nevertheless, approximately linearly dependent on the center-to-nitrogen distance. Table 3-4 collects the structural data for PPC compounds and compares them to those of the analogous porphyrins. Measurements of H_2PPC, H_2PPC-d_4(py), and H_2PPC-d_4(et) reveal that the three highest RR frequencies of the free base PPC at 1606, 1559, and 1505 cm^{-1} derive from normal modes with qualitatively similar P.E.D.'s to those of the metalloporphycene complexes. Thus, these points can be used to estimate K and A parameters for a structural correlation of porphycene

vibrational frequency to core size for each of these modes (Table 3-4).

Comparison of these estimated structural parameters to those of porphyrins (Table 3-4 and ref. 27, 79-84 and references therein) suggests interesting generalizations. The porphycene macrocycle is in general smaller, more rigid, and less able to expand than the porphyrin ring. This is reflected by the fairly high K values(inverse slope) estimated for PPC vibrations compared to those of typical high frequency porphyrin modes.[27,46,80-81] Also, the core size of the free base porphycene falls within the range of these metal complexes, whereas the free base porphyrin has a larger core size than the metalloporphyrin complexes considered here. This relatively contracted core size for H_2PPC is the result of exceptionally strong internal hydrogen bonds between the imine pyrrole nitrogen atoms and the free base protons.[3,8]

3.3.6) Iron Complexes

In Figure 3-8 the ClFe^{III}PPC spectrum is more complex than that of (Im)$_2$Fe^{III}PPCCl, suggesting that the $\pi \rightarrow \pi^*$ excited states of the ring (B_{2u} and B_{3u} in D_{2h} symmetry) interact with $\pi \rightarrow d_{yz}$, d_{xz} charge-transfer (CT) excited states (also B_{2u} and B_{3u}). These CT states are likely produced from b_{1u}(porphycene) $\rightarrow$ b_{3g},b_{2g}(iron) transitions analogous to the a_{2u}(porphyrin) $\rightarrow$ e_g(iron) transitions of D_{4h} hemes.[85-86] As the latter do not occur in low-spin Fe^{III}

Table 3-4

(A) Core Sizes of PPC and Analogous Porphyrin Complexes

	d_{CtN}(Å)			
	PPC	ref.	Porphyrin	ref.
Ni	1.896	4	1.958	79, 82
Cu	1.94 ± 0.01	5	2.000	79
H_2	1.927	4	2.065	83

(B) Estimates of Structural Parameters for MPPC and MOEP[38] Vibrational Frequencies

NiPPC vibration (cm^{-1})	K (cm^{-1}/ Å)	A (Å)
1625	760	4.03
1579	490	5.12
1520	350	6.26

NiOEP vibration (cm^{-1})	K (cm^{-1}/ Å)	A (Å)
1655	405	6.05
1602	236	8.74
1576	203	9.73

systems, their presence in the absorption spectrum[67-68] of $ClFe^{III}PPC$ is consistent with a spin state higher than S = 1/2. Analogous ferric porphyrin complexes exhibit spectral trends qualitatively similar to those in Figure 3-8.

By analogy to $ClFe^{III}$ porphyrins, a pure S = 5/2 high spin state is expected for $ClFe^{III}PPC$; however, magnetic susceptibility measurements indicated that substantial S = 3/2 intermediate spin character exists.[87] The smaller core size of porphycene presumably increases the splitting of the $d_{x^2-y^2}$ level from the other iron orbitals making the S = 5/2 state less accessible than in porphyrin complexes.

In iron porphyrins the vibrational frequencies of the macrocycle are known to be sensitive to the ligation, spin, and oxidation state of the Fe. This situation has been extensively exploited by RR study of heme proteins.[53] It is of interest to determine if a similar situation exists for iron porphycenes. The EPR spectrum of the six-coordinate ferric complex confirms an S = 1/2 spin state for the iron atom. The features of $(Im)_2Fe^{III}PPCCl$ at 1298, 1513, 1567, and 1605 cm^{-1} in Figure 3-8 are clearly higher in frequency than the analogous features in the ferric chloride complex. This indicates that the conformation of the porphycene macrocycle is more contracted in the $(Im)_2Fe^{III}$ complex than in the $ClFe^{III}$ adduct.

Figure 3-8 shows that the metal center in porphycene is reduced. The 13 cm^{-1} decrease from 1298 to 1285 cm^{-1} upon reduction is larger than the 7-9 cm^{-1} decrease exhibited by

the vibrations in the 1400-1700 cm^{-1} range. While the latter reflect the macrocycle expansion attributable to the larger ionic radius of Fe^{II} than Fe^{III}, the decrease in frequency of the mode around 1300 cm^{-1} is much larger than expected by comparison to the Ni^{II} and Cu^{II} complexes. Consequently, this feature appears analogous to the $\nu_4 C_aN$ mode of hemes, the "oxidation state marker". The porphycene mode is likely to be a νC_aN or $\nu C_{a'}N$ motion, and these data suggest overlap between the porphycene $b_{3g}(\pi^*)$ and $b_{2g}(\pi^*)$ orbitals and the iron $b_{3g}(d_{yz})$ and $b_{2g}(d_{xz})$ orbitals, analogous to the situation in iron porphyrins.[53,88] Reduction of the metal to Fe^{II} most likely leads to population of the macrocycle π^* orbitals and weakening of the C_aN and/or $C_{a'}N$ bonds.

CHAPTER 4

EFFECTS OF LOWER SYMMETRY AND NORMAL COORDINATE ANALYSES OF METALLOCHLORIN

4.1) Introduction

Hydroporphyrins serve as the prosthetic groups in a variety of proteins that participate in electron transfer and catalysis.[12-14,89-98] The structural and electronic properties of these macrocycles determine the detailed aspects of their functional nature. The vibrational characteristics of the ring are a particularly sensitive indicator of these properties.[99] Accordingly, many groups have been using vibrational spectroscopy to probe hydroporphyrins and related macrocycles.[26,36-40,100-123] At present, a substantial body of vibrational data is available for reduced pyrrole macrocycles. Most of these data have been acquired for metallochlorins. These macrocycles are structurally similar to metalloporphyrins except that one of the four pyrrole rings is reduced (Figure 1-3).

The availability of a considerable amount of vibrational data for metallochlorins makes these rings the most amenable to vibrational analysis. The first interpretations of the vibrational spectra of these systems

were made exclusively by analogy to those of metalloporphyrins.[26,39,98,100-105] This type of analysis presumes that the vibrational eigenvectors of the two different classes of macrocycles are similar. Because there is no *a priori* basis for this assumption, normal coordinate analyses are required to identify the exact forms of the normal modes of the reduced pyrrole systems. In this regard, normal coordinate calculations have been reported for a variety of metallochlorins, including NiOEC[36,109], Cu(II) tetraphenylchlorin[104], and several Ni(II) pheophorbides.[36] Bocian et al.[36,108] have examined all of these species by using semiempirical quantum force field and/or empirical force field (GF matrix) methods. Several other groups[109,123] have also examined MOEC complexes by using empirical force field methods. Bocian et al.'s calculations (both empirical and semiempirical) predict that the forms of the normal modes of metallochlorins are in general different from those of porphyrins.[36,108] In contrast, empirical calculations on NiOEC by Prendergast and Spiro[109] predict that the vibrational eigenvectors of metallochlorins are similar to those of metalloporphyrins.

The origin of the disagreements between the empirical and semiempirical normal coordinate calculations on NiOEC is not clear, although Spiro and co-workers have suggested that they are due to intrinsic inaccuracies in the semiempirical approach.[109] While it is true that semiempirical vibrational analysis methods are less accurate than empirical

approaches, the development of an accurate empirical force field requires data from a variety of isotopomers. However, Spiro et al. did not use the vibrational data from a series of meso-deuterated NiOEC complexes (NiOEC, NiOEC-α,β-d_2, NiOEC-γ,δ-d_2, NiOEC-d_4). They utilized only the vibrational data from NiOEC-γ,δ-d_2 and the pyrrole-^{15}N isotopomer.[109] The inclusion of additional meso-deuteration data (NiOEC-α,β-d_2, NiOEC-d_4) is essential for the development of an accurate force field, because the deuteration in NiOEC-γ,δ-d_2 samples only one of the two symmetry inequivalent methine bridges in the macrocycle (Figure 1-3).

Recently, Fonda et al.[38] obtained detailed IR and resonance Raman data for a series of meso-deuterated CuOEC complexes (CuOEC, CuOEC-α,β-d_2, CuOEC-γ,δ-d_2, and CuOEC-d_4). The deuteration in these isotopomers systematically perturbs each of the symmetry inequivalent methine bridges of the OEC ring. Now it is possible to develop an empirical force field for CuOEC based on the vibrational data from a series of meso-deuterated CuOEC complexes. Furthermore, the detailed IR and resonance Raman data were also obtained from the various meso-deuterated ZnOEC complexes (ZnOEC, ZnOEC-α,β-d_2, ZnOEC-γ,δ-d_2, ZnOEC-d_4). These data allow the examination of the effects of the central metal ion on the forms of the vibrational eigenvectors. Additionally, this new information provides a basis for a comparison of the various force fields for MOEC complexes and the factors that influence the forms of the vibrational eigenvectors.

4.2) Theory of Normal Vibrations[124,125]

4.2.1) Normal Modes

Each normal coordinate is a linear combination of basis coordinates. Prior to the development of the Wilson method, the Cartesian coordinates were used as the basis set. In contrast, the Wilson method uses internal coordinates as the basis set. In fact, only five different types of internal coordinates are needed to represent a given normal coordinate completely.

For a general polyatomic molecule, there are 3N - 6 normal coordinates (3N - 5 for a linear molecule), where N is the number of atoms in the polyatomic molecule. In a diatomic molecule, the internal coordinate (bond stretch) is the normal coordinate. The restoring force for the diatomic molecule will then be:

$$F = -kq \qquad \text{(eq. 4-1)}$$

where q represents the internal coordinate.

The potential energy V will be given by:

$$2V = kq^2 \qquad \text{(eq. 4-2)}$$

The kinetic energy T will be given by:

$$2T = \dot{q}^2 \qquad \text{(eq. 4-3)}$$

where $\dot{q} = dq/dt$. If the normal modes of a general polyatomic molecule are to behave in the same manner as the normal mode of the diatomic molecule, the expressions for the potential and kinetic energies will not have cross terms. That means the normal modes are defined to be mutually orthogonal,

hence the name "normal" modes. In terms of the normal coordinates, Q, the kinetic and potential energy expressions for a general polyatomic molecule can be written as:

$$2T = \sum_i \dot{Q}_i^2 \qquad 2V = \sum_i \lambda_i Q_i^2 \qquad \text{(eq. 4-4)}$$

where $\dot{Q}_i = dQ_i/dt$, and the summations over i run from 1 to 3N - 6 (or 3N - 5 for linear molecules).

The kinetic and potential energies take a diagonal form in their matrix representations. The expressions in eq. 4-4 can be rewritten as:

$$2T = \dot{\underline{Q}}'\dot{\underline{Q}} \qquad 2V = \underline{Q}'\lambda\,\underline{Q} \qquad \text{(eq. 4-5)}$$

where $\underline{Q}$ is the matrix (column vector) of the normal coordinates, $\dot{\underline{Q}}$ is its time derivative and λ is the diagonal matrix of the λ values. $\underline{Q}'$ and $\dot{\underline{Q}}'$ are the transpose matrices of Q and $\dot{\underline{Q}}$, respectively.

4.2.2) Internal Coordinates

There are five kinds of internal coordinates that are used to describe the motion of a molecule. Except for the linear bend, all the internal coordinates' $\vec{s}$ vectors are defined in terms of unit vectors, $\vec{e}_{ij}$, directed along the bonds. The expressions for the $\vec{s}$ vectors also incorporate information on the bond lengths and valence angles. The $\vec{e}_{ij}$ are defined as:

$\vec{e}_{ij} = [(x_j - x_i)\vec{i} + (y_j - y_i)\vec{j} + (z_j - z_i)\vec{k}]/r_{ij}$ where (x_i,y_i,z_i) and (x_j,y_j,z_j) are the Cartesian coordinates of

atoms i and j, respectively, and r_{ij} is the distance between them. The five types of internal coordinates are:

(1) Bond Stretch : Δr_{ij} (Figure 4-1)

(2) Valence Angle Bend : $\Delta\alpha_{ijk}$ (Figure 4-2)

(3) Out-of-Plane Wag : $\Delta\vartheta$ (Figure 4-3)

(4) Linear Valence Angle Bend : $\Delta\phi$ (Figure 4-4)

(5) Torsion : $\Delta\tau$ (Figure 4-5)

Decius proved that this set of basis vectors is sufficient to describe the normal coordinates of any molecule completely.

4.2.3) The Transformation from Cartesian Coordinates to Internal Coordinates

The expressions for the kinetic and potential energies in the Cartesian coordinates can be written as:

$$2T = \dot{\underline{X}}'\underline{M}\,\dot{\underline{X}} \qquad 2V = \underline{X}'\underline{F}^{x}\,\underline{X} \qquad \text{(eq. 4-6)}$$

where $\underline{X}$ is the matrix of the Cartesian coordinates. The kinetic energy, when expressed in terms of Cartesian basis vectors, takes the form of the diagonal matrix $\underline{M}$, formed from the masses of the constituent atoms. This formulation parallels that of normal coordinates where the kinetic energy also takes a diagonal form.

The case for the potential energy, however, will not be as simple. The $\underline{F}^{x}$ matrix of eq. 4-6 will be non-diagonal. Except for the case of a linear molecule, the elements of

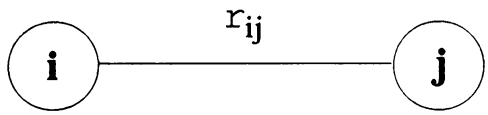

$$\vec{s}_i = - \vec{e}_{ij}$$

$$\vec{s}_j = \vec{e}_{ij}$$

Figure 4-1 Bond Stretch: Δr_{ij}

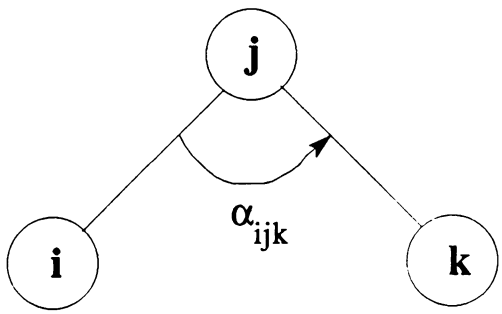

$$\alpha_{ijk} \neq 180°$$

$$\vec{s}_i = (\cos\alpha_{ijk}\, \vec{e}_{ji} - \vec{e}_{jk})/r_{ij} \sin\alpha_{ijk}$$

$$\vec{s}_k = (\cos\alpha_{ijk}\, \vec{e}_{jk} - \vec{e}_{ji})/r_{jk} \sin\alpha_{ijk}$$

$$\vec{s}_j = - (\vec{s}_i + \vec{s}_k)$$

Figure 4-2 Valence Angle Bend: $\Delta\alpha_{ijk}$

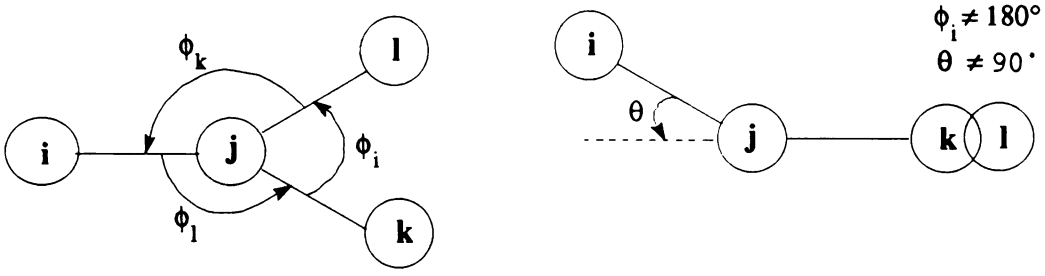

$$\vec{s}_i = \frac{1}{r_{ji}} \left[\frac{\vec{e}_{jk} \times \vec{e}_{jl}}{\cos\vartheta \sin\phi_i} - \tan\vartheta \vec{e}_{ji} \right]$$

$$\vec{s}_k = \frac{1}{r_{jk}} \left[\frac{\vec{e}_{jk} \times \vec{e}_{jl}}{\sin\phi_i} \right] \left[\frac{\cos\phi_i \cos\phi_k - \cos\phi_l}{\cos\vartheta \sin^2\phi_i} \right]$$

$$\vec{s}_l = \frac{1}{r_{jl}} \left[\frac{\vec{e}_{jk} \times \vec{e}_{jl}}{\sin\phi_i} \right] \left[\frac{\cos\phi_i \cos\phi_l - \cos\phi_k}{\cos\vartheta \sin^2\phi_i} \right]$$

$$\vec{s}_j = -(\vec{s}_i + \vec{s}_k + \vec{s}_l)$$

Figure 4-3 Out-Of-Plane Wag: $\Delta\vartheta$

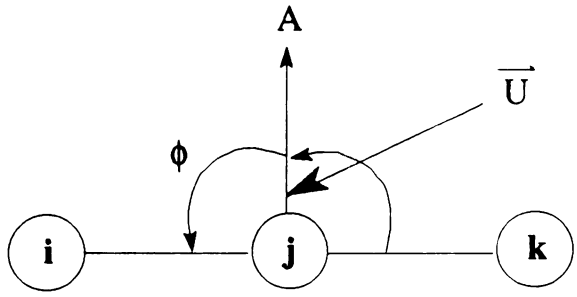

$$\vec{s}_i = -\vec{U}/r_{ji} \qquad \vec{s}_k = -\vec{U}/r_{jk} \qquad \vec{s}_j = -(\vec{s}_i + \vec{s}_k)$$

$\vec{U}$ is a unit vector along j - A, perpendicular to i-j-k.

Figure 4-4 linear Valence Angle Bend: $\Delta\phi$

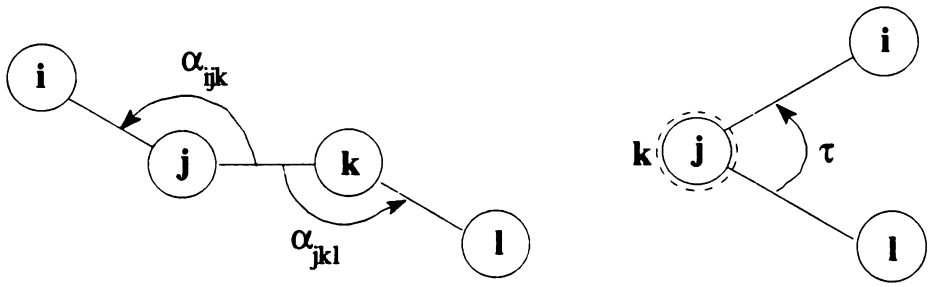

α_{ijk} , $\alpha_{jkl} \neq 180°$

For each i-type atom:

$$\vec{s}_i = \frac{1}{ni} \left[\frac{\vec{e}_{ij} \times \vec{e}_{jk}}{r_{ij} \sin^2 \alpha_{ijk}} \right]$$

For each l-type atom:

$$\vec{s}_l = \frac{1}{nl} \left[\frac{\vec{e}_{lk} \times \vec{e}_{kj}}{r_{lk} \sin^2 \alpha_{jkl}} \right]$$

$$\vec{s}_j = \frac{1}{ni} \sum_{ni} \frac{r_{jk} - r_{ij} \cos\alpha_{ijk}}{r_{ij} r_{jk} \sin^2 \alpha_{ijk}} (\vec{e}_{ij} \times \vec{e}_{jk}) + \frac{1}{nl} \sum_{nl} \frac{\cos\alpha_{jkl}}{r_{jk} \sin^2 \alpha_{jkl}} (\vec{e}_{lk} \times \vec{e}_{kj})$$

$$\vec{s}_k = \frac{1}{nl} \sum_{nl} \frac{r_{jk} - r_{kl} \cos\alpha_{jkl}}{r_{kl} r_{jk} \sin^2 \alpha_{jkl}} (\vec{e}_{lk} \times \vec{e}_{kj}) + \frac{1}{ni} \sum_{ni} \frac{\cos\alpha_{ijk}}{r_{jk} \sin^2 \alpha_{ijk}} (\vec{e}_{ij} \times \vec{e}_{jk})$$

ni = the number of i-type atoms
nl = the number of l-type atoms

Figure 4-5 Torsion: $\Delta\tau$

the $\underline{F}^x$ matrix will be difficult to interpret physically. For a non-linear molecule, combinations of atomic motions along the x, y and z directions will in general be mixtures of stretches and bends. Thus, interpretations of the physical meaning of the elements of the $\underline{F}^x$ matrix, in terms of conventional force constants, will be very difficult. These difficulties can be bypassed if internal coordinates are chosen for the basis set rather than Cartesian displacement vectors. Then, the kinetic and potential energies can be expressed as:

$$2T = \dot{\underline{R}}'\underline{K}\,\dot{\underline{R}} \qquad 2V = \underline{R}'\underline{F}\,\underline{R} \qquad \text{(eq. 4-7)}$$

where $\underline{R}$ is the matrix (column vector) of the internal coordinates and $\underline{K}$ and $\underline{F}$ are the kinetic and potential energies matrices, respectively. Both the $\underline{K}$ and $\underline{F}$ matrices will be non-diagonal. Constructing a non-diagonal kinetic energy matrix is complicated matter. However, the interpretation of the elements of the new $\underline{F}$ matrix in terms of primary and interaction force constants is now relatively easy.

4.2.4) The Kinetic Energy in Internal Coordinates

By definition, the momentum P_{x_i}, conjugate with x_i, is given by:

$$P_{x_i} = \frac{\partial T}{\partial \dot{x}_i} = m_i \dot{x}_i \qquad \text{(eq. 4-8)}$$

The kinetic energy will be given by

$$2T = \underline{P}_x' \; M^{-1} \; \underline{P}_x \qquad \text{(eq. 4-9)}$$

The column vector $\underline{P}_x$ can be expressed as:

$$\underline{P}_x = \underline{M} \; \dot{\underline{X}} \qquad \text{(eq. 4-10)}$$

A set of conjugate momenta, P, can be defined with the internal coordinates, q:

$$P_{q_k} = \frac{\partial T}{\partial \dot{q}_k} \qquad k = 1,2,\cdots\cdots s \qquad \text{(eq. 4-11)}$$

The momentum, P_{x_i}, in terms of Cartesian coordinates, can be written in terms of the coordinates corresponding to the translational and rotational motions of the molecule by q_j° and their conjugate momenta by $P_{q_j^\circ}$

$$\begin{aligned} P_{x_i} &= \frac{\partial T}{\partial \dot{x}_i} \\ &= \Sigma_k^s \frac{\partial T}{\partial \dot{q}_k} \frac{\partial q_k}{\partial x_i} + \Sigma_j^6 \frac{\partial T}{\partial \dot{q}_j^\circ} \frac{\partial q_j^\circ}{\partial x_i} \\ &= \Sigma_k^s \; P_{q_k} \; B_{k,x_i} \end{aligned} \qquad \text{(eq. 4-12)}$$

The second term becomes zero since the momenta corresponding to the translational and rotational motions are zero. In matrix form

$$\underline{P}_x = \underline{B}' \underline{P} \qquad \text{(eq. 4-13)}$$

From eq. 4-10 and eq. 4-13

$$\underline{M} \; \dot{\underline{X}} = \underline{B}' \underline{P} \qquad \text{(eq. 4-14)}$$

The $\underline{B}$ is the transforming matrix defining internal coordinates in terms of Cartesian coordinates:

$$\underline{R} = \underline{B} \; \underline{X} \qquad \text{(eq. 4-15)} \qquad \dot{\underline{R}} = \underline{B} \; \dot{\underline{X}} \qquad \text{(eq. 4-16)}$$

From eq. 4-14, $\dot{\underline{X}} = \underline{M}^{-1}\underline{B}'\underline{P}$. Inserting this into eq. 4-16

$$\dot{\underline{R}} = \underline{B} \; \underline{M}^{-1}\underline{B}'\underline{P} \qquad \text{(eq. 4-17)}$$

So, the new expression for kinetic energy (eq. 4-9) will be given by:

$$2T = \underline{P}'\underline{B}\,\underline{M}^{-1}\underline{B}'\underline{P} \qquad \text{(eq. 4-18)}$$

If a new matrix G is defined as

$$\underline{G} = \underline{B}\,\underline{M}^{-1}\underline{B}' \qquad \text{(eq. 4-20)}$$

Then eq. 4-20 becomes

$$2T = \underline{P}'\underline{G}\,\underline{P} \qquad \text{(eq. 4-21)}$$

Combining eq. 4-21 with eq. 4-17

$$\dot{\underline{R}} = \underline{G}\,\underline{P} \qquad \text{or} \qquad \underline{P} = \underline{G}^{-1}\dot{\underline{R}} \qquad \text{(eq. 4-22)}$$

The kinetic energy can then be rewritten again as:

$$\begin{aligned} 2T &= \underline{P}'\underline{G}\,\underline{P} \\ &= (\underline{G}^{-1}\dot{\underline{R}})'\underline{G}(\underline{G}^{-1}\dot{\underline{R}}) \\ &= \dot{\underline{R}}'\underline{G}^{-1}\dot{\underline{R}} \end{aligned} \qquad \text{(eq. 4-23)}$$

Comparing eq. 4-23 with eq. 4-7, it is clear that

$$\underline{K} = \underline{G}^{-1}$$

Actually, once the B matrix is known, the G matrix follows automatically via the relationship given in eq. 4-20.

4.2.5) The Potential Energy in Internal Coordinates

The potential energy was already defined in eq. 4-7. The elements of the F matrix will be defined as:

$$F_{ij} = \left[\frac{\partial^2 V}{\partial q_i \partial q_j}\right]_e = \left[\frac{\partial^2 V}{\partial q_j \partial q_i}\right]_e \qquad \text{(eq. 4-24)}$$

The subscript "e" indicates that the partial derivative is to be evaluated at the equilibrium geometry. The

interpretation of the elements of the F matrix is now very simple.

4.2.6) The Secular Equation

The matrix $\underline{L}$ is the transformation matrix, which relates the internal coordinates to the normal coordinates as:

$$\underline{R} = \underline{L}\,\underline{Q} \qquad \text{(eq. 4-25)}$$

The potential energy can then be written as:

$$2V = \underline{R}'\underline{F}\,\underline{R} = (\underline{L}\underline{Q})'\underline{F}(\underline{L}\underline{Q})$$

$$= \underline{Q}'\underline{L}'\underline{F}\,\underline{L}\,\underline{Q} \qquad \text{(eq. 4-26)}$$

Comparison of eq. 4-26 with eq. 4-5 yields the important identity:

$$\underline{L}'\underline{F}\,\underline{L} = \underline{\lambda} \qquad \text{(eq. 4-27)}$$

The kinetic energy can now be written as:

$$2T = \dot{\underline{R}}'\underline{G}^{-1}\dot{\underline{R}} = (\underline{L}\dot{\underline{Q}})'\underline{G}^{-1}(\underline{L}\dot{\underline{Q}})$$

$$= \dot{\underline{Q}}'\underline{L}'\underline{G}^{-1}\underline{L}\dot{\underline{Q}} \qquad \text{(eq. 4-28)}$$

Comparison of eq. 4-28 with eq. 4-5 yields the second identity:

$$\underline{L}'\underline{G}^{-1}\underline{L} = \underline{I} \qquad \text{(eq. 4-29)}$$

where $\underline{I}$ is the identity or unit matrix. Therefore,

$$\underline{L}'\underline{F}\,\underline{L} = \underline{I}\,\underline{\lambda}$$

$$= \underline{L}'\underline{G}^{-1}\underline{L}\,\underline{\lambda} \qquad \text{(eq. 4-30)}$$

Left-multiplying by $(\underline{L}')^{-1}$,

$$\underline{F}\,\underline{L} = \underline{G}^{-1}\underline{L}\,\underline{\lambda} \qquad \text{(eq. 4-31)}$$

Left-multiplying by $\underline{G}$,

$$\underline{G}\,\underline{F}\,\underline{L} = \underline{L}\,\underline{\lambda} \qquad \text{(eq. 4-32)}$$

This is the Secular Equation to be solved for the vibrational analyses. The vibrational Hamiltonian matrices are the G and F matrices and the solutions of the Secular Equation (λ values) are related to the vibrational frequencies.

4.2.7) The Potential Energy Distribution

Morino et al.[126] proposed that the potential energy distribution of a normal coordinate, Q_N, be defined by:

$$V(Q_N) = \frac{1}{2} Q_N^2 \sum_{ij} F_{ij} L_{iN} L_{jN} \qquad \text{(eq. 4-33)}$$

In general, the value of $F_{ij}L_{iN}L_{jN}$ is large when i = j. Thus, the $F_{ii}L_{iN}^2$ terms are the most important in determining the distribution of the potential energy and the magnitudes of the $F_{ii}L_{iN}^2$ terms provide a measure of the relative contribution of each internal coordinate, q_i, to the normal coordinate Q_N. Therefore the potential energy distribution is defined by the following expression.

$$PED_{ij} = (F_{ii}L_{ij}^2) / (\Sigma_i F_{ii} L_{ij}^2) \qquad \text{(eq. 4-34)}$$

4.3) Normal Coordinate Calculations

Normal coordinate calculations for CuOEC were performed by using the empirical GF matrix method of Wilson.[124]

The G matrix was constructed by using the crystallographic data for FeOEC.[17] This structure was also used by Prendergast and Spiro[109] in their normal coordinate calculations on NiOEC. The crystallographically determined

structure of the FeOEC ring skeleton is non-planar and deviates somewhat from C_2 symmetry. In this calculation, the geometry was adjusted to give a planar, C_2 structure. The ethyl groups were treated with the ethylene carbons and hydrogens and the terminal methyl groups positioned above and below the plane of the macrocycle such that C_2 symmetry was preserved. The bond lengths and bond angles of the ring skeleton in this idealized structure are given in Table 4-1. Figure 4-6 gives the pyrrole ring designations and atom numbering scheme that were used in the calculations. Figures 4-7 and 4-8 display the internal coordinate numbering scheme for CuOEC. Table 4-2 shows the C_2 symmetry coordinates that were used in the normal coordinate calculations.

The normal modes of CuOEC were calculated with an all-valence force field by using the vibrational analysis programs of Schachtschneider.[127] The normal coordinate calculations for CuOEC were initiated by constructing the F matrix reported for NiOEC by Spiro et al.[109] This force field for NiOEC was developed via a selective refinement of the valence force field previously developed for NiOEP.[128] The magnitude of the diagonal C_aC_m force constants used by Spiro et al.[109] follows a pattern that corresponds to a long-short-long-short alteration of the C_aC_m bond lengths (starting from the reduced ring) rather than the actual short-long-short-long pattern.[17,129,130] The initial calculations on CuOEC utilized the F matrix constructed for NiOEC with the C_aC_m force constants ordered consistent with the bond lengths. As

Table 4-1 Geometric Parameters for the CuOEC Calculation

Inter. Coor.	I	II_i, IV_i	II_j, IV_j	III
		Bond Lengths(Å)		
CuN	1.979	1.973	1.973	1.956
Na	1.327	1.370	1.389	1.379
ab	1.502	1.437	1.446	1.433
am	1.363	1.401	1.363	1.401
bb	1.433	1.351	1.351	1.346
mH		1.100		
b1	1.488	1.505	1.501	1.506
12	1.502	1.529	1.529	1.529
		Angles(degree)		
NCuN	90	90	90	90
CuNa	131.2	127.6	127.4	127.6
Nab	119.5	110.6	110.6	110.6
aNa	100.5	105.0	105.0	104.7
Nam	122.9	124.4	124.4	124.4
abb	100.9	107.7	106.0	107.0
bam	117.6	125.0	125.0	125.0
ama	125.4	125.4	125.4	125.4
ab1	112.9	124.6	125.1	124.8
bb1	130.2	127.6	128.8	128.2
b12	117.5	128.3	128.3	128.3

Labels: a,b and m are the C_a, C_b and C_m atoms; 1 and 2 refer to the first and second C atoms of the ethyl groups.

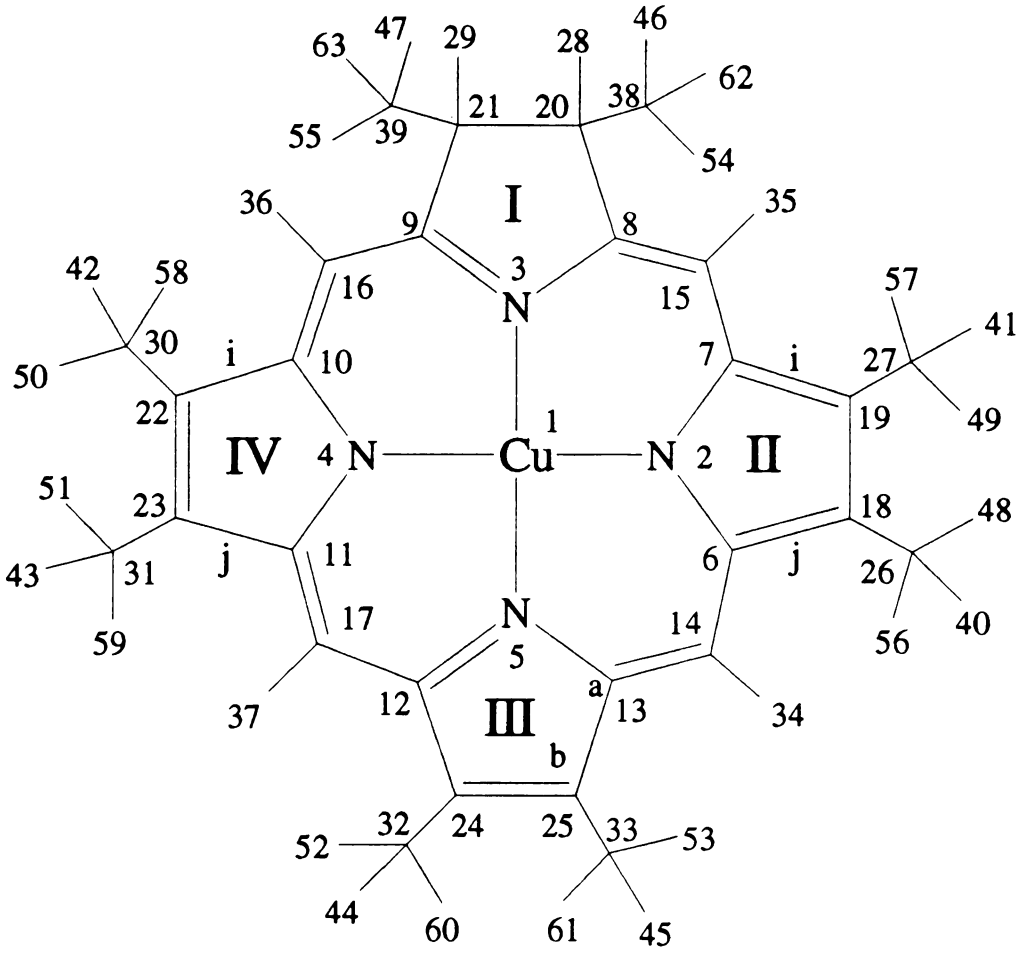

Figure 4-6 Structure and atom labeling scheme for CuOEC

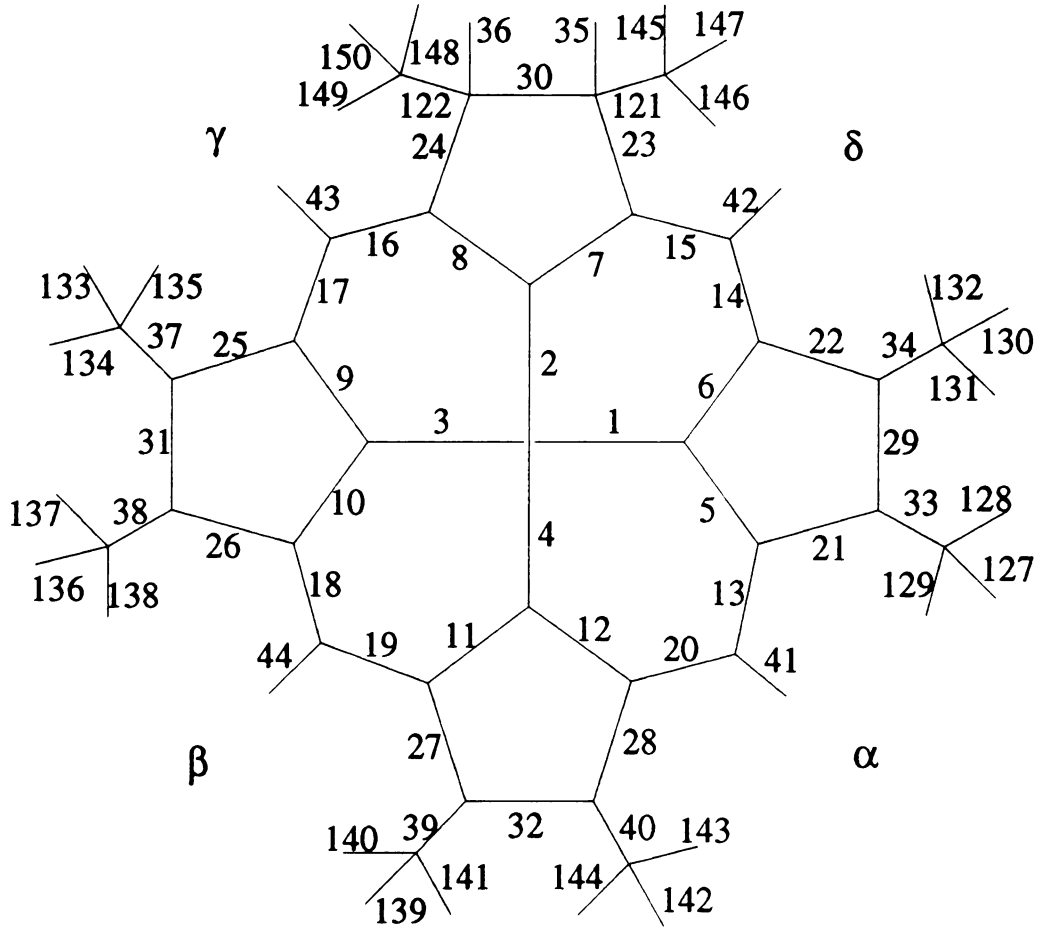

Figure 4-7 Internal coordinates representation of the in-plane metallochlorin bond stretching deformations. The numbers on the bonds refer to the numbers used in the computer program of Schachtschneider.

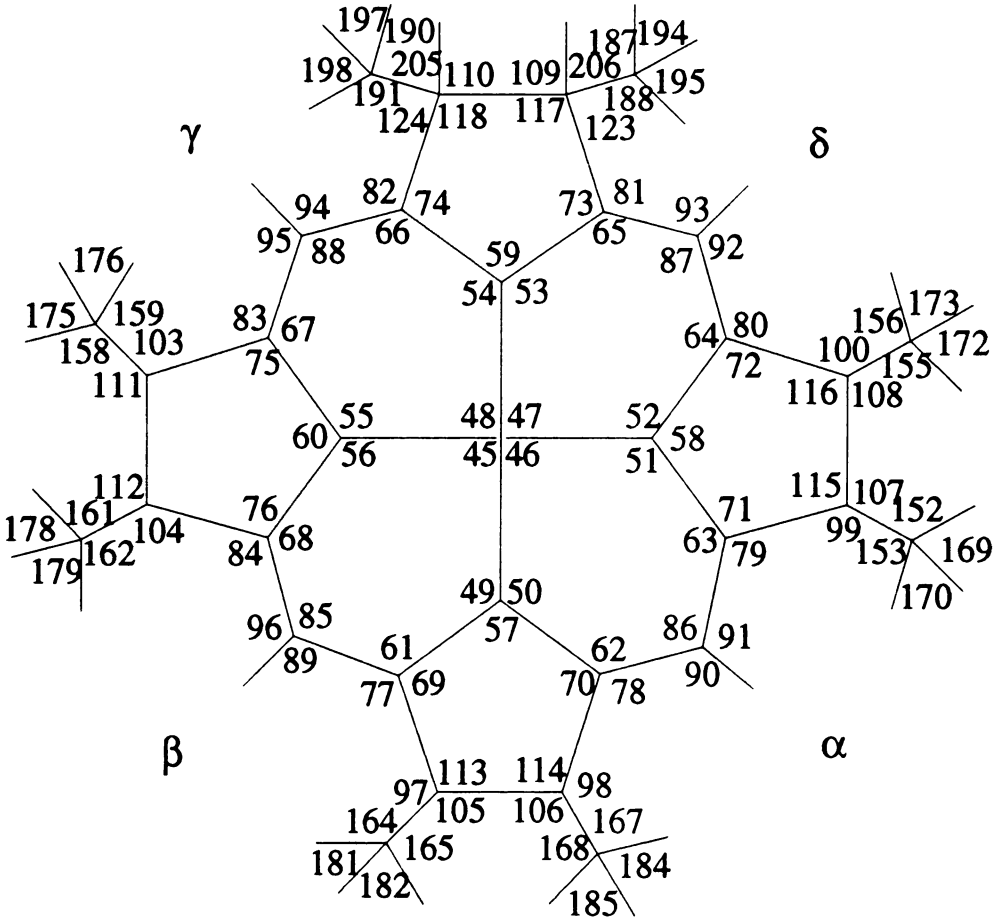

101 = 8-20-28
102 = 9-21-29
125 =38-20-21
126 =39-21-20
151 =40-26-18
154 =41-27-19
157 =42-30-22
160 =43-26-18
163 =44-32-24
166 =45-32-24
171 =56-26-48
174 =57-27-49
177 =50-30-58
180 =59-31-51
183 =60-32-52
186 =61-33-53
189 =20-38-62
192 =21-39-63
193 =46-38-54
196 =47-39-55
199 =26-18-6-19
200=27-19-7-18
201=30-22-10-23
202=31-23-11-22
203=32-24-12-25
204=33-23-13-24

Figure 4-8 Internal coordinates representation of the metallochlorin angle bending deformations.The numbers on the bonds refer to the numbers used in the computer program of Schachtschneider. Some of internal coordinates could not represent in plane. In number series, left hand side numbers could be represented internal coordinates and right hand side number series represent atom labeling in Figure 4-6.

Table 4-2 In-Plane C_2 Symmetry Coordinates for CuOEC

A

1: 1 + 3	2: 2
3: 4	4: 5 + 10
5: 6 + 9	6: 7 + 8
7: 11 + 12	8: 13 + 18
9: 14 + 17	10: 15 + 16
11: 19 + 20	12: 21 + 26
13: 22 + 25	14: 23 + 24
15: 27 + 28	16: 29 + 31
17: 30	18: 32
19: 33 + 38	20: 34 + 37
21: 39 + 40	22: 41 + 44
23: 42 + 43	24: 45 + 46
25: 47 + 48	26: 49 + 50 - 2(57)

27: 51 + 52 - 2(58) + 55 + 56 - 2(60)
28: 53 + 54 - 2(59)
29: 61 + 69 - 2(77) + 62 + 70 - 2(78)
30: 63 + 71 - 2(79) + 68 + 76 - 2(84)
31: 64 + 72 - 2(80) + 67 + 75 - 2(83)
32: 65 + 73 - 2(81) + 66 + 74 - 2(82)
33: 90 + 91 - 2(86) + 89 + 96 - 2(85)
34: 92 + 93 - 2(87) + 94 + 95 - 2(88)
35: 97 + 105 - 2(113) + 98 + 106 - 2(114)
36: 99 + 107 - 2(115) + 104 + 112 - 2(120)
37: 100 + 108 - 2(116) + 103 + 111 - 2(119)
38: 61 - 69 + 62 - 70
39: 63 - 71 + 68 - 76
40: 64 - 72 + 67 - 75
41: 65 - 73 + 66 - 74
42: 97 -105 + 98 - 106
43: 99 - 107 + 104 - 112
44: 100 -108 + 103 - 111
45: 89 - 96 + 90 - 91
46: 92 - 93 - 94 + 95

Table 4-2 (cont.) In-Plane C_2 Symmetry Coordinates for CuOEC

A (cont.)

47: 35 + 36
48: 121 + 122
49: 101 - 109 + 102 - 110
50: 124 - 126 - 125 + 123

51: 117 + 118	52: 127 + 136
53: 128 + 137	54: 129 + 138
55: 130 + 133	56: 131 + 134
57: 132 + 135	58: 139 + 142
59: 140 + 143	60: 141 + 144
61: 145 + 148	62: 146 + 149
63: 147 + 150	64: 151 + 160
65: 152 + 161	66: 153 + 162
67: 154 + 157	68: 155 + 158
69: 156 + 159	70: 163 + 166
71: 164 + 167	72: 165 + 168
73: 169 + 178	74: 170 + 179
75: 171 + 180	76: 172 + 175
77: 173 + 176	78: 174 + 177
79: 181 + 184	80: 182 + 185
81: 183 + 186	82: 187 + 190
83: 188 + 191	84: 189 + 192
85: 193 + 196	86: 194 + 197
87: 195 + 198	88: 199 + 202
89: 200 + 201	90: 203 + 204
91: 51 - 52 + 56 - 55	92: 205 + 206

B

93: 5 - 10	94: 6 - 9
95: 7 - 8	96: 11 - 12
97: 13 - 18	98: 14 - 17

Table 4-2 (cont.) In-Plane C_2 Symmetry Coordinates for CuOEC

B (cont.)

99: 15 - 16	100: 19 - 20
101: 21 - 26	102: 22 - 25
103: 23 - 24	104: 27 - 28
105: 33 - 38	106: 34 - 37
107: 39 - 40	108: 49 - 50
109: 51 - 52 + 55 - 56	110: 54 - 53
111: 89 - 96 + 91 - 90	112: 92 - 93 + 94 - 95

113: 97 + 105 - 2(113) - 98 - 106 + 2(114)

114: 99 + 107 - 2(115) - 104 -112 + 2(120)

115: 100 + 108 - 2(116) - 103 -111 + 2(119)

116: 97 - 105 + 106 - 98

117: 99 - 107 + 112 - 104

118: 100 - 108 + 111 - 103

119: 41 - 44	120: 42 - 43
121: 45 - 46	122: 48 - 47

123: 61 + 69 - 2(77) - 62 - 70 + 2(78)

124: 63 + 71 - 2(79) - 68 - 76 + 2(84)

125: 65 + 72 - 2(80) - 67 - 75 + 2(83)

126: 65 + 73 - 2(81) - 66 - 74 + 2(82)

127: 61 - 69 + 70 - 62

128: 63 - 71 + 76 - 68

129: 64 - 72 + 75 - 67

130: 65 - 73 - 66 + 74

131: 1 - 3	132: 29 - 31

133: 51 + 52 - 2(58) - 55 - 56 + 2(60)

134: 35 - 36

135: 121 - 122

136: 101 - 109 - 102 + 110

137: 124 - 126 + 125 - 123

138: 117 - 118

139: 127 - 136	140: 128 - 137

Table 4-2 (cont.) In-Plane C_2 Symmetry Coordinates for CuOEC

B (cont.)

141: 129 - 138	142: 130 - 133
143: 131 - 134	144: 132 - 135
145: 139 - 142	146: 140 - 143
147: 141 - 144	148: 145 - 148
149: 146 - 149	150: 147 - 150
151: 151 - 160	152: 152 - 161
153: 153 - 162	154: 154 - 157
155: 155 - 158	156: 156 - 159
157: 163 - 166	158: 164 - 167
159: 165 - 168	160: 169 - 178
161: 170 - 179	162: 171 - 180
163: 172 - 175	164: 173 - 176
165: 174 - 177	166: 181 - 184
167: 182 - 185	168: 183 - 186
169: 187 - 190	170: 188 - 191
171: 189 - 192	172: 194 - 197
173: 193 - 196	174: 195 - 198
175: 199 - 202	176: 200 - 201
177: 203 - 204	
178: 90 + 91 - 2(86) - 89 - 96 + 2(85)	
179: 92 + 93 - 2(87) - 94 - 95 + 2(88)	
180: 205 - 206	

expected, this force field overestimates the vibrational frequencies for the skeletal modes of CuOEC (the skeletal mode frequencies of NiOEC are in general higher than those of CuOEC.[36,38,109]). Consequently, the magnitude of all the diagonal stretching force constants were systematically reduced before attempting any perturbative refinement of the force field. This procedure brought the calculated skeletal frequencies of CuOEC into better accord with those observed experimentally. This force field is designated FF I in Table 4-3. Only those force constants that are different from those reported by Spiro et al.[109] are listed in the Table 4-3. Tables 4-4 and 4-5 show force constants that are the same as those reported by Spiro et al.[109] For reference, the force field obtained by reversing the C_aC_m stretching force constants of FF I is also listed in the Table 4-3 and is designated FF II. For this force field and all others described below, only those force constants that are different from those of FFI are included in Table 4-3.

During the course of the vibrational analyses, many strategies were employed in attempts to improve the fit between the observed and calculated vibrational frequencies and isotope shifts. These approaches were based on systematically varying selected diagonal and off-diagonal force constants of the ring skeleton. In all cases the force constants for the reduced ring, the ethyl groups and the meso-hydrogens were held fixed. Two additional force fields that give reasonable fits to the data are also given in

Table 4-3 Refined Diagonal Force Constants[a] for CuOEC

	internal coord.	I	II_1, IV_1	II_2, IV_2	III
FFI[b]	$\kappa(aN)_1$	5.459	5.411	5.127	5.325
	$\kappa(ab)_2$	4.018	5.335	5.431	5.527
	$\kappa(bb)_3$	3.752	6.703	6.703	6.703
	$\kappa(am)_4$	6.819	6.390	6.819	6.390
	$\kappa(CuN)_5$	1.443	1.571	1.571	1.499
FFII[c]	κ(am)	6.390	6.819	6.390	6.819
FFIII[c]	κ(aN)	5.743	7.168	5.888	6.151
	κ(ab)	4.018	5.555	5.368	5.373
	κ(bb)	3.752	6.660	6.660	6.961
	κ(am)	5.138	6.964	6.776	6.470
	κ(CuN)	1.503	1.636	1.636	1.561
1,2	κ-κ(am-am)	0.2		0.4	
FFIV[c]					
1,2	κ-κ(am-am)	0.435		0.412	
1,4	κ-κ(am-am)	-0.362	-0.749		0.129

[a]In mdyn/Å for stretches (κ) and stretch-stretch interaction ($\kappa-\kappa$).

[b]Force field I is numbered for using in Table 4-5.

[c]All other force constants are the same as in force field I

Table 4-4[a] Fixed Diagonal Force Constants[b] for CuOEC

internal coord.	I	II_1, IV_1	II_2, IV_2	III
$\kappa(mH)_6$	4.560	4.560	4.560	4.560
$\kappa(b1)_7$	3.688	4.064	4.064	4.064
$\kappa(12)_8$	4.600	4.600	4.600	4.600
$\kappa(1H)_9$	4.560	4.560	4.560	4.560
$\kappa(bH)_{10}$	4.560			
$H(aNa)_{11}$	1.620	1.620	1.620	1.620
$H(Nab)_{12}$	1.370	1.370	1.370	1.370
$H(abb)_{13}$	1.170	1.370	1.370	1.370
$H(CuNa)_{14}$	0.300	0.300	0.300	0.300
$H(Nam)_{15}$	0.830	0.830	0.830	0.830
$H(mab)_{16}$	0.730	0.830	0.830	0.830
$H(ama)_{17}$	1.100	1.100	1.100	1.100
$H(ab1)_{18}$	0.900	1.200	1.200	1.200
$H(bb1)_{19}$	0.900	1.200	1.200	1.200
$H(b12)_{20}$	1.200	1.200	1.200	1.200
$H(NCuN)_{21}$	0.250	0.250	0.250	0.250
$H(amH)_{22}$	0.500	0.500	0.500	0.500
$H(b1H)_{23}$	0.625	0.625	0.625	0.625
$H(21H)_{24}$	0.625	0.625	0.625	0.625
$H(H1H)_{25}$	0.520	0.520	0.520	0.520
$H(abH)_{26}$	0.400			
$H(bbH)_{27}$	0.400			
$H(1bH)_{28}$	0.400			
$\gamma(b1)_{29}$		0.400	0.400	0.400

[a]ref. 109

[b]In mdyn/Å for stretches (k), mdyn Å/rad^2 for in-plane bends (H) and mdyn Å/rad^2 for out-of-plane bends (γ).

Table 4-5

[a]ref. 109

[b]In mdyn/Å for (κ-κ), (κ-H) and mdyn Å /rad^2 for (κ-H).

[c]i-j, interaction between internal coordinates i and j, labeled according to the numbering scheme in Tables 4-3 and 4-4.

$(\kappa\text{-}\kappa)_{1,2}$: stretch-stretch interaction between two bonds sharing one atom

$(\kappa\text{-}\kappa)_{1,3}$: stretch-stretch interaction between two bonds separated by one atom.

$(\kappa\text{-H})_2$: stretch-bend interaction between bond and angle sharing two common atoms.

$(\kappa\text{-H})_1$: stretch-bend interaction between bond and angle sharing one common atom.

$(\text{H-H})_2$: bend-bend interaction between angles sharing two common atoms

Table 4-5[a] Fixed Off Diagonal Force Constants[b] for CuOEC

internal coord.[c]	I	II, III, IV
$(\kappa-\kappa)_{1,2}$		
1-1, 1-4, 1-5, 2-3, 2-7, 4-4, 4-7, 7-8	0.430	0.430
2-4	0.040	0.430
5-5	0.150	0.150
$(\kappa-\kappa)_{1,3}$		
1-2, 2-2	0.250	0.250
1-4, 4-5, 2-4, 2-7 1-7	-0.250	-0.250
$(\kappa-H)_2$		
4-17, 1-11, 2-12 2-16, 4-16, 2-18	0.245	0.245
2-13	0.160	0.160
3-13	0.020	0.320
3-19, 7-18, 6-19	0.320	0.320
1-12. 1-15, 1-14	0.100	0.100
4-22	0.080	0.150
5-23, 8-24	0.110	0.110
$(\kappa-H)_1$		
1-15, 1-12, 2-11, 7-12	-0.120	-0.120
1-12, 2-15, 4-12, 2-19, 1-22	-0.245	-0.245
$(H-H)_2$		
15-17	0.060	0.060
23-24	-0.070	-0.070

Table 4-3. One of the force fields was obtained by first refining all of the diagonal skeletal constants. This refinement was followed by a second iteration in which only the diagonal force constants of the C_aC_m and C_bC_b bonds were allowed to vary. Finally, the 1,2 C_aC_m-C_aC_m interaction constants for the α,β- and γ,δ-methine bridges were given different values because this improved the fit in the observed versus calculated meso-deuteration shifts. This force field is designated FF III in Table 4-3. The force field designated FF IV was obtained by adding 1,4 C_aC_m-C_aC_m interaction constants to FFI and then refining both these and 1,2 C_aC_m-C_aC_m interaction constants.

4.4) Results

4.4.1) Vibrational Spectra of CuOEC and ZnOEC

Figure 4-9 shows resonance Raman spectra obtained with Soret excitation for ZnOEC, ZnOEC-α,β-d_2, ZnOEC-γ,δ-d_2 and ZnOEC-d_4 in CH_2Cl_2 solutions. The IR spectra for this set of ZnOEC derivatives in $CHCl_3$ solution are shown in Figure 4-10. The total number of bands observed by IR spectroscopy in these measurements is greater than the number detected by resonance Raman spectroscopy owing to the IR activity of the internal vibrations of the ethyl groups. Soret excitation Raman spectra of CuOEC, CuOEC-α,β-d_2, CuOEC-γ,δ-d_2, and CuOEC-d_4, which complement the visible excitation Raman spectra (Figure 4-11) in earlier work[38,131], are shown in Figure 4-12. Comparison of the vibrational data for ZnOEC

Figure 4-9 Resonance Raman spectra of ZnOEC, ZnOEC-α,β-d_2, ZnOEC-γ,δ-d_2 and ZnOEC-d_4 in CH_2Cl_2 solution obtained with Soret excitation at 406.7 nm. Laser power: 7 mW, concentrations: ~40 μM. Asterisks(*) in Figures 4-10, 11, 12, 13 and 14 represent solvent vibrations.

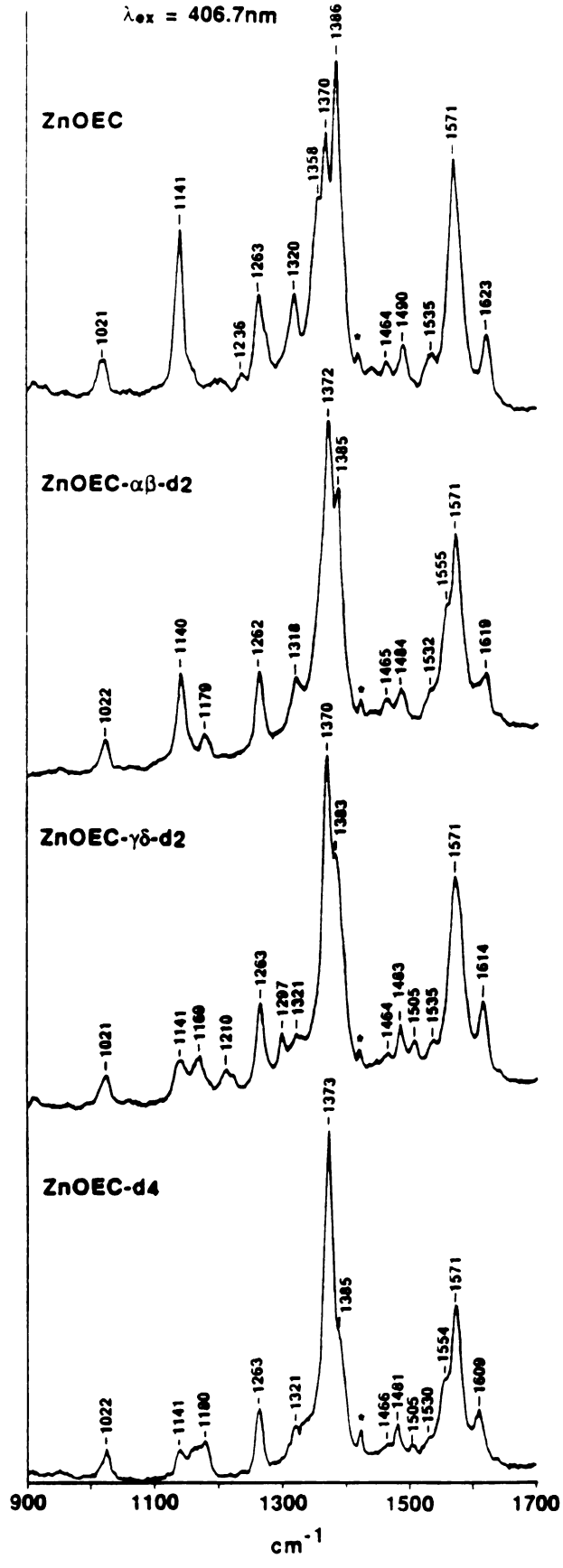
λex = 406.7nm
ZnOEC
1021
1141
1236
1263
1320
1358
1370
1386
1464
1490
1535
1571
1623
ZnOEC-αβ-d2
1022
1140
1179
1262
1318
1372
1385
1465
1484
1532
1555
1571
1618
ZnOEC-γδ-d2
1021
1141
1160
1210
1263
1297
1321
1370
1383
1464
1483
1505
1535
1571
1614
ZnOEC-d4
1022
1141
1180
1263
1321
1373
1385
1466
1481
1505
1530
1554
1571
1600
900
1100
1300
1500
1700
cm-1

Figure 4-10 IR spectra of saturated $CHCl_3$ solution of ZnOEC, ZnOEC-α,β-d_2, ZnOEC-γ,δ-d_2 and ZnOEC-d_4

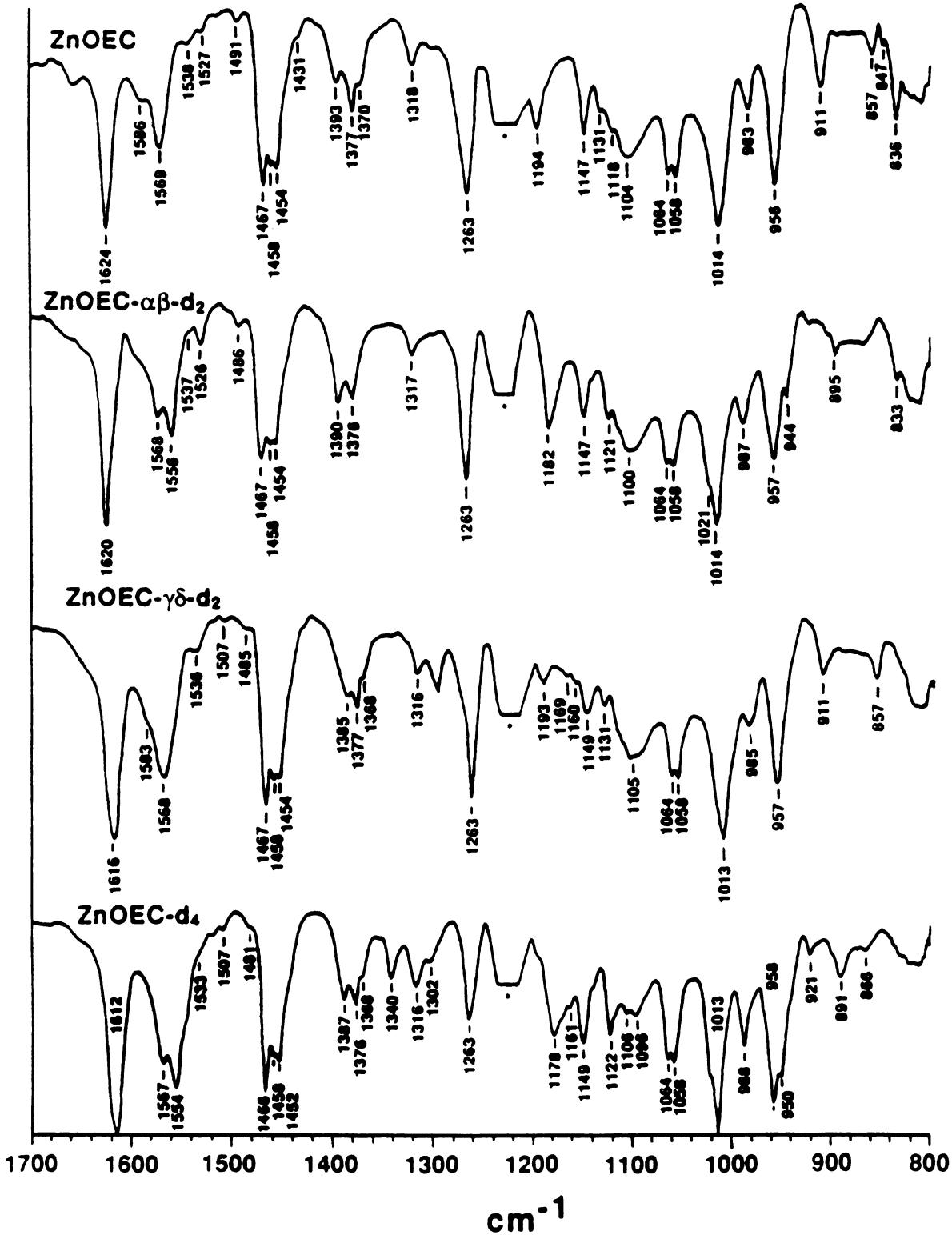
ZnOEC
1624
1586
1569
1538
1527
1491
1467
1458
1454
1431
1393
1377
1370
1318
1263
1194
1147
1131
1118
1104
1064
1058
1014
983
958
911
857
847
836
ZnOEC-αβ-d2
1620
1568
1556
1537
1526
1486
1467
1458
1454
1390
1378
1317
1263
1182
1147
1121
1100
1064
1058
1021
1014
987
957
944
895
833
ZnOEC-γδ-d2
1616
1583
1568
1536
1507
1485
1467
1459
1454
1385
1377
1368
1316
1263
1193
1169
1160
1149
1131
1105
1064
1058
1013
985
957
911
857
ZnOEC-d4
1612
1567
1554
1533
1507
1481
1466
1458
1452
1387
1376
1368
1340
1316
1302
1263
1178
1161
1149
1122
1106
1088
1064
1058
1013
988
958
950
921
891
866
1700
1600
1500
1400
1300
1200
1100
1000
900
800
cm-1

Figure 4-11 Resonance Raman spectra of CuOEC, CuOEC-α,β-d_2, CuOEC-γ,δ-d_2 and CuOEC-d_4 in CH_2Cl_2 solution obtained with visible excitation at 615.0 nm. Laser power: 40 mW, concentrations: ~70 μM (from ref.38).

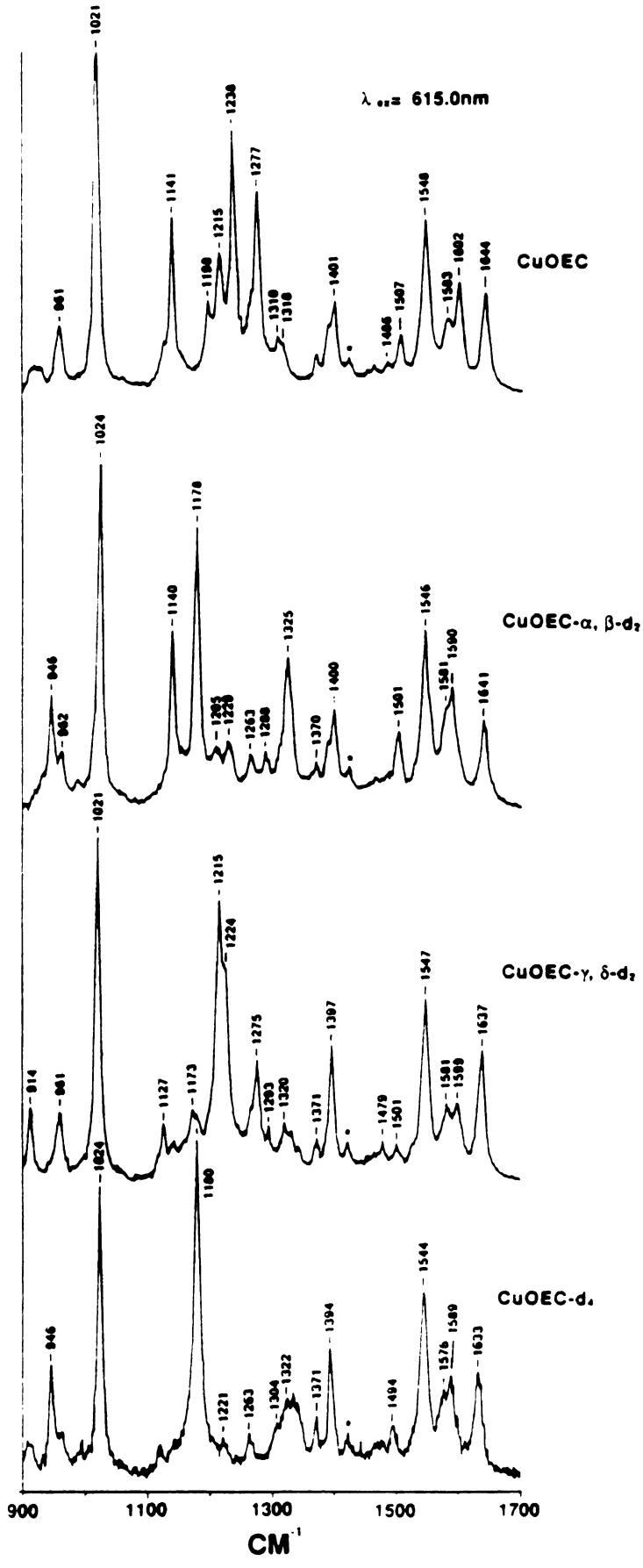
λ exc= 615.0nm
CuOEC
CuOEC-α, β-d2
CuOEC-γ, δ-d2
CuOEC-d4
900
1100
1300
1500
1700
CM-1

Figure 4-12 Resonance Raman spectra of CuOEC, CuOEC-α,β-d_2, CuOEC-γ,δ-d_2 and CuOEC-d_4 in CH_2Cl_2 solution obtained with Soret excitation at 406.7 nm. Laser power: 7 mW, concentrations: ~40 μM.

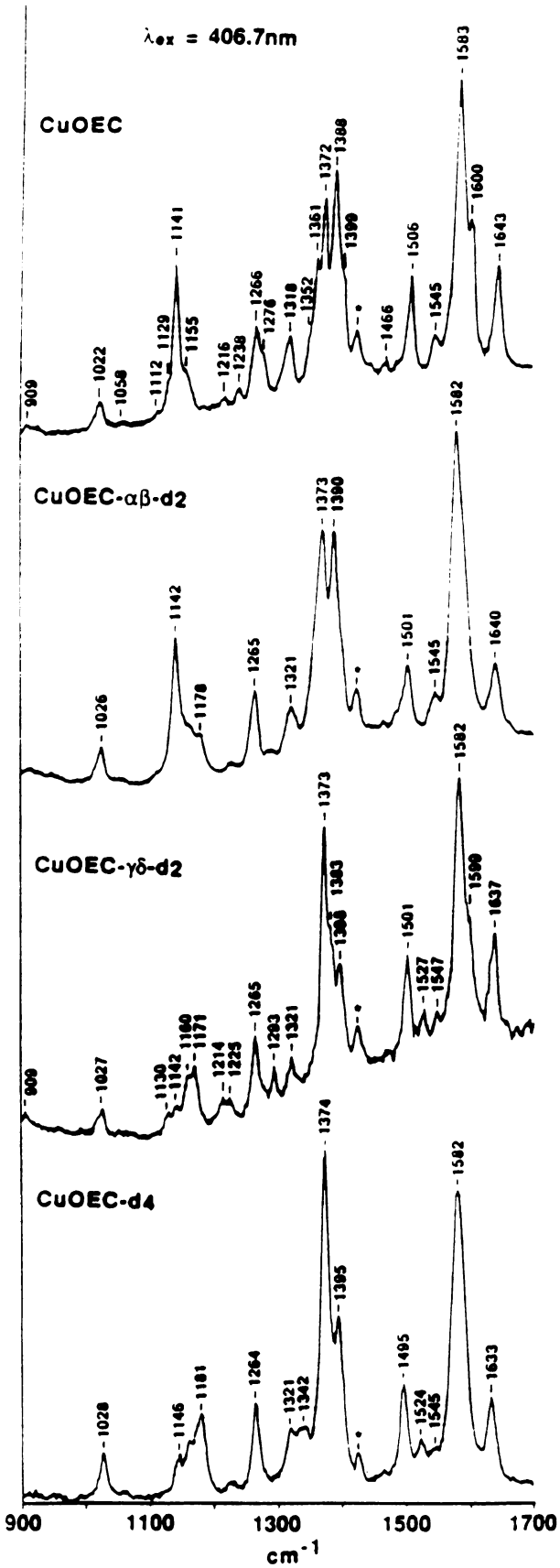
λex = 406.7nm
CuOEC
909
1022
1058
1112
1129
1155
1141
1216
1238
1266
1276
1318
1352
1361
1372
1388
1399
1466
1506
1545
1583
1600
1643
CuOEC-αβ-d2
1026
1142
1178
1265
1321
1373
1390
1501
1545
1582
1640
CuOEC-γδ-d2
900
1027
1130
1142
1160
1171
1214
1225
1265
1283
1321
1373
1501
1527
1547
1582
1590
1637
CuOEC-d4
1028
1146
1181
1264
1321
1342
1374
1395
1495
1524
1545
1582
1633
900
1100
1300
1500
1700
cm-1

(Figures 4-9 and 4-10) with those for CuOEC in Figure 4-11 and 4-12 shows a close correspondence in the modes observed and in the pattern of vibrational frequency shifts upon selective deuteration at the methine bridge positions (Table 4-6). Thus, a detailed discussion of the mode assignments is deferred to the normal coordinate analysis section below. Here, only some general observations and comments on the behavior of several of the modes in the high frequency region will be made.

The metal-dependent frequency differences between the correlated modes in Table 4-6 arise from the larger core size, and correspondingly lower macrocycle mode frequencies, for ZnOEC relative to CuOEC. These metal dependencies have been observed for metallochlorins by several authors[26,38,100,101] and correspond to the well-known core size dependence of metalloporphyrin macrocycle modes.[79] In the original work with CuOEC, our visible excitation Raman and IR data showed two prominent modes in the 1580 - 1605 cm^{-1} region. The ZnOEC data presented here and the normal coordinate calculations discussed below indicate that a third band should be apparent in this frequency region (for ZnOEC the corresponding region is 1565 - 1590 cm^{-1} and these three modes occur at 1569, 1571 and 1586 cm^{-1} in the h_4 species (Table 4-6)). Accordingly, higher resolution IR data for CuOEC and its specifically deuterated derivatives were recorded and the occurrence of a third mode in this region at 1583 cm^{-1} (Table 4-6) was revealed. Inspection of

Table 4-6. Vibrational Frequencies (cm^{-1}), Isotope Shifts (cm^{-1}), and Symmetries for the High-Frequency Modes of CuOEC[a,b] and ZnOEC[b].

CuOEC				ZnOEC				
H_4	$\Delta\alpha\beta$	$\Delta\gamma\delta$	Δd_4	H_4	$\Delta\alpha\beta$	$\Delta\gamma\delta$	Δd_4	sym
1644	-3	-7	-10	1623	-4	-9	-14	A
1602	-12	-2	-13	1586	-18	-3	-19	A
1584	-10	-4	-11	1569	-13	-1	-15	B
1583	-1	-1	-1	1571	0	0	0	A
1547	-1	0	-3	1538	-1	-2	-5	A
1543	0	-17	-17	1527	-1	-20	-20	B
1507	-6	-6	-13	1490	-6	-7	-9	A
1486[c]	-4	-7	-10					A

a : ref. 38
b : this work
c : enhanced by visible excitation

polarized resonance Raman (Figures 4-13 and 4-14) and IR spectra (Figure 4-10) of ZnOEC also revealed that the 1535 cm^{-1} band in the Soret excitation Raman spectrum (Figure 4-9) consists of a 1538 cm^{-1} polarized mode and a 1527 cm^{-1} anomalously polarized mode. The properties and frequency shift patterns of these modes correspond closely to those of the 1547 cm^{-1} and 1543 cm^{-1} modes in CuOEC.

The compilation of mode frequencies and deuteration shifts for CuOEC and ZnOEC in Table 4-6 shows that the frequency shift pattern observed for CuOEC upon selective methine deuteration is paralleled by that observed for the ZnOEC derivatives. The shift magnitudes for the Zn species are greater than those of the Cu complexes, however, owing to the lower C_aC_m mode frequencies and hence better mixing with C_mH deformations that occurs in ZnOEC. For several correlated modes in the two metallochlorins, the frequency shift patterns upon α,β-deuteration are distinct from those upon γ,δ-deuteration, which indicates that mode localization phenomena in the metallochlorins do not depend on the central metal but rather on the macrocycle symmetry, as suggested earlier.[36,38]

4.4.2) Vibrational Assignments for CuOEC

The vibrational assignments for the high-frequency (above 1000 cm^{-1}) skeletal modes of CuOEC are given in Table 4-7. These assignments were made on the basis of the frequencies, isotope shifts, and resonance Raman band

Figure 4-13 Polarized resonance Raman spectra of ZnOEC and ZnOEC-α,β-d_2 in CH_2Cl_2 solution obtained with Soret excitation at 406.7 nm. Laser power: 7 mW, concentrations: ~40 μM.

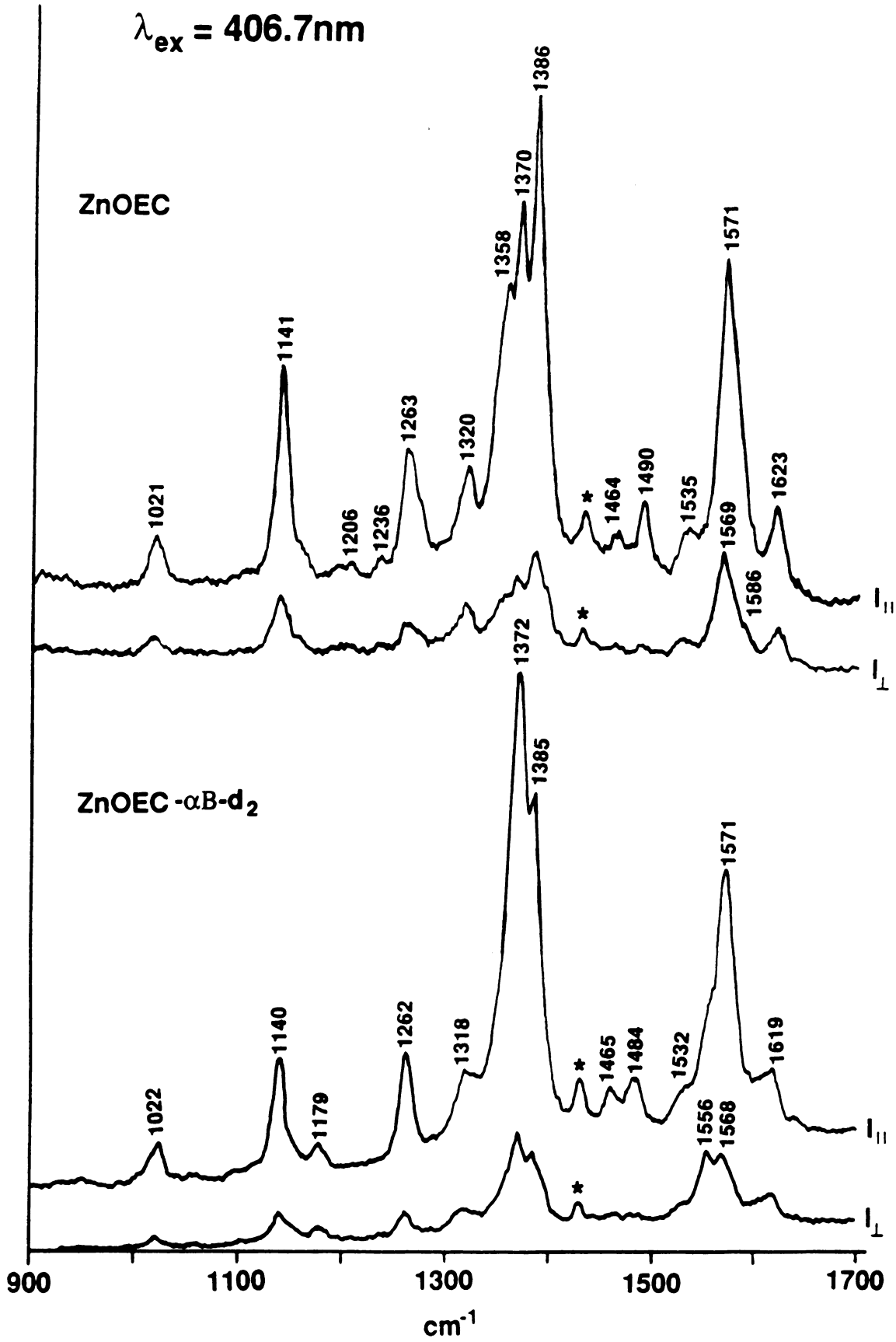
λex = 406.7nm
ZnOEC
1021
1141
1206
1236
1263
1320
1358
1370
1386
1464
1490
1535
1569
1571
1586
1623
I||
I⊥
ZnOEC -αB-d2
1022
1140
1179
1262
1318
1372
1385
1465
1484
1532
1556
1568
1571
1619
I||
I⊥
900
1100
1300
1500
1700
cm-1

Figure 4-14 Polarized resonance Raman spectra of ZnOEC-γ,δ-d_2 and ZnOEC-d_4 in CH_2Cl_2 solution obtained with Soret excitation at 406.7 nm. Laser power: 7 mW, concentrations: ~40 μM.

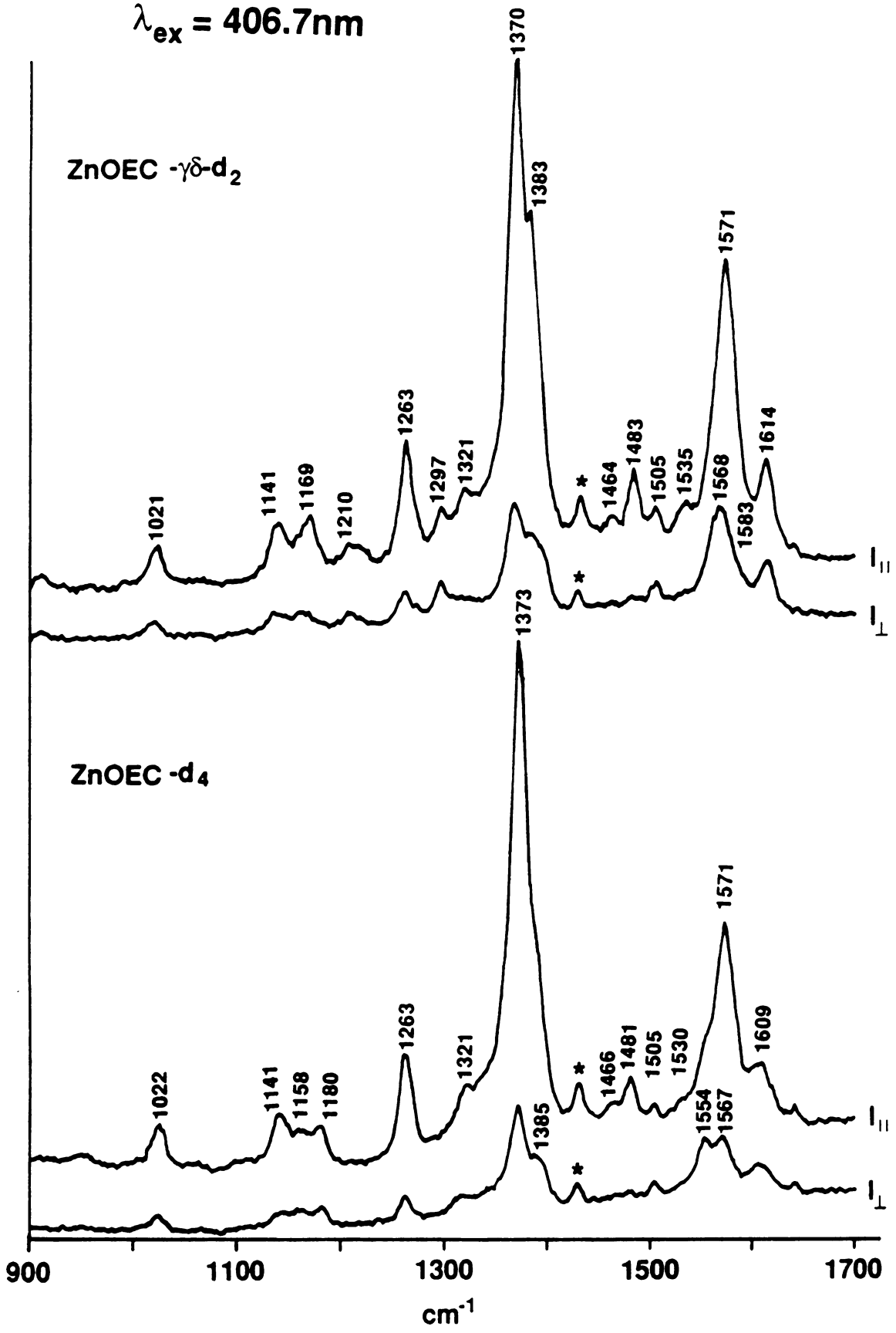
λex = 406.7nm
ZnOEC -γδ-d2
1370
1383
1571
1263
1321
1297
1141
1169
1210
1021
1464
1483
1505
1535
1568
1583
1614
I∥
I⊥
ZnOEC -d4
1373
1571
1263
1321
1141
1158
1180
1022
1466
1481
1505
1530
1554
1567
1609
1385
900
1100
1300
1500
1700
cm-1

Table 4-7 Observed[a] and Calculated[b] Frequencies and Isotope Shifts (cm^{-1}) for the High-Frequency Skeletal Modes of CuOEC

obsd				$\Delta\alpha\beta$-d_2		$\Delta\gamma\delta$-d_2		$\Delta\alpha\beta\gamma\delta$-$d_4$		$\Delta^{15}N$		
RR	IR	cald	sym	obsd	cald	obsd	cald	obsd	cald	obsd	cald	Assignment[d]
1644(p)[c]	1644	1645	A	3	1	7	11	10	14	0	0	57%$\nu C_aC_m(\gamma,\delta)$, 10%$\delta C_mH(\gamma,\delta)$
		1618	B		5		7		15		0	36%$\nu C_aC_m(\gamma,\delta)$, 30%$\nu C_aC_m(\alpha,\beta)$
1602(p)	1602	1616	A	12	11	2	5	13	14	1	0	52%$\nu C_aC_m(\alpha,\beta)$, 10%$\nu C_aC_m(\gamma,\delta)$, 10%$C_mH(\alpha,\beta)$
1584(dp)	1583	1582	B	10	8	4	14	11	18	0	0	32%$\nu C_aC_m(\gamma,\delta)$, 32%$\nu C_aC_m(\alpha,\beta)$
1583(p)		1571	A	2	3	1	0	1	3		0	27%νC_bC_b(III), 11%νC_bC_b(II,IV), 13%$\nu C_aC_m(\alpha,\beta)$
		1557	B		5		1		6		1	45%νC_bC_b(II,IV), 8%$\nu C_aC_m(\alpha,\beta)$, 4%$\nu C_aC_m(\gamma,\delta)$
1547(p)	1547	1561	A	1	0	0	1	3	2	0	1	28%νC_bC_b(II,IV), 20%νC_bC_b(III), 6%$\nu C_aC_m(\alpha,\beta,\gamma,\delta)$
1543(ap)	1543	1453	B	0	2	17	6	17	7		3	21%$\nu C_aC_m(\gamma,\delta)$, 9%$\nu C_aN(II_1,IV_1)$
1507(p)	1507	1491	A	6	3	6	4	13	9	1	1	15%$\nu C_aC_m(\alpha,\beta)$, 15%$\nu C_aC_m(\gamma,\delta)$, 20%$\nu C_bC_b$(II,IV)
1486(p)	1484	1470	A	4	5	7	7	10	10		2	21%$\nu C_aC_m(\gamma,\delta)$, 16%$\nu C_aC_m(\alpha,\beta)$, 12%$\nu C_aN$(II,IV)
1466(dp)		1461	B		4		1		7		2	22%$\nu C_aC_m(\alpha,\beta)$, 10%νC_aN(III)
1403(dp)		1392	B	0	4	4	0	7	3	1	1	32%νC_aC_b(III), 16%νC_bC_1
1388	1396	1385	B	2	5	5	0	4	5		1	26%νC_aC_b(II,IV), 16%νC_bC_1
1373(p)	1375	1386	A	3	1	2	1	2	2	6	1	29%νC_aC_b(II,IV), 20%νC_bC_1
1362(p)		1355	A		2		2		3	5	3	12%$\nu C_aN(II_2,IV_2,III)$, 9%νC_aC_b(III)

Table 4-7 (cont.) Observed[a] and Calculated[b] Frequencies and Isotope Shifts (cm^{-1}) for the High-Frequency Skeletal Modes of CuOEC.

obsd				$\Delta\alpha\beta$-d_2		$\Delta\gamma\delta$-d_2		$\Delta\alpha\beta\gamma\delta$-$d_4$		$\Delta^{15}N$		
RR	IR	cald	sym	obsd	cald	obsd	cald	obsd	cald	obsd	cald	Assignmentd
1352(p)		1343	A		3		2		5	4	3	17%$\nu C_aN(II_1,IV_1,III)$, 6%$\nu C_aC_b(III)$
1318(ap)	1318	1315	B	1	2	1	2	2	5	1	3	26%$\nu C_aN(II,IV)$, 22%$\nu C_aC_b(II,IV)$
		1313	A		1		2		3		4	20%$\nu C_aN(I,III)$, 9%$\nu C_aC_b(III)$, 7%$\nu C_aN(II,IV)$
1310		1291	B	+ 7	+6		424		394	5	4	19%$\nu C_aN(I)$, 18%$\delta C_mH(\gamma,\delta)$
		1305	B		198		0		197		1	8%$\delta C_mH(\alpha,\beta)$, 37%$CH_2$ twist
		1296	A		0		7		7		2	14%νCaN(I), 20%CH_2 twist
1277(ap)		1259	B	+11	0	+16	+17	+27	+16		2	13%$\nu C_aN(I)$, 13%$\nu C_aC_b(II_1,IV_1)$
1275(p)		1286	A	99	127	2	0	97	122		0	7%$\delta C_mH(\alpha,\beta)$, 52%CH2 twist
1238(p)		1258	A	292	308	14	1	292	263		+6	30%$\delta C_mH(\alpha,\beta)$, 20%$\nu C_aC_b(II_2,IV_2,III)$
1215(ap)	1211	1218	B		353	0	0		366		1	27%$\delta C_mH(\alpha,\beta)$, 17%$\nu C_aC_b(III)$
1198(p)	1197	1210	A	0	+2		289		263	0	3	35%$\delta C_mH(\gamma,\delta)$, 18%$\nu C_aC_b(I,II1,IV_1)$
1155(dp)		1130	B		0	0	+9		+9	10	6	24%$\nu C_aN(III)$, 22%νC_bC_1
1141(p)		1118	A	0	0	+32	+24	+32	+21	13	9	23%$\nu C_aN(II.IV_1)$, 18%νC_bC_1
1129(ap)	1128	1147	B	6	1	0	22	6	22	19	5	19%$\nu C_aC_b(I)$, 13%$\nu C_aN(I)$, 10%$\delta C_mH(\gamma,\delta)$
		1108	A		+176		0		+173		9	20%$\nu C_aN(II_2,IV_2)$, 14%$\delta C_mH(\alpha,\beta)$

Table 4-7 (cont.) Observed[a] and Calculated[b] Frequencies and Isotope Shifts (cm^{-1}) for the High-Frequency Skeletal Modes of CuOEC.

obsd				$\Delta\alpha\beta$-d_2		$\Delta\gamma\delta$-d_2		$\Delta\alpha\beta\gamma\delta$-$d_4$		$\Delta^{15}N$		
RR	IR	cald	sym	obsd	cald	obsd	cald	obsd	cald	obsd	cald	Assignment[d]
		1117	B		2		+114		+114		6	12%$\nu C_aN(II_1,IV_1)$, 12%νC_bC_1
		1108	B		+68		0		+75		3	17%$\nu C_aN(II_2,IV_2)$, 12%νC_bC_1
		1104	B		+182		+2		+189		8	24%νC_bC_1
		1092	A		+6		+10		+14		4	10%νC_aC_b(III), 8%δCmH(α,β), 8%$\delta C_mH(\gamma,\delta)$
		1088	B		+8		+10		+11		5	20%$\delta C_mH(\alpha,\beta,\gamma,\delta)$, 10%$\nu C_aN$(I,II,IV)
		1060	A		0		7		+6		7	15%νC_aC_b(I,III), 11%νC_1C_2
		1035	A		0		0		0		2	20%δC_aC_bH(I), 16%νC_aC_b(I)

[a]The resonance Raman and IR frequencies for CuOEC and the meso-deuteriated isotopomers were taken from ref. 38. The ^{15}N shifts are from ref. 100.

[b]Calculated with FFI

[c]Abbreviations: p = polarized; ap = anomolously polarized; dp = depolarized.

[d]Mode description are as follows: ν = stretch and δ = in-plane deformation. C_a, C_b, C_m and the characters in parentheses refer to the macrocyclic positions shown in Figure 1-3.

polarizations of the various modes. The calculated frequencies and potential energy distributions listed in the table were obtained with FFI. Table 4-8 compares the frequencies and meso-deuteration shifts for eight high-frequency skeletal modes calculated by using four different force fields (FF I ~ FF IV). The average errors between the observed and calculated frequencies and meso-deuteration shifts are compared for all four force fields in Table 4-9. These errors were determined on the basis of the 16 highest frequency observed resonance Raman bands and 37 meso-deuteration shifts. These bands correspond to C_aC_m, C_bC_b, C_aN and C_aC_b stretching motions.

4.5) Discussion

4.5.1) Vibrational Assignments

The molecular symmetry of metallochlorin is lowered to C_2 from D_{4h} for a planar metalloporphyrin macrocycle. The resonance Raman active and IR active vibrational modes belong to the A and B symmetry species of C_2 molecular symmetry. Table 4-10 represents the correlation of D_{4h} and C_2 in-plane modes. The selective meso-deuteration data, in conjuction with the normal coordinate calculations, have allowed us to refine the previous interpretation of the vibrational spectra of CuOEC.[36,38] These refinements are readily extended to the spectra of other MOEC complexes. Most of the modes above 1000 cm^{-1} can now be assigned with a

Table 4-8 Comparison of the Frequencies and Deuteration Shifts (cm^{-1}) for the Various Force Fields

		$\Delta\alpha,\beta$-d_2	$\Delta\gamma,\delta$-d_2	$\Delta\alpha,\beta,\gamma,\delta$-$d_4$
obsd.	1644	3	7	10
FF I	1645	1	11	14
FF II	1640	2	8	14
FF III	1646	3	7	13
FF IV	1642	1	12	15
obsd.	1602	12	2	13
FF I	1616	11	5	14
FF II	1617	10	8	15
FF III	1613	8	6	12
FF IV	1604	6	12	15
obsd.	1584	10	4	11
FF I	1582	8	14	18
FF II	1578	15	6	18
FF III	1590	12	4	14
FF IV	1581	13	7	18
obsd.	1583	2	1	1
FF I	1571	3	0	3
FF II	1576	3	1	3
FF III	1590	3	0	3
FF IV	1572	2	0	2

Table 4-8 (cont.) Comparison of the Frequencies and Deuteration Shifts (cm^{-1}) for the Various Force Fields

		$\Delta\alpha,\beta$-d_2	$\Delta\gamma,\delta$-d_2	$\Delta\alpha,\beta,\gamma,\delta$-$d_4$
obsd.	1547	1	0	3
FF I	1561	0	1	2
FF II	1561	0	2	2
FF III	1556	1	2	4
FF IV	1552	0	1	1
obsd.	1543	0	17	17
FF I	1453	2	6	7
FF II	1450	0	24	25
FF III	1474	4	18	21
FF IV	1466	2	6	10
obsd.	1507	6	6	13
FF I	1491	3	4	9
FF II	1492	1	6	8
FF III	1511	3	6	12
FF IV	1494	6	4	11
obsd.	1486	4	7	10
FF I	1470	5	7	10
FF II	1469	7	5	10
FF III	1486	7	11	16
FF IV	1474	3	7	10

Table 4-9 Average Errors Between the Observed and Calculated Frequencies and Deuteration Shifts for the Various Force Fields[a]

FF	Δcm^{-1}	$\Delta\Delta d(cm^{-1})$	description
I	13.5 (8.40)[b]	2.89 (2.47)	force field for NiOEC with scaled diagonal force constants
II	14.2 (9.00)	2.43 (2.20)	same as I with C_aC_m force constant reversed (see ref. 109)
III	11.6 (7.73)	2.48 (2.43)	skeletal diagonal force constant refined, 1,2 C_aC_m-C_aC_m interaction constant adjusted
IV	12.1 (7.86)	2.69 (2.35)	same as I but only 1,2 C_aC_m-C_aC_m and 1,4 C_aC_m-C_aC_m interaction constant adjusted

[a]Values tabulated from the 16 observed bands and 37 observed deuteration shifts in the 1650 - 1300 cm^{-1} region.

[b]Values in parentheses do not include the observed 1543 cm^{-1} band and its corresponding deuteration shifts.

Table 4-10 The correlation of D_{4h} and C_2 In-plane Modes

D_{4h}		C_2
A_{1g}(p)	→	A(p)
B_{1g}(dp)	→	A(p)
A_{2g}(ap)	→	B(ap, dp)
B_{2g}(dp)	→	B(dp)
E_u(IR)	→	A(p) + B(dp)

p = polarized
ap = anomalously polarized
dp = depolarized

reasonable degree of confidence. Many of the vibrational assignments reported in Table 4-7 are consistent with previous qualitative interpretations of the spectra of CuOEC. However, the new information reported herein necessitates the reevaluation of certain assignments. The specific assignments for selected high-frequency skeletal modes are discussed in more detail below.

4.5.1.1) C_aC_m Vibrations

There are eight C_aC_m vibrations expected in the high-frequency region (4 A and 4 B). Table 4-7 shows that seven of the eight modes are observed in the vibrational spectra (1644, 1602, 1584, 1543, 1507, 1486, 1466 cm^{-1}). The corresponding resonance Raman and IR bands of ZnOEC are tabulated in Table 4-6 and ref. 38 (The 1486 cm^{-1} band of CuOEC is only enhanced by visible excitation; for ZnOEC visible excitation measurements are not feasible owing to the huge fluorescence from the lowest excited singlet state.).

The only missing vibrational band is the highest frequency B-symmetry mode that is calculated at 1618 cm^{-1}. The skeletal mode frequencies of MOEC are observed to be metal dependent, and hence core-size dependent. The empirical expression[80] that relates vibrational frequency and core-size for a metalloporphyrin is:

$$\nu = K (A - d)$$

where ν is the vibrational frequency in cm^{-1}, K(cm^{-1}/Å) and A(Å) are parameters characteristic of the macrocycle, and d is the center to nitrogen distance, or core size, of the metalloporphyrin in Å. The physically useful parameter is the K value, which is proportional to the amount of C_aC_m stretching character in the vibrational mode. Fonda et al.[38] reported the core-size correlation parameters, K and A, for the high frequency modes of the Ni, Cu, and Zn complexes of OEC and OEP, respectively. They assumed the same core-size for porphyrin and chlorin complexes, namely Ni(1.958 Å)[82], Cu(2.000 Å)[132] and Zn(2.047 Å).[133] In the study of NiOEC by Bocian et al.[36] the corresponding band for the mode calculated at 1618 cm^{-1} in CuOEC (the highest B symmetry mode) was observed near 1644 cm^{-1}; this vibration could be the analog of the missing C_aC_m mode of CuOEC. Because the core-size correlation parameters (K and A) are positive, the corresponding resonance Raman band of CuOEC compared to NiOEC would be expected at lower frequency. These expectations are supported by observed and calculated frequencies.

In a previous resonance Raman study of CuOEC, Ozaki et al.[100] assigned the 1602 cm^{-1} band to a totally symmetry C_bC_b stretching motion. However, the meso-deuteration data indicate that this band is associated with a C_aC_m mode localized on the α,β-methine bridges (ref.38 and this work).

The careful investigation of IR and resonance Raman spectra shows that the composite 1583 cm^{-1} band in CuOEC is

composed of 1584 and 1583 cm^{-1} bands. The measurement of the polarization ratio reveals that the 1584 cm^{-1} band is the depolarized B symmetry mode and the 1583 cm^{-1} band is the polarized A symmetry mode. Furthermore, the 1584 cm^{-1} band shows strong isotope dependence upon deuteration of the methine chlorins. On the other hand, the frequency shifts of the 1583 cm^{-1} band for the methine deuteriated chlorins is not great. The 1584 cm^{-1} band reported by Fonda et al.[38] showed isotope shifts for meso-deuteration and frequency shifts on change of peripheral substituents from CuOEC to copper etiochlorin I (CuECI). Although these researchers were not aware that this spectral feature is actually composed of two modes, it is now clear that the 1584 cm^{-1} band is a mixture of two modes (C_aC_m and C_bC_b). Therefore, the 1584 and 1583 cm^{-1} modes are assigned to C_aC_m and C_bC_b stretching modes, respectively. The normal coordinate calculation presented in this work also supports this interpretation (see Table 4-7).

Compared to CuOEC, the corresponding mode frequencies of ZnOEC are generally lower owing to the core-size effect. Moreover, the frequency shift magnitudes of meso-deuterated ZnOEC are greater than those of CuOEC because the lower frequency C_aC_m modes in ZnOEC can mix better with the C_mH deformations. However, the investigation of IR, resonance Raman and polarization ratios for ZnOEC also reveals that the deuteration shift patterns are virtually the same as those for CuOEC (see Table 4-6). This means that the

vibrational mode localization phenomenon in chlorin complexes does not depend on the central metal in the chlorin, but rather the symmetry of chlorin.

One other C_aC_m vibration is evident in the CuOEC spectrum; that is the mode observed at 1543 cm^{-1} in both the IR and Soret excited resonance Raman. This mode is not enhanced by visible excitation and is assigned as a B-symmetry, γ,δ-methine bridge localized C_aC_m vibration on the basis of its resonance Raman polarization (anomalous) and meso-deuteration shift pattern (0 cm^{-1} in CuOEC-α,β-d_2; 17 cm^{-1} in both CuOEC-γ,δ-d_2 and CuOEC-d_4). In addition, an analog of this mode is observed at 1527 cm^{-1} in ZnOEC. The IR spectrum of ZnOEC shows that the 1535 cm^{-1} resonance Raman band of ZnOEC is a mixture of the 1538 and 1527 cm^{-1} vibrational modes. Similar to the 1543 cm^{-1} band of CuOEC, this band shows the anomalous polarization and a similar frequency shift pattern to that for the meso-deuterated chlorins (1 cm^{-1} in ZnOEC-α,β-d_2; 20 cm^{-1} in both ZnOEC-γ,δ-d_2 and ZnOEC-d_4). However, the frequency of this band is anomalously high compared to the calculated frequency and is not reproduced in any force field calculations reported herein (Tables 4-3 and 4-8).

4.5.1.2) C_bC_b Vibrations

There are three C_bC_b vibrations expected in the high-frequency region (2 A and 1 B). The fourth C_bC_b stretch is associated with the reduced ring and expected at lower

frequency. Of the three high-frequency C_bC_b vibrations of CuOEC, the two A-symmetry modes are observed in the vibrational spectra (1583 and 1546 cm^{-1}). For ZnOEC, the corresponding bands are observed at 1571 and 1538 cm^{-1}, respectively. The methine deuteration behavior and normal coordinate analysis of these two modes demonstrate that there is mixing of the C_aC_m and C_bC_b internal coordinates. But the contribution of the C_aC_m internal coordinate is not great. The B-symmetry band is not observed for CuOEC but is calculated at 1557 cm^{-1} (FF I). In NiOEC[36,38,109], the analog of the B-symmetry band is observed at 1572 cm^{-1}. Accordingly, the B-symmetry vibration of CuOEC would most likely fall in the 1560 - 1570 cm^{-1} region.

4.5.1.3) C_aC_b and C_aN Vibrations

Under C_2 symmetry, there are eight C_aN and six C_aC_b modes expected in the high-frequency region (4 A and 4 B; 3 A and 3 B, respectively). Two other C_aC_b modes are associated with the reduced ring and expected at lower frequency. The C_aC_b and C_aN vibrations are extensively mixed with one another and with other motions of the macrocycle (Table 4-7). Consequently, it is not generally appropriate to classify the observed bands as a specific type of mode. Inspection of the vibrational data for CuOEC reveals that there are eight prominent bands that can be associated with C_aC_b and C_aN vibrations (1403, 1388, 1373, 1362, 1318, 1155, 1141 and 1129 cm^{-1}). All of these bands have analogs in the

spectra of ZnOEC and NiOEC.[36,38] Most of them have been identified on the basis of their ^{15}N shifts. Furthermore, the vibrational frequencies of ZnOEC, CuOEC and NiOEC that can be associated with C_aC_b and C_aN modes are very similar. This means that the C_aC_b and C_aN modes in chlorin complexes do not depend on the central metal in the chlorin.

4.5.1.4) C_mH Vibrations

There are four C_mH deformations (2 A and 2 B). These modes are extensively mixed with other vibrations of the macrocycles as is evidenced by the complicated meso-deuteration shift patterns observed in the 1100 - 1300 cm^{-1} spectral region. On the basis of the spectral data for CuOEC and the normal coordinate calculations, the bands at 1310, 1238, 1215 and 1198 cm^{-1} (Figure 4-11) are assigned as the four C_mH deformations. Boldt et al.[36] assigned the 1310 cm^{-1} band as a mode localized on the α,β-methine bridges. However, normal coordinate calculations presented here and careful investigation of spectra indicate that the motion is actually localized on the γ,δ-methine bridges. These assignments for the C_mH deformation were derived in the following manner. In case of the B-symmetry 1310 cm^{-1} band based on the normal coordinate calculations, a large meso-deuteration shift is observed in CuOEC-γ,δ-d_2 and CuOEC-d_4. This is not immediately apparent because the spectra of both of these isotopomers exhibit an anomalously polarized band in the 1320 - 1325 cm^{-1} region.[38] However, this latter band

is actually the analog of a band observed at 1318 cm^{-1} in the normal isotopomer. In CuOEC, this band is very weak, but its intensity increases in CuOEC-γ,δ-d_2 and CuOEC-d_4. The fact that the 1318 cm^{-1} band is a different mode not associated with a C_mH deformation is clearly revealed in both the IR and resonance Raman spectra of CuOEC-d_4, which exhibit a strong band in this region. The apparent absence of the 1310 cm^{-1} band in the spectrum of CuOEC-α,β-d_2 is due to the fact that this mode upshifts approximately 10 cm^{-1} in this isotopomer and becomes a shoulder on the low-energy side of the 1318 cm^{-1} band. This upshift is predicted by the normal coordinate calculations (Table 4-7). The band associated with the A-symmetry analog of the 1310 cm^{-1} vibration is more difficult to identify. The 1198 cm^{-1} band is attributed to this mode on the basis of its selective shifts in the spectra of CuOEC-γ,δ-d_2 and CuOEC-d_4. The assignment of the 1238 and 1215 cm^{-1} bands as the A and B symmetry C_mH deformations localized on the α,β-methine bridges was also based on the selective meso-deuteration shifts of these bands. Both of these modes are observed in the spectra of CuOEC-γ,δ-d_2 and both are absent in the spectra of CuOEC-α,β-d_2 and CuOEC-d_4.[33]

In addition to the four bands discussed above, several other modes are quite sensitive to meso-deuteration. In particular, the 1275 cm^{-1} band appears to be comprised of two meso-deuteration sensitive bands (one polarized and the other anomalously polarized). In CuOEC-α,β-d_2, the

anomalously polarized band upshifts to 1288 cm^{-1}, while the polarized band downshifts to 1178 cm^{-1}. This reveals a band at 1263 cm^{-1} which is attributable to a CH_2 deformation of the ethyl group[125]. In CuOEC-γ,δ-d_2, the anomalously polarized band upshifts to approximately 1293 cm^{-1}, while the polarized band does not shift. Deuteration sensitivity is also observed for the 1141 cm^{-1} band. In CuOEC-α,β-d_2, this mode does not shift, whereas in CuOEC-γ,δ-d_2 this mode upshifts to 1173 cm^{-1}. In CuOEC-d_4, the 1141 cm^{-1} band upshifts to 1180 cm^{-1}. This band falls at nearly the same frequency as the 1178 cm^{-1} band of CuOEC-α,β-d_2 (1275 cm^{-1} of the normal isotopomer). Consequently, the 1180 cm^{-1} band of CuOEC-d_4 is probably a superposition of the upshifted 1141 cm^{-1} and downshifted 1275 cm^{-1} bands.

4.5.2) Comparison of the Force Fields

4.5.2.1) General Features of the Calculations

The objectives of performing normal coordinate calculations on CuOEC were to develop a satisfactory force field for MOEC complexes and to determine the factors that influence the vibrational eigenvectors. The forms of the eigenvectors were obtained from the normal coordinate calculations to confirm the mode localization effect. The semiempirical calculations on MOEC by Boldt et al.[31] predict that the normal modes of the metallochlorins are different from those of metalloporphyrins. In particular, the

semiempirical method predicts that the vibrational eigenvectors of a number of the skeletal modes are localized on specific sectors of the macrocycle. The localization was most pronounced in the vibrations involving the methine bridges. This localization phenomenon was attributed to the length alteration pattern that occurs in the C_aC_m bonds of the OEC macrocycle.[17,129,130] Indeed, the vibrational data obtained for selectively meso-deuterated CuOEC and ZnOEC support the idea of localized eigenvectors for certain modes.[38] On the other hand, the the normal coordinate calculations on NiOEC by Prendergast and Spiro[109] predict that the vibrational eigenvectors of this complex are delocalized and are generally similar to those of NiOEP. However, their calculations are not based on sufficient experimental data (they did not use the experimental data for NiOEC-α,β-d_2 and NiOEC-d_4). Limited experimental data can produce incorrect calculated results in a normal coordinate analyses.

Normal coordinate calculations based on a series of meso-deuterated CuOEC(CuOEC, CuOEC-α,β-d_2, CuOEC-γ,δ-d_2 and CuOEC-d_4) predict that certain vibrational eigenvectors are localized. The localization phenomenon is manifested regardless of the quality of fit to the experimental data. The localization is particularly apparent in modes associated with the C_aC_m stretches and C_mH deformations. These are illustrated in Figures 4-15-18, which depict selected vibrational eigenvectors for CuOEC. These

Figure 4-15 Vibrational eigenvectors of CuOEC which contain substantial contributions from C_sC_m stretching vibrations. Displacements are shown only for those atoms whose motions contribute significantly to the normal mode (10% or greater of the maximum atomic displacement of a given mode).

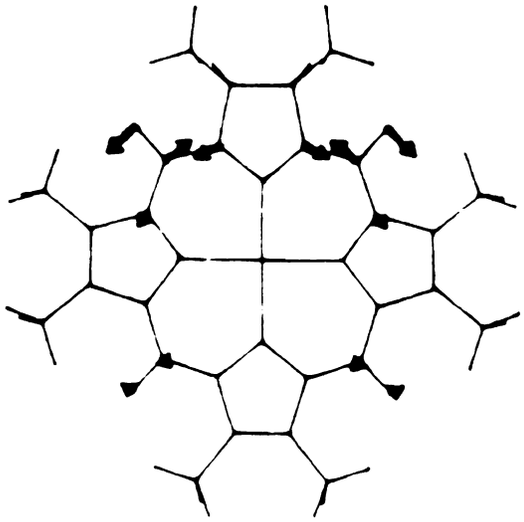

calc. 1645
obs. 1644

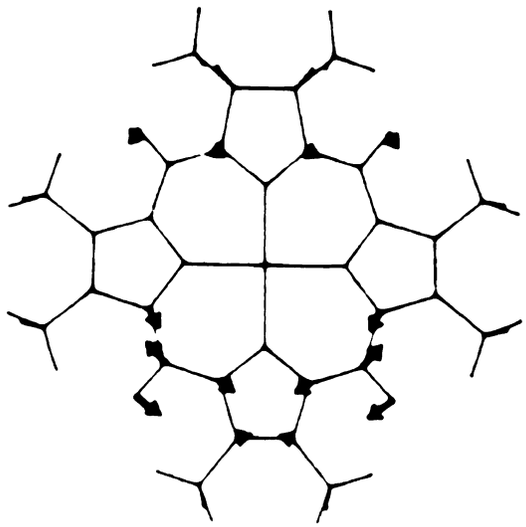

calc. 1616
obs. 1602

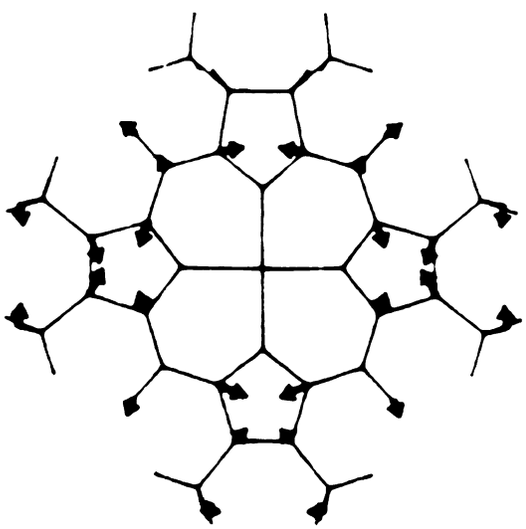

calc. 1491
obs. 1507

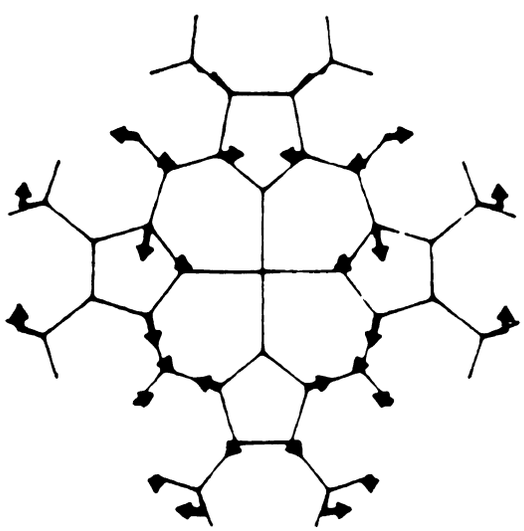

calc. 1470
obs. 1486

Figure 4-15 (cont.) Vibrational eigenvectors of CuOEC which contain substantial contributions from C_aC_m stretching vibrations. Displacements are shown only for those atoms whose motions contribute significantly to the normal mode (10% or greater of the maximum atomic displacement of a given mode).

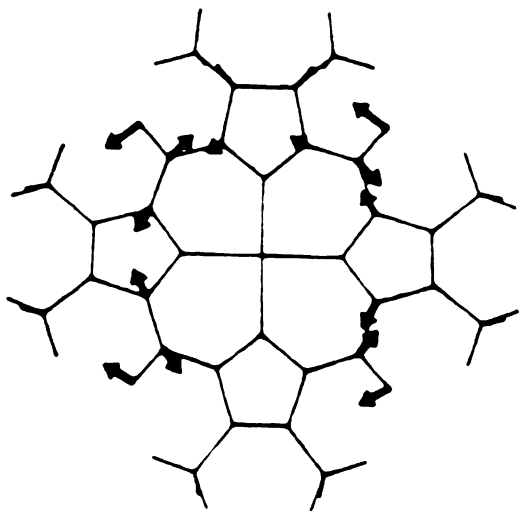

calc. 1618
obs. ----

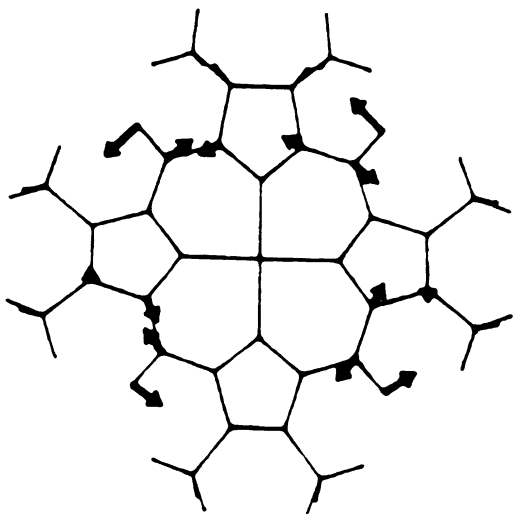

calc. 1582
obs. 1584

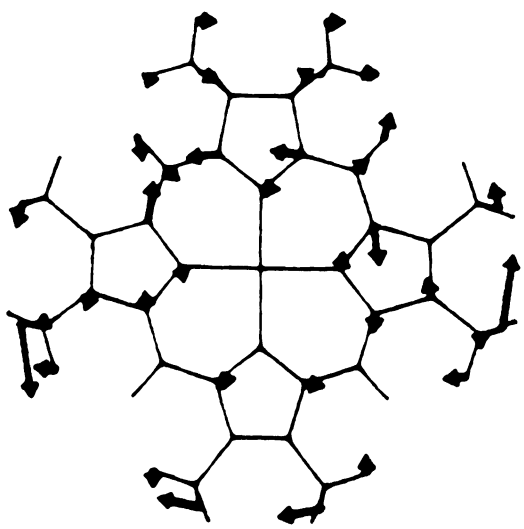

calc. 1453
obs. 1543

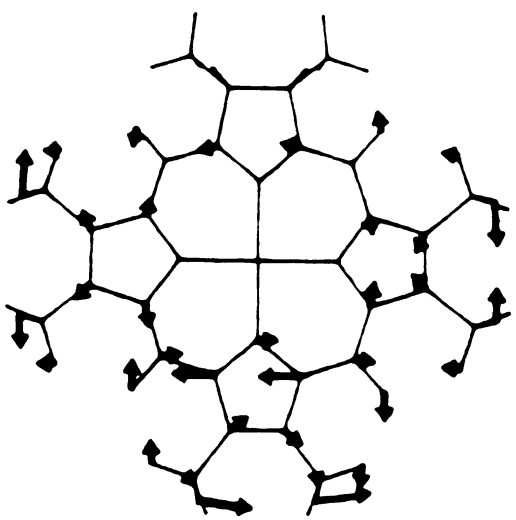

calc. 1461
obs. 1466

Figure 4-16 Vibrational eigenvectors of CuOEC which contain substantial contributions from C_bC_b stretching motions. Displacements are shown only for those atoms whose motions contribute significantly to the normal mode (10% or greater of the maximum atomic displacement of a given mode).

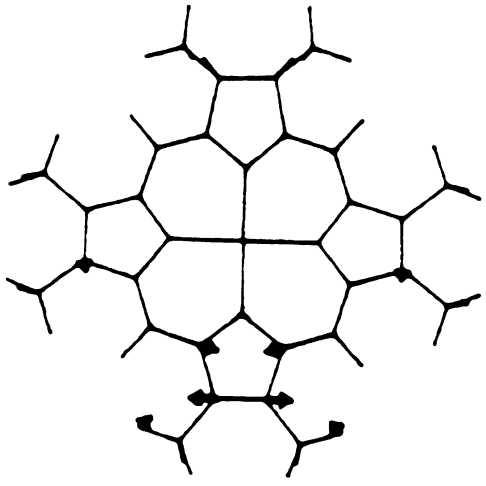

calc. 1571
obs. 1583

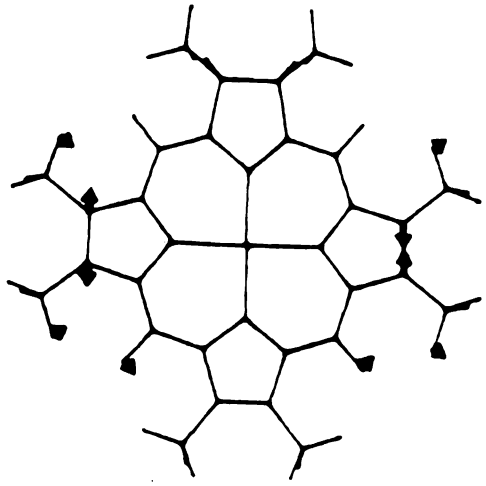

calc. 1557
obs. ----

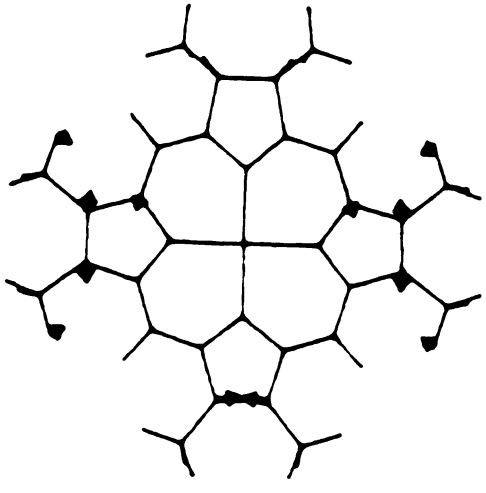

calc. 1561
obs. 1547

Figure 4-17 Vibrational eigenvectors of CuOEC which contain substantial contributions from $C_{\alpha}H$ deformations. Displacements are shown only for those atoms whose motions contribute significantly to the normal mode (10% or greater of the maximum atomic displacement of a given mode).

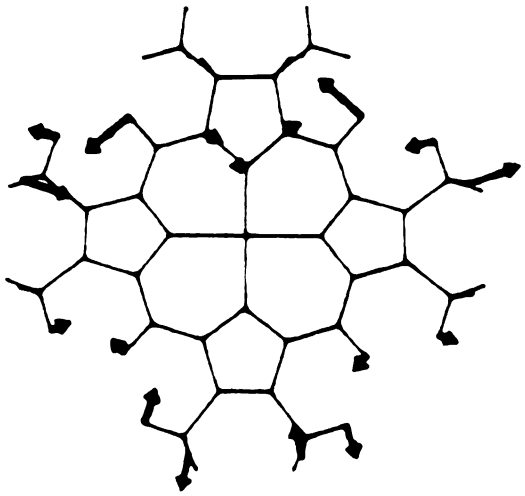

calc. 1291
obs. 1307

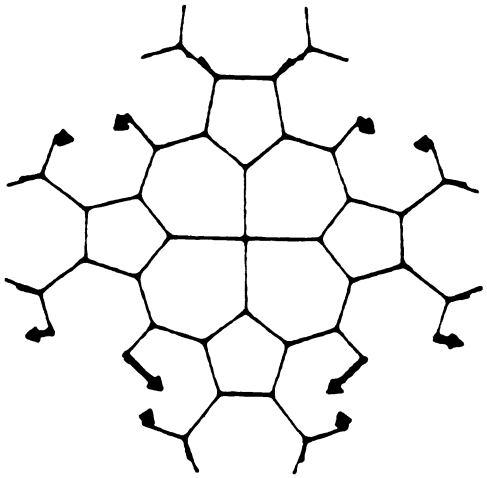

calc. 1218
obs. 1238

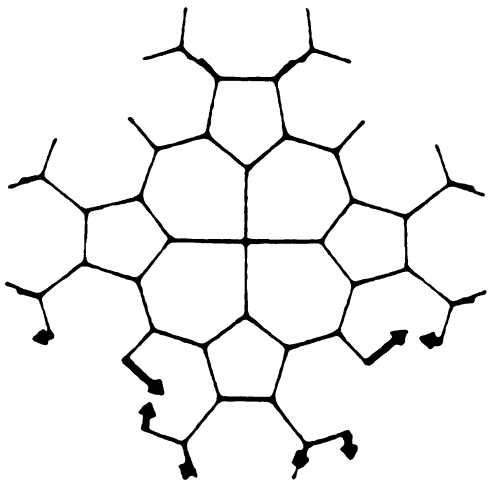

calc. 1218
obs. 1215

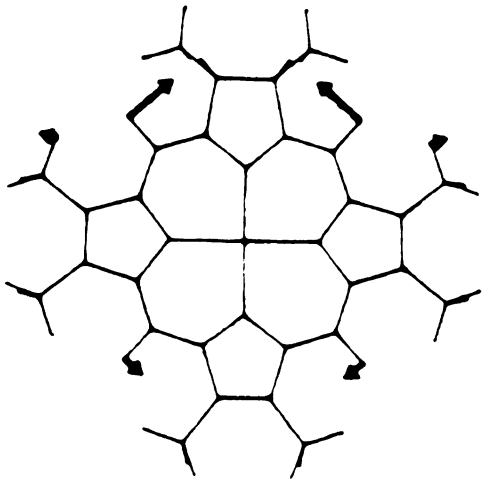

calc. 1210
obs. 1198

Figure 4-18 Vibrational eigenvectors of CuOEC which contain substantial contributions from both C_aC_b and C_aN stretching vibrations. Displacements are shown only for those atoms whose motions contribute significantly to the normal mode (10% or greater of the maximum atomic displacement of a given mode).

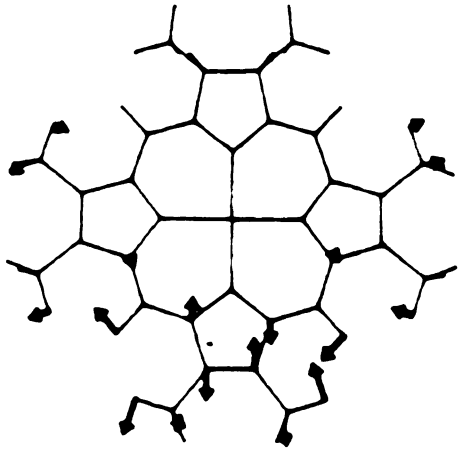

calc. 1392
obs. 1403

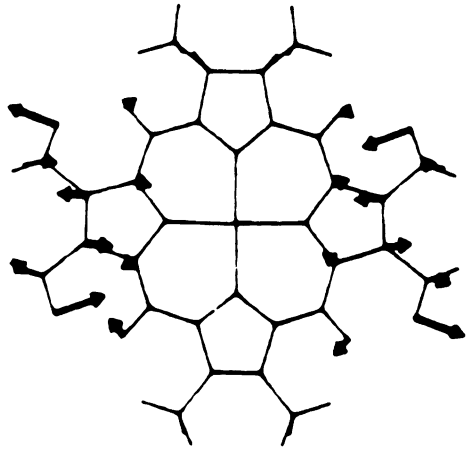

calc. 1385
obs. 1388

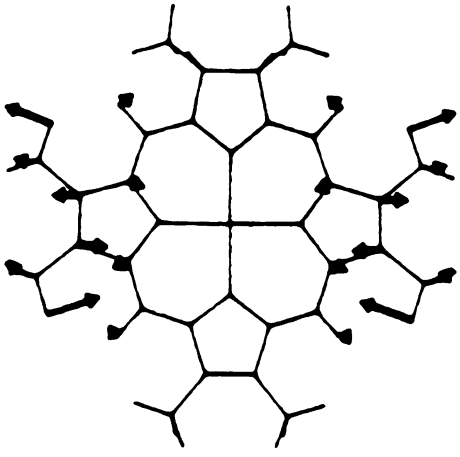

calc. 1386
obs. 1373

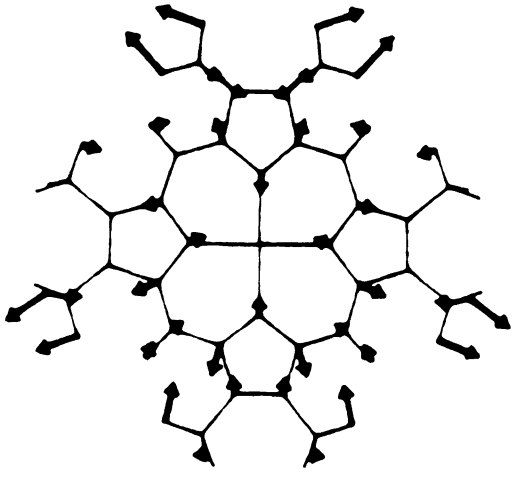

calc. 1355
obs. 1362

Figure 4-18 (cont.) Vibrational eigenvectors of CuOEC which contain substantial contributions from both C_aC_b and C_bN stretching vibrations. Displacements are shown only for those atoms whose motions contribute significantly to the normal mode (10% or greater of the maximum atomic displacement of a given mode).

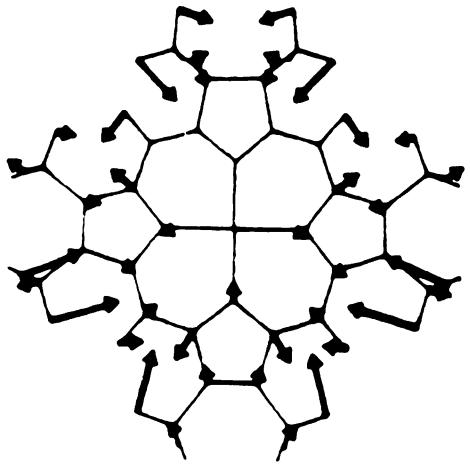

calc. 1343
obs. 1352

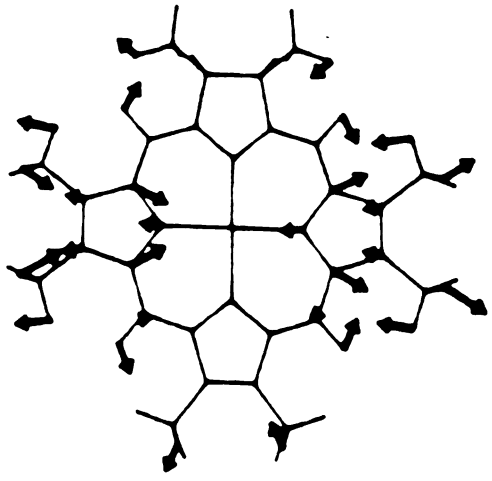

calc. 1315
obs. 1318

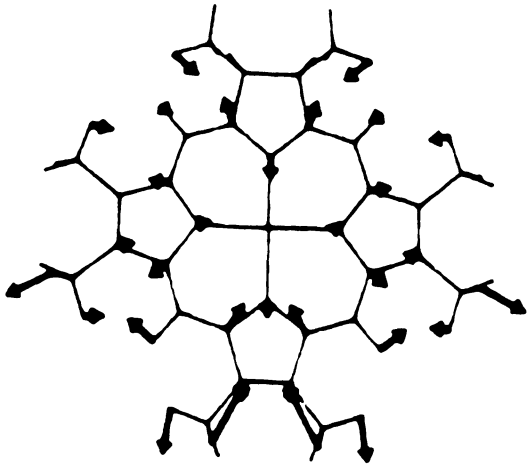

calc. 1313
obs. ----

eigenvectors were calculated by using FF I. On the basis of these results, it is clear that mode localization is a general consequence of symmetry lowering and does not depend on the fine details of the force field or the central metal. This conclusion is further supported by the observation that the isotope-shift patterns observed for selectively meso-deuteriated ZnOEC are virtually identical to those observed for CuOEC. Furthermore, Li and Zgierski[134] recently reported detailed normal coordinate calculations for free base and Ni(II) porphine. Similar localization occurs as a consequence of the bond-length disparities that occur in the low symmetry free base. The localization is apparent in the eigenvectors of free base porphyrin despite the fact that the bond length disparities[82] are significantly smaller than those in MOEC complexes.[17,129,130]

4.5.2.2) Relative Merits of Individual Force Fields

Inspection of Table 4-8 reveals that FF I - FF IV are approximately comparable in their quality as judged by the calculated average errors in the frequencies and meso-deuteration shifts. However, none of these force fields adequately reproduces all of the detailed spectral features. For example, the mode observed at 1602 cm^{-1} downshifts 12 cm^{-1} upon α,β-methine deuteration, but only 2 cm^{-1} upon γ,δ-methine deuteration. FF I predicts shifts of 11 cm^{-1} and 5 cm^{-1}, respectively, which is a reasonable representation of the observed shift pattern. In contrast, FF II predicts

shifts of 10 cm^{-1} and 8 cm^{-1}; FF III predicts shifts of 8 cm^{-1} and 6 cm^{-1}; FF IV predicts shifts of 6 cm^{-1} and 12 cm^{-1}. These predicted shift patterns are considerably less satisfactory than those obtained with FF I. On the other hand, FF I fails to predict the shift pattern observed for the 1584 cm^{-1} band, whereas the other three force fields give a satisfactory representation of the observed pattern. As Table 4-8 shows, the 1584 cm^{-1} band downshifts 10 cm^{-1} upon α,β-methine deuteration and 4 cm^{-1} upon γ,δ-methine deuteration. FF I predicts shifts of 8 cm^{-1} and 14 cm^{-1}, respectively. FF II predicts shifts of 15 cm^{-1} and 6 cm^{-1}; FF III predicts shifts of 12 cm^{-1} and 4 cm^{-1}; FF IV predicts shifts of 13 cm^{-1} and 7 cm^{-1}. In the case of the 1543 cm^{-1} band, although FF II and FF III do give a satisfactory representation of the observed shift pattern, all of the force fields significantly underestimate the frequency of this mode. This mode alone accounts for approximately 30% of the average error in the frequencies (Table 4-9). This may suggest that higher order interaction, not accounted for in the valence force fields, is important in the MOEC macrocycle. Even if none of these force fields exactly reproduce all of the observed shift patterns, these force fields give a reasonable accounting of the vibrational characteristics of MOEC complexes.

One of the criteria that has been used in deriving a satisfactory force field is the requirement that the force constants scale with the bond lengths.[109,128] Of the

calculations reported here, this requirement is met by FF I and FF IV. In contrast, the force constants used for the C_aC_m bonds in FF II are in reverse order from those that should be used based on the bond lengths. In the case of FF III, the refinement increases the $C_a(II_1)$-N(II) stretching force constant from 5.411 mdyn/Å to 7.168 mdyn/Å. Simultaneously, the C_aC_m force constant for the bond adjacent to ring I is reduced from 6.819 mdyn/Å to 5.138 mdyn/Å. Both of these refined values are unreasonable based on the lengths of the C_aC_m and C_aN bonds in tetrapyrrolic macrocycles.[135] Regardless, both FF II and FF III give reasonable average errors in both the frequencies and meso-deuteration shifts. Indeed, by these criteria, FF III is the "best". Accordingly, the bond-length criterion, while appealing, is not necessarily a satisfactory indictor of the merit of a force field. Li and Zgierski[134] found that the inclusion of certain 1,4 interaction constants was important in obtaining an accurate force field for porphines. In the calculations on CuOEC, the effects of 1,4 interactions were explored only in a limited fashion. A detailed assessment of the effects of these (and higher order) interactions is not possible because there are a large number of these types of interactions and the experimental information is too limited to allow an evaluation of their importance.

4.6) Summary and Conclusion

The valence force field calculations reported herein indicate that various force fields satisfactorily reproduce the general features of the vibrational spectra of CuOEC. However, none of these force fields reproduces the frequencies and meso-deuteration shift patterns of all of the modes. This suggests that 1,4 and higher interaction constants make substantial contributions to the valence force field.

Meso-deuteration shift patterns of CuOEC and ZnOEC show that mode localization phenomena are not properties of the central metal but those of metallochlorin symmetry. All of the empirical force fields predict that the eigenvectors of certain skeletal modes are localized on sectors of the macrocycle. This result is in general agreement with the prediction of the QCFF/PI calculation by Boldt et al.[36]

CHAPTER 5

CONCLUSIONS AND FUTURE WORK

The goal of this research project was to explore the effects of lower symmetry in modified macrocycles by means of investigating the electronic and vibronic properties of metalloporphycenes and metallochlorins.

Metalloporphycenes, which are isomers of the extensively studied metalloporphyrins, qualify as potential agents for tumor marking and photodynamic therapy owing to their high absorption intensity in the wavelength region above 620nm.[33-35] Furthermore, metalloporphycene represents an example of a macrocycle of true D_{2h} symmetry, which is approximated by heme a and metallobacteriochlorins.[41-42] For these reasons the electronic and vibronic properties of porphycenes are extremely interesting. The lower symmetry (D_{2h}) of metalloporphycene compared to the D_{4h} symmetry of metalloporphyrin lifts x, y degeneracy and reduces configuration interactions in the electronic transitions of metalloporphycene. Close investigation of absorption band positions demonstrates that the $\pi \rightarrow \pi^*$ states of metalloporphycenes are adequately defined by one-electron wave functions, unlike those of metalloporphyrins.

Vibrational analyses of resonance Raman spectra of NiPPC, NiPPC-d_4(py) and NiPPC-d_4(et) give some insight into the normal mode composition. However, more complete vibrational analyses should be executed by normal coordinate calculations based on the vibrational data of additional isotopically substituted compounds (for example ^{15}N substitutied metalloporphycene). Vibrational eigenvectors based on the normal coordinate calculations will help to understand the consequences of symmetry-lowering in metalloporphycene. The vibrational properties of metalloporphyrins in biological systems are influenced by the central metal, axial ligation, peripheral substitution, ring oxidation, reduction etc. Therefore, the vibrational properties of metalloporphycenes for CO or CN^- bounding as axial ligands and for porphycene cations or anions will be one of the interesting fields to investigate in the future.

Metallochlorin is a metalloporphyrin derivative in which a C_aC_b bond of one of the pyrrole rings has been reduced.[9] Metallochlorins are ubiquitous in nature, occurring as the chlorophyll pigments in photosynthetic systems[10], in marine worm pigments[11] etc. Reduction of a C_bC_b bond in a metalloporphyrin lowers the molecular symmetry from D_{4h} to C_2 and has a profound effect on the entire macrocycle. Therefore, the vibrational characteristics of the metallochlorins are particularly important for gaining an understanding of symmetry-lowering effects in modified macrocycles. Accordingly, many groups[36,38,109] have studied the

vibrational data. There remain, however, some controversies in the interpretation of the vibrational modes of metallochlorins. As discussed in chapter 4, the main disagreement involves vibrational mode localization effects in metallochlorins. Bocian et al.[36] have examined NiOEC by using a semiempirical quantum force field (QCFF/PI) method. Their calculations predict that the forms of the vibrational eigenvectors in metallochlorins are in general different from those of porphyrins. In contrast, empirical calculations (GF matrix method) on NiOEC by Prendergast and Spiro[109] predict that the vibrational eigenvectors of metallochlorins are similar to those of metalloporphyrins. The origin of the disagreements between the empirical and semiempirical normal coordinate calculations on NiOEC is not clear. One possible reason for disagreement is limited experimental data. For the development of an accurate empirical force field it is necessary to obtain data from a variety of isotopomers. As a result of normal coordinate calculations for CuOEC, a good start in understanding the controversy for mode localization effects in chlorin has been made and the vibrational mode properties in chlorins can be understood more clearly.

As described in this dissertation, normal coordinate calculations based on the IR and resonance Raman spectra of selectively meso-deuterated CuOEC (CuOEC-h_4, CuOEC-$\alpha\beta$-d_2, CuOEC-$\gamma\delta$-d_2, CuOEC-d_4) show that the eigenvectors of certain skeletal modes are localized on sectors of the macrocycle.

The meso-deuteration shift patterns of CuOEC and ZnOEC show that mode localization phenomena are not dependent on the identity of the central metal but are inherent properties of metallochlorins that result from their reduced symmetry. Therefore, normal coordinate calculations by using selectively meso-deuterated ZnOEC vibrational spectroscopic data will be useful in testing and exploring the effect of mode localization in lower symmetry macrocycles. Like metalloporphyrins, the vibrational properties of metallochlorins will be influenced by the central metal, axial ligation, peripheral substitution, ring oxidation, reduction etc. Therefore, an analysis of the vibrational properties of metallochlorins within the centext of these factors will help in providing an understanding of the reduced macrocycle. Once the mode assignments for metallochlorins have been firmly established, the vibrational properties of metallochlorins in biological systems will be an interesting topic for investigation.

LIST OF REFERENCES

LIST OF REFERENCES

1. Dolphin,D., Ed. The Porphyrin; Academic Press: New York, 1978; Vol. I

2. Dolphin,D., Ed. The Porphyrin; Academic Press: New York, 1978; Vol. VII

3. Vogel,E.; Kocher,M.; Schmickler,H.; Lex,J. Angew. Chem., Int. Ed. Engl. 1986, 25, 257-259.

4. Vogel,E.; Balci,M.; Pramod,K.; Koch,P.; Lex,J.; Ermer,O.; Angew. Chem., Int. Ed. Engl. 1987, 26, 928-931.

5. a) Vogel,E.; Kocher,M.; Balci,M.; Teichler,I.; Lex,J.; Schmickler,H.; Ermer,O. Angew. Chem., Int. Ed. Engl. 1987, 26, 931-934. b) Furenlid,L.R.; Renner,M.R.; Smith,K.M.; Fajer,J. J. Am. Chem. Soc. 1990, 112, 1634-1635.

6. Wehrle,B.; Limbach,H.-H.; Kocher,M.; Ermer,O.; Vogel,E. Angew. Chem., Int. Ed. Engl. 1987, 26, 934-936.

7. Schulpmann,J.; Huber,M.; Toporowicz,M.; Kocher,M.; Vogel.E.; Levanon,H.; Mobius,K. J. Am. Chem. Soc. 1988, 110, 8566-8567.

8. Vogel,E.; Kocher,M.; Lex,J.; Ermer,O. Irs. J. Chem. 1989, 29, 257-266.

9. Scheer,H. in The Porphyrin; Dolphin,D., Ed.; Academic Press: New York, 1978; Vol. VII, pp 1-44.

10. Svev,W.A. in The Porphyrin; Dolphin,D., Ed.; Academic Press: New York, 1978; Vol. V, pp 341-399.

11. Ballantine,J.A.; Psaila,A.F.; Pelter,A.; Murray-Rust,P.; Ferrito,V.; Schembri,P.; Jacaarini,V. J. Chem. Soc., Perkin Trans. I, 1980, 1080-1089.

12. Babcock,G.T.; Ingle,R.T.; Oertling,W.A.; Davis,J.C.; Averill,B.A.; Husle,C.L.; Stufkens,D.J.; Bolscher,B.G.J.M.; Wever,R. Biochem. Biophys. Acta 1985, 828, 58-66.

13. Andersson,L.A.; Loehr,T.M.; Lim,A.R.; Mauk,A.G. J. Biol. Chem. 1984, 259, 15340-15349.

14. Brittian,T.; Greenwood,C.; Barher,D. Biochim. Biophys. Acta 1982, 705, 26-32.

15. Chang,C.K.; Wu,W. J. Biol. Chem. 1986, 261, 8593-8596.

16. Chang,C.K.; Barkigia,K.M.; Hanson,L.K.; Fajer,J. J. Am. Chem. Soc. 1986, 108, 1352-1354.

17. Strauss,S.H.; Silver,M.E.; Long,K.M.; Thompson,R.G.; Hudgens,R.A.; Spartalian,K.; Ibers,J.A. J. Am. Chem. Soc. 1985, 107, 4207-4215.

18. Platt,J.R. in Radiation Biology; Hollaender,A. Ed.; Mcgraw-Hill, New York, Vol. III, pp

19. Longuet-Higgins,H.; Rector,C.W.; Platt,J.R. J. Chem. Phys. 1950, 18, 1174-1181.

20. Gouterman,M. J. Chem. Phys. 1959, 30, 1139-1161.

21. Gouterman,M. J. Mol. Spec. 1961, 6, 138-163.

22. a) Califano,M. Vibrational States; John Wiley & Sons, New York, 1-15. b) Centeno,J.A. Dissertation (1987), Michigan State Univ. East Lansing, MI, 48824

23. Heilter,W. in The Quantum Theory of Radiation, 3rd ed. Oxford University Press, New York, 1954.

24. Albrecht,A.C. J. Chem. Phys. 1960, 33, 156-169.

25. Clark,R.J.H.; Stewart,B. Struct. Bond. 1979, 36, 1-80.

26. Ozaki,Y.; Iriyama,K.; Ogoshi,H.; Ochiai,T.; Kitagawa,T. J. Phys. Chem. 1986, 90, 6105-6112.

27. Callahan,P.M.; Babcock,G.T. Biochemistry 1981, 20, 952-958.

28. Spiro,T.G.; Stong, J. D.; Stein, P. J. Am. Chem. Soc. 1979, 101, 2684-2655.

29. Choi, S.; Spiro, T. G.; Langry, K. C.; Smith, K. M.; Budd, D. L.; La Mar, G. N. J. Am. Chem. Soc. 1982, 104, 4345-4351.

30. Renner,M.W; Forman,A.; Wu.W.; Chang,C.K.; Fajer,J. J. Chem. Soc. 1989, 111, 8619-8621.

31. Whitlock, H. W. Jr.; Hanauer, R.; Oester, M. Y.; Bower, B. K. J. Am. Chem. Soc. 1969, 91, 7485-7489.

32. Perrin, D. D.; Armarego, W. L. F.; Perrin, D. R. In the purification of Laboratory Chemicals 2nd Ed. Pergamon Press; New York, 1980.

33. Aramendia,P.F.; Redmond,R.W.; Novell,S.; Schuster,W.; Braslavsky,S.E.; Schaffner,K.; Vogel,E. Photochem. Photobiol. 1986, 44, 555-559.

34. Levanon,H.; Toporowicz,M.; Ofir,H.; Fessenden,R.W.; Paritosh,K.D.; Vogel,E.; Kocher,M.; Parmod,K. J. Phys. Chem. 1988, 92, 2429-2433.

35. Redmond,R.W.; Valduga,G.; Novell,S.; Braslavsky,S.E.; Schaffner,K.; Vogel,E.; Pramond,K.; Kocher,M. J. Photochem. Photobiol. B 1989, 3, 193-207.

36. Boldt,N.J.; Donohoe,R.T.; Birge, R.R.; Bocian,D.F. J. Am. Chem. Soc. 1987, 109, 2284-2298.

37. Andersson, L.A.; Loehr,T.N.; Stershic,M.T.;Stolzenberg, A.M. Inorg. Chem. 1990, 29, 2278-2285.

38. Fonda,H.N.; Oertling,W.A.;Salehi,A.; Chang,C.K.; Babcock,G.T. J. Am. Chem. Soc. 1990, 112, 9497-9507.

39. Andersson,L.A.; Loehr,T.M. Cotton,T.M.; Simpson,D.J.; Smith,K.M. Biochim. Biophys. Acta. 1989, 974, 163-179.

40. Donohoe,R.J.; Frank,H.A.; Bocian,D.F.; Photochem. Photobiol. 1988, 48, 531-537.

41. Schick,A.G.; Bocian,D.F. Biophys. Biochem. Acta. 1987, 895, 127-154.

42. Woodruff,W.H.; Kossler,R.J.; Ferris,N.S.; Dallinger,R.F. Adv. Chem. Ser. 1982, 201, 625-659.

43. Kitagawa,T.; Ozaki,Y. Struct. Bonding 1987, 109, 71-114.

44. Shelnutt,J.A. J. Am. Chem. Soc. 1987, 109, 4169-4173.

45. Oertling,W.A.; Salehi,A.; Chung,Y.C.; Leroi,G.E.; Chang,C.K.; Babcock,G.T. J. Phys. Chem. 1987, 91, 5587-5898.

46. Salehi,A.; Oertling,W.A.; Fonda,H.N.; Chang,C.K.; Babcock,G.T. Photochem. Photobiol. 1988, 48, 525-530.

47. Donohoe,R.T.; Duchowski,J.K.; Bocian,D.F. J. AM. Chem. Soc. 1988, 110, 6119-6124.

48. Oertling,W.A.; Salehi,A.; Chang,C.K.; Babcock,G.T. J. Phys. Chem. 1989, 93, 1311-1319.

49. Czernuszewicz,R.S.; Macor,K.A.; Li,X.-Y.; Kincaid,J.K.; Spiro,T.G. J. AM. Chem. Soc. 1989, 111, 3860-3869.

50. Ksenofontova,N.M.; Maslov,V.G.; Sidorov,A.N.; Bobovich, Y.S. Opt. Spectrosc. 1976, 40, 452-465.

51. Teraoka,J.; Hashimoto,S.; Sugimoto,H.; KitagaWa,T. J. Am. Chem. Soc. 1987, 109, 180-184.

52. Donohoe,R.T.; Atamian,M.; Bocian,D.F. J. Am. Chem. Soc. 1987, 109, 5593-5599.

53. Spiro,T.G. in Iron Porphyrins; Lever,A.B.P., Gray,H.B., Eds.; Addison-Wesley, Reading,MA, 1983; Part2, 89-159.

54. Lutz,M.; Robert,B. in Biological Applications of Raman Spectrocsopy; Spiro,T.G. Ed.; John Wiley & Sons, New York, 1988, 347-411.

55. Callahan,P.M.; Cotton,T.M. J. Am. Chem. Soc. 1987, 109, 7001-7007.

56 Schiemke,A.K.; Eirich,L.D.; Loehr,T.M. Biochim. Biophys. Acta. 1983, 748, 143-150.

57. Schiemke,A.K.; Scott,R.A.; Shelnutt,J.A. J. Am. Chem. Soc. 1988, 110, 1645-1646.

58. Mayer,E.; Gardiner,D.J.; Hester,R.E. Mol. Phys. 1973, 26, 783-787.

59. Salama,S.; Spiro,T.G. J. Raman Spectrosc. 1977, 6, 57-60.

60. Abe,M.; Kitagawa,T.; Kyogoku,Y. J. Chem. Phys. 1978, 69, 4526-4534.

61. Gladkov,L.L.; Solovyov,K.N. Spectrochim, Acta 1986, 42A, 1-10.

62. Li,X.-Y.; Czernuszewicz,R.S.; Kincaid,J.A.; Stein,P.; Spiro,T.G. J. Phys. Chem. 1990, 94, 47-61.

63. Atamian,M.; Donohoe,R.J.; Lindsey,J.R.; Bocian,D.F. J. Phys. Chem. 1989, 93, 2236-2243.

64. Li,X.-Y.; Czernuszewicz,R.S.; Kincaid,J.A.; Su,O.Y.; Spiro,T.G. J. Phys. Chem. 1990, 94, 31-47.

65. Simpson,W.T. J. Chem. Phys. 1949, 17, 1218-1221.

66. Platt,J.R. J. Chem. Phys. 1950, 18, 1168-1173.

67. Pariser,R.; Parr,R.G. J. Chem. Phys. 1953, 21, 767-776.

68. Moffitt,W. J. Chem. Phys. 1954, 22, 1820-1829.

69. Shelnutt,J.A. J. Phys. Chem. 1984, 88, 4988-4992.

70. Shelnutt,J.A.; Prtiz,V. J. Phys. Chem. 1985, 89, 4733-4739.

71. Obtained from the correlation tables in: Wilson,E.B.; Decius,J.C.; Cross, P.C. In Molecular Vibrational: The Theory of Infrared and Raman Vibrational Spectra; Dover Publications, 1955; Appendix X. Note that the $C_{2''}$ axes of MOEP are retained in MPPC.

72. The effects of ring bromination and metal substitution on the individual MO energies will be more readily understood when calculations yielding orbital coefficients become available.

73. Bernstein,H.T. Phil. Trans. R. Soc. London A 1979, 293, 287-302.

74. Spiro,T.G.; Strekas,T.C. Proc. Natl. Acad. Sci. U.S.A. 1972, 69, 2622-2626.

75. Shelnutt,J.A.; O'Shea,D.C.; Yu,N.-T.; Cheung,L.D.; Felton,R.H. J. Chem. Phys. 1976, 64, 1156-1165.

76. Shelnutt,J.A.; Cheung,L.D.; Chang,R.C.C.; Yu,N.-T.; Felton,R.H. J. Chem. Phys. 1977, 66, 3387-3398.

77. Nishimura,Y.; Hirakawa,A.Y.; Tsuboi,M.J. Mol. spectrosc. 1977, 68, 335-358.

78. Shelnutt,J.A. J. Chem. Phys. 1981, 74, 6644-6657.

79. Spaulding,L.D.; Chang,C.C.; Yu,N.-T.; Felton,R.H. J. Am. Chem. Soc. 1975, 97, 2517-2525.

80. Huong,P.V.; Pommier,J.-C.C.R. Acad. Sci. Ser. C 1977, 285, 519-522.

81. Parthasarathi,N.; Masen,C.; Yamaguchi,S.; Spiro,T.G. J. Am. Chem. Soc. 1987, 109, 3865-3871.

82. Cullen,D.L.; Meyer,E.F. J. Am. Chem. Soc. 1974, 96, 2095-2102.

83. a) Timkovich,R.; Tulinsky,A. J. Am. Chem. Soc. 1969, 91, 4430-4432. b) Silvers,S.; Tulinsky,A. J. Am. Chem. Soc. 1990, 112, 1634-1635.

84. Scheidt,W.R.; Lee,Y.T. Struct. Bonding 1987, 64, 1-70. and references therein.

85. Smith,D.W.; Williams,R.T.P. Struct. Bonding 1969, 7, 1-45.

86. Adar,F. in The Porphyrins; Dolphin,D., Ed.; Academic: New York, 1979; Vol.III, 167-209.

87. Neya,S.; Chang,C.K.; Vogel,E. manuscript in preparation.

88. Kitagawa,T.; Abe,M.; Kyogoku,Y.; Ogoshi,H.; Sugimoto,H.; Yoshida,Z. Chem. Phys. Lett. 1977, 48, 55-58.

89. Svec,W.A. In The Porphyrins; Dolphin, D., Ed.; Academic Press: New York, 1978; Vol. 5, 341-349

90. Eglington,D.G.; Barber,D.; Thomson,A.J.; Greenwood,C.; Segel,A.W. Biochim. Biophys. Acta 1982, 703, 187-195.

91. Okamura,M.Y.; Feher,G.; Nelson,N. In Photosynthesis; Godvindjee, Ed.; Academic Press, 1982; Vol. I, 195-272.

92. Siegel,J.M.; Rueger,D.C.; Barber,M.J.; Krueger,R.J; Orme-Johnson,N.R.; Orme-Johnson,W.H.J. Biol. Chem. 1982, 257, 6343-6350.

93. Ellefson,W,L.; Whitman,W.B.; Wolfe,R.S. Proc. Natl. Sci. USA 1982, 79, 3707-3710.

94. Sibbet,S.S.; Hurst,J.K. Biochemistry 1984, 23, 3007-3013.

95. Bondoc, L. L.; Chau, M. H.; Price, M. A.; Timkovich, R. Biochemistry 1986, 25, 8458-8466.

96. Chatfield,M.J.; La Mar,G N.; Lecomte,J.T.J.; Balch, A.L.; Smith,K.M.; Langry,K.C. J. Am. Chem. Soc. 1986, 108, 7108-7110.

97. Mcree,D.E.; Richardson,D.C.; Richardson,J.S.; Siegel,L.M. J. Biol. Chem. 1986, 261, 10277-10281.

98. Andersson,L.A.; Sotiriou,C.; Chang,C.K.; Loher,T.M. J. Am. Chem. Soc. 1987, 109, 258-264.

99. Schick,G.A.; Bocian,D.F. Biochim. Biophys. Acta 1987, 895, 127-154.

100. Ozaki,Y.; Kitagawa,T.; Ogoshi,H. Inorg. Chem. 1979, 18, 1772-1776.

101. Ozaki,Y.; Iriyama,K.; Ogoshi,H.; Ochiai,T.; Kitagawa,T. J. phys. Chem. 1986, 90, 6113-6118.

102. Fujiwara,M.; Tasumi,M. J. Phys. Chem. 1986, 90, 250-255.

103. Fujiwara,M.; Tasumi,M. J. Phys. Chem. 1986, 90, 5646- 5650.

104. Andersson,L.A.; Loehr,T.M.; Chang,C.K.; Mauk, A.G. J. Am. Chem. Soc. 1985, 107, 182-191.

105. Andersson,L.A.; Loehr,T.M.; Sotiriou,C.; Wu,W.; Chang,C.K. J. Am. Chem. Soc. 1986, 108, 2908-2916.

106. Boldt,N.J.; Bocian,D.F. J. Phys. Chem. 1988, 92, 581-586.

107. Ogoshi,H.; Watanabe.E.; Yoshida,Z.; Kincaid,J.; Nakamoto,K. Inorg. Chem. 1975, 14, 1344-1350.

108. Donohoe,R.J.; Atamian,M.; Bocian,D.F. J. Phys. Chem. 1989, 93, 2244-2252.

109. Prendergast,K.; Spiro,T.G. J. Phys. Chem. 1991, 95, 1555-1563.

110. Lutz,M. In Advances in Infrared and Raman Spectroscopy; Clark,R.J.H.; Hester,R.E., Eds.; Wiley: New York, 1984; Vol. 11, 211-300.

111. Cotton,T.M.; Van Duyne,R.P. J. Am. Chem. Soc. 1987, 1981, 103, 6020-6026.

112. Callahan,P.M.; Cotton,T.M. J. Am. Chem. Soc. 1987, 109, 7001-7007.

113. Cotton,T.M.; Timkovich,R.; Cork,M.S. FEBS. Lett. 1981, 133, 39-44.

114. Ching,Y.; Ondrias,M.R.; Rousseau,D.L.; Muhoberac, B.B.; Wharton,D.C. FEBS. Lett. 1982, 138, 239-244.

115. Andersson, L.A.; Loehr,T.M.; Weishih,W.; Chang,C.K; Timkovich,R. FEBS. Lett. 1990, 267, 285-288.

116. Andersson,L.A.; Loehr,T.M.; Thompson,R.G.; Strauss,S.H. Inorg. Chem. 1990, 29, 2142-2147.

117. Ondrias,M.R.; Carson,S.D.; Hirasawa,M.; Knaff,D.B. Biochim. Biophys. Acta 1985, 830, 159-163.

118. Han,S.; Madden,J.F.; Thompson,R.G.; Strauss,S.H.; Siegel,L.M.; Spiro,T.G. Biochemistry 1989, 28, 5461-5470.

119. Melamed,D.; Sullivan,E.P.; Prendergast,K.; Strauss, S.H.; Spiro,T G. Inorg. Chem. 1991, 30, 1308-1319.

120. Lai,K.K.; Yue,K.T. J. Raman Spectrosc. 1990, 21, 21-26.

121. Lai,K.K.; Moura,I.; Liu,M.Y.; Legall,J.; Yue,K.Y. Biochim. Biophys. Acta 1991, 1060, 25-27.

122. Procyk,A.D.; Bocian,D.F. J. Am. Chem. Soc. 1991, 113, 3765-3773.

123. Gladkov,L.L.; Starukhin,A.S.; Shulga,A.M. Spectrochim. Acta 1987, 43A, 1125-1134.

124. Wilson,E.B.; Desius,J.C.; Cross,P.C. In Molecular Vibrations, McGraw-Hill, New York, 1955.

125. Mclntoch,D.F.; Michaelian,K.M. Can. J. Spectrosc. 1979, 24, 1-10. and references therein.

126. Morino,Y.; Kuchitsu,K. J. Chem. Phys. 1952, 20, 1809-1810.

127. Strauss,S.H.; Silver,M.E.; Long,K.M.; Thompson, R.G.; Hudgens,R.A.; Spartalian,K.; Ibers,J.A. J. Am. Chem. Soc. 1985, 107, 4207-4215.

128. Schachtschneider,J.H. Vibrational Analysis of Polyatomic Molecules; Shell Development Co.; Emeryville, Ca, 1962; Vol. I-III.

129. Li,X.-Y.; Czernuszewicz,R.S.; Kincaid,J.R.; Stein,P; Spiro,T.G. J. Phys. Chem. 1990, 94, 47-61.

130. Spaulding,L.D.; Andrews,L.C.; Williams,G.J.D. J. Am. Chem. Soc. 1977, 99, 6918-6923.

131. Gallucci,J.C.; Swepston,P.N.; Ibers,J.A. Acta Crystallogr. Sect. B: Struct. Crystallogr. Chem. 1982, 38B, 2134-2139.

132. Because of its longer singlet lifetime and higher fluoresence yield, it was impossible to record visible excitation raman spectra for ZnOEC and its selectively deuterated compounds.

132. Moustakali,I.; Tulinsky,A. J. Am. Chem. Soc. 1973, 95, 6811-6815.

133. Collins,D.M.; Hoard,J.L. J. Am. Chem. Soc. 1970, 92, 3761-3771.

134. Li,X.-Y.; Zgierski,M.Z. J. Phys. Chem. 1991, 95, 4268-4287.

135. Scheidt,W.R. In the Porphyrins; Dorphin, D. Ed.; Academic Press; New York, 1978; Vol III. 463-512.